AN ABSTRACT OF THE THESIS OF

T Bruce Appelgate Jr for the degree of Master of Science in
Oceanography presented on October 19, 1988.

Title: Tectonic and Volcanic Structures of the Southern Flank of Axial Volcano, Juan de Fuca Ridge: Results From a SeaMARC I Sidescan Sonar Survey

Redacted for Privacy

Abstract Approved: _____
Stephen R. Hammond

A 5km swath-width SeaMARC I sidescan sonar survey, conducted over the zone of overlap between the southern rift zone of Axial Volcano and the northern tip of the Vance spreading segment on the Juan de Fuca Ridge (between 45°24'N and 45°50'N latitude), was analyzed to locate the present position of the Juan de Fuca spreading axis, and to determine the tectonic and volcanic structure of the seafloor. Sidescan data were processed in concert with the ship's Loran-C navigation to construct navigated, orthorectified mosaics of the sidescan imagery. In order to navigate the sidescan swaths, a simple numerical model was developed to describe the tracking behavior of the towed sidescan vehicle. Successive positions and orientations of the sidescan towfish were estimated, and were used to assign latitude/longitude values to individual sidescan pixels. Navigated sidescan pixels were mapped by computer onto an absolute (latitude/longitude) reference grid, and the resulting sidescan mosaic was compared directly to existing high-resolution SeaBeam bathymetry in order to discriminate the effects of large- and small-scale roughness on the observed backscatter distribution. The Juan de Fuca spreading axis between 45°25'N and 45°39'N is located within the axial valley of the Vance segment. Relative age relationships, based on crosscutting and superposition principles, indicate that the most recent volcanism within the axial valley has occurred along the valley's central ridge, and that the most recent resolvable extension within the axial valley has been concentrated between the central ridge and west valley wall. The Vance segment terminates at 45°39'N, and is not associated with a transform fault. The south rift zone of Axial volcano is a constructional volcanic feature that is not faulted, and a discrete axis of spreading over the south flank of Axial volcano is not resolvable in the sidescan imagery; however, the spreading locus north of 45°39'N is constrained to a zone between 130°06'W and

129°54'W. The lack of a well-defined spreading axis north of 45°39'N indicates that the physical manifestation of the divergent plate boundary has been modified or masked by hotspot volcanic processes associated with Axial volcano such that a definitive locus of spreading is not expressed in the surface morphology.

Tectonic and Volcanic Structures of the Southern Flank of Axial Volcano, Juan de Fuca Ridge: Results From a SeaMARC I Sidescan Sonar Survey

by

T. Bruce Appelgate, Jr.

A THESIS
submitted to
Oregon State University

in partial fulfillment of
the requirements for the
degree of

Master of Science

Completed October 19, 1988
Commencement June 1989

APPROVED:

Redacted for Privacy

Professor of Oceanography in charge of major

Redacted for Privacy

Dean of College of Oceanography

Redacted for Privacy

Dean of Graduate School

Date thesis is presented October 19, 1988

Typed for researcher by Bruce Appelgate

ACKNOWLEDGEMENTS

This gargantuan project could have never been pulled off without the patience, expertise, and graciousness of several industrious people with whom I've worked closely during my tenure as a graduate student. First and foremost, I thank my major professor, Dr. Steve Hammond, for providing me with the opportunity to pursue this degree at Oregon State University, and for making available the results of the 1986 SeaMARC I sidescan survey that constitute the bulk of the data in this thesis. Dr. Hammond sacrificed much of his own time, and took time out from his very hectic schedule, to guide me along the path of academic enlightenment. Thanks, boss. I am also indebted to Dr. Chris Fox for his indispensible assistance with the data reduction and image processing phases of this project, as well as his timely and to-the-point reviews of several iterations of this manuscript. And I'm proud to say that there's a white sandy tropical beach (a Fox original) hanging on the wall in my living room -- I've been there, dude. Dr. Bob Embley helped me with the finer points of interpreting geological structures from sidescan records, helpfully reviewed this thesis, and taught me the basics of going baseline and the give-and-go. Dr. Bob Duncan served on my committee on very short notice, and provided helpful comments on this thesis. I thank Drs. John Delaney, Paul Johnson, Robin Holcomb and Ellen Kapel for fruitful discussions during the early stages of this project.

I am very grateful to T-K Andy Lau for the time and energy he devoted to helping me with computer programming, and I stand in awe of his industrious nature. Maria Restrepo patiently and completely answered all my questions regarding SeaBeam processing (no matter how busy she was), and I thank her for providing a last-minute plot of the Cobb Offset for my discipline exam. My hat is off to Sue Hanneman for keeping things around MRRD on an even keel with her charming, subtle wit and remarkable work ethic -- I wish her lots of blue skies and big winds. I thank Jessica Waddell for efficiently cutting a swath through loads of paperwork and effectively keeping me out of hock. I also wish to express my gratitude to the Stationary Club for accepting me as non-dues-paying member. Really, guys, payday's just around the corner. Many people have made my stay at OSU memorable, including Tom Lippmann, Annette deCharon, Colin Roesler, Russ VanDissen, Dana Desonie, Gary and Cathy Davis, Mike Parker, Cindy Bowline, and Yip Chun. Finally, I thank my mom and dad for their unflagging encouragement, love and support over the past 25 years, and Brian, Brad and Dianna for just being there. Most of all, thank you Lisa for putting up with me through all of this.

This work was supported by the NOAA VENTS program through the OSU Cooperative Institute for Marine Resource Studies.

TABLE OF CONTENTS

INTRODUCTION 1

TECTONIC EVOLUTION OF THE JUAN DE FUCA SPREADING SYSTEM AND GEOLOGIC SETTING OF AXIAL VOLCANO 5
- Tectonic Evolution of the Juan de Fuca Ridge System 5
- Tectonic Setting of the Northern Vance Segment and Axial Volcano 8

THE SEAMARC I SWATH MAPPING SYSTEM 14
- The Subsea System 14
- The Topside System 17
- Image Resolution 18

DATA PROCESSING 21
- Navigating the Path of the Sidescan Vehicle 22
- Gridding and Plotting Navigated Sidescan Imagery 33

INTERPRETING SIDESCAN IMAGES 42
- Fundamental Concepts for Interpreting Backscatter Patterns 43
- Interpreting Geological Structures From Backscatter Patterns 48

RESULTS 60
- The Vance Segment 60
  - The Vance Segment From 45°26'N to 45°32'N 61
  - The Vance Segment From 45°32'N to 45°40'N 89
- The South Rift Zone of Axial Volcano 96
- South Helium Basin 122

DISCUSSION 133
- Timing of Events and Implications for the Tectonic Evolution of the Northern Vance Spreading Segment 133
- Timing of Events on the Southern Flank of Axial Volcano 137
- Constraints on the Timing of Events Based on Bathymetric Data 141
- Discrimination of the Locus of Spreading Between 45°24'N and 45°47'N 145

AREAS OF FUTURE STUDY 150

SUMMARY 152

BIBLIOGRAPHY 155

LIST OF FIGURES

Figure		Page
1.	Location map of Axial Volcano relative to the spreading ridges and crustal plates of the northeast Pacific	2
2.	Regional SeaBeam bathymetry of Axial volcano and the northern Vance spreading segment	11
3.	Physical configuration of the SeaMARC I sidescan sonar system	15
4.	Schematic diagram of the method used to determine the horizontal distance of the towfish from the ship	24
5.	Stepwise, rigid-wire model for estimating towfish positions behind the ship	26
6.	Rigid-wire model of the towfish behavior during a turn	29
7.	Stepwise model for estimating towfish positions behind the ship, accounting for flexure of the towcable	31
8.	Flexing-wire model of the towfish behavior during a turn	34
9.	Sidescan pixel gridding process	36
10.	Backscatter characteristics of mosaicked sidescan swaths	39
11.	Sidescan images of positive-relief structures	44
12.	Sidescan images of negative-relief structures	46
13.	Sidescan image of a fault scarp facing nadir	49
14.	Sidescan image of a fault scarp facing away from nadir	51
15.	Sidescan image of lavas overlying a fault scarp	54
16.	Sidescan image showing effects of micromorphology and/or acoustic impedance constrast on backscatter patterns	56
17.	Location map for detailed sidescan images shown in Figures 18 through 29	62
18.	The Vance segment between 45°26'N and 45°29'N latitude	
	A. Sidescan mosaic	65
	B. Geological interpretation	66
	C. Bathymetry	67
19.	The Vance segment between 45°29'N and 45°32'N latitude	
	A. Sidescan mosaic	69
	B. Geological interpretation	70
	C. Bathymetry	71
20.	The Vance segment between 45°32'N and 45°35'N latitude:	

A. Sidescan mosaic 73
B. Geological interpretation 74
C. Bathymetry 75
21. The Vance segment between 45°35'N and 45°38'N latitude:
A. Sidescan mosaic 77
B. Geological interpretation 78
C. Bathymetry 79
22. The Vance segment between 45°38'N and 45°41'N latitude:
A. Sidescan mosaic 81
B. Geological interpretation 82
C. Bathymetry 83
23. Axial volcano's south rift zone between 45°44'N and 45°47'N latitude:
A. Sidescan mosaic 99
B. Geological interpretation 100
C. Bathymetry 101
24. Axial volcano's south rift zone between 45°41'N and 45°44'N latitude:
A. Sidescan mosaic 103
B. Geological interpretation 104
C. Bathymetry 105
25. Axial volcano's south rift zone between 45°38'N and 45°41'N latitude:
A. Sidescan mosaic 107
B. Geological interpretation 108
C. Bathymetry 109
26. Axial volcano's south rift zone between 45°35'N and 45°38'N latitude:
A. Sidescan mosaic 111
B. Geological interpretation 112
C. Bathymetry 113
27. Axial volcano's south rift zone between 45°32'N and 45°35'N latitude:
A. Sidescan mosaic 115
B. Geological interpretation 116
C. Bathymetry 117
28. South Helium Basin between 45°41'N and 45°44'N latitude:
A. Sidescan mosaic 125
B. Geological interpretation 126
C. Bathymetry 127
29. South Helium Basin between 45°44'N and 45°47'N latitude:

A. Sidescan mosaic 129
B. Geological interpretation 130
C. Bathymetry 131
30. Line drawing showing relative ages of structures within the Vance Segment's axial valley 138
31. Line drawing showing relative ages of structures within South Helium Basin 142

LIST OF PLATE

Plate		Page
1.	1:100,000 sidescan mosaic of the southern flank of Axial volcano, the northern tip of the Vance spreading segment, and surrounding areas	map pocket

TECTONIC AND VOLCANIC STRUCTURES OF THE SOUTHERN FLANK OF AXIAL VOLCANO, JUAN DE FUCA RIDGE: RESULTS FROM A SEAMARC I SIDESCAN SONAR SURVEY

INTRODUCTION

Axial volcano, located near 45°00'N/130°00'W (Figure 1), is the most recent product of the Cobb-Eickelberg hotspot (Delaney et al., 1981; Hammond and Delaney, 1985), and is being constructed on or near the Juan de Fuca spreading axis (Davis and Karsten, 1986; Hammond et al., 1987). The morphology of the volcano is complex: major rift zones extend 50 km north and south of the main volcanic edifice, and large embayments penetrate the volcano's northern and southern flanks. The complicated structure of Axial volcano has been attributed to complex tectonic and volcanic processes that result from the proximity of the hotspot to the Juan de Fuca spreading center (Karsten and Delaney, 1986; Hammond et al., 1987). Previous studies (e.g., Delaney et al., 1981; Hammond and Delaney, 1985) have concluded that the Juan de Fuca spreading axis in the vicinity of Axial volcano is offset to the west of the spreading segments to the north (the Northern Symmetrical Segment) and south (the Vance segment). Based on an analysis of high-resolution SeaBeam bathymetry, Hammond and Delaney (1985) proposed that the axis of Juan de Fuca spreading is (or recently was) located along the rift zones of the volcano. However, bathymetric data alone cannot unequivocally constrain the position of the spreading axis near Axial volcano, and higher resolution imaging techniques are required to more completely understand the structural complexity of this region.

In order to more accurately define the position of the divergent plate boundary near Axial Volcano, a SeaMARC I sidescan sonar survey was conducted over the zone of overlap between Axial volcano's southern rift zone and the northern tip of the Vance spreading segment. The survey was performed in July, 1986 aboard the National Oceanic and Atmospheric Administration (NOAA) ship *Discoverer* as part of an ongoing study by the NOAA VENTS program that is investigating the volcanic, tectonic, and hydrothermal processes associated with the Juan de Fuca spreading center system. A 1500 km^2 area was insonified with 100% coverage using adjacent 5 km wide sonar swaths, and over 300 megabytes of digital sidescan data were acquired. The survey was designed to investigate the geological structure and constitution of Axial volcano's south rift zone and the Juan de Fuca spreading axis between 45°25'N and 45°50'N, utilizing the capability of SeaMARC I

Figure 1. Diagram showing the location of Axial Volcano relative to the spreading ridges and crustal plates of the northeast Pacific. Explanation of symbols: ER, Explorer Ridge; STFZ, Sovanco Transform Fault Zone; WV, West Valley; EO, Endeavour Offset; ES, Endeavour Segment; CO, Cobb Offset; NSS, Northern Symmetrical Segment; VS, Vance Segment; CS, Cleft Segment; BTFZ, Blanco Transform Fault Zone; GR, Gorda Ridge; GDZ, Gorda Deformation Zone; MFZ, Mendocino Fracture Zone. Stippled bold line between the Vance and Northern Symmetrical Segments indicates the location of the divergent plate boundary zone near Axial Volcano inferred from the results of this survey [modified from Riddihough, 1984].

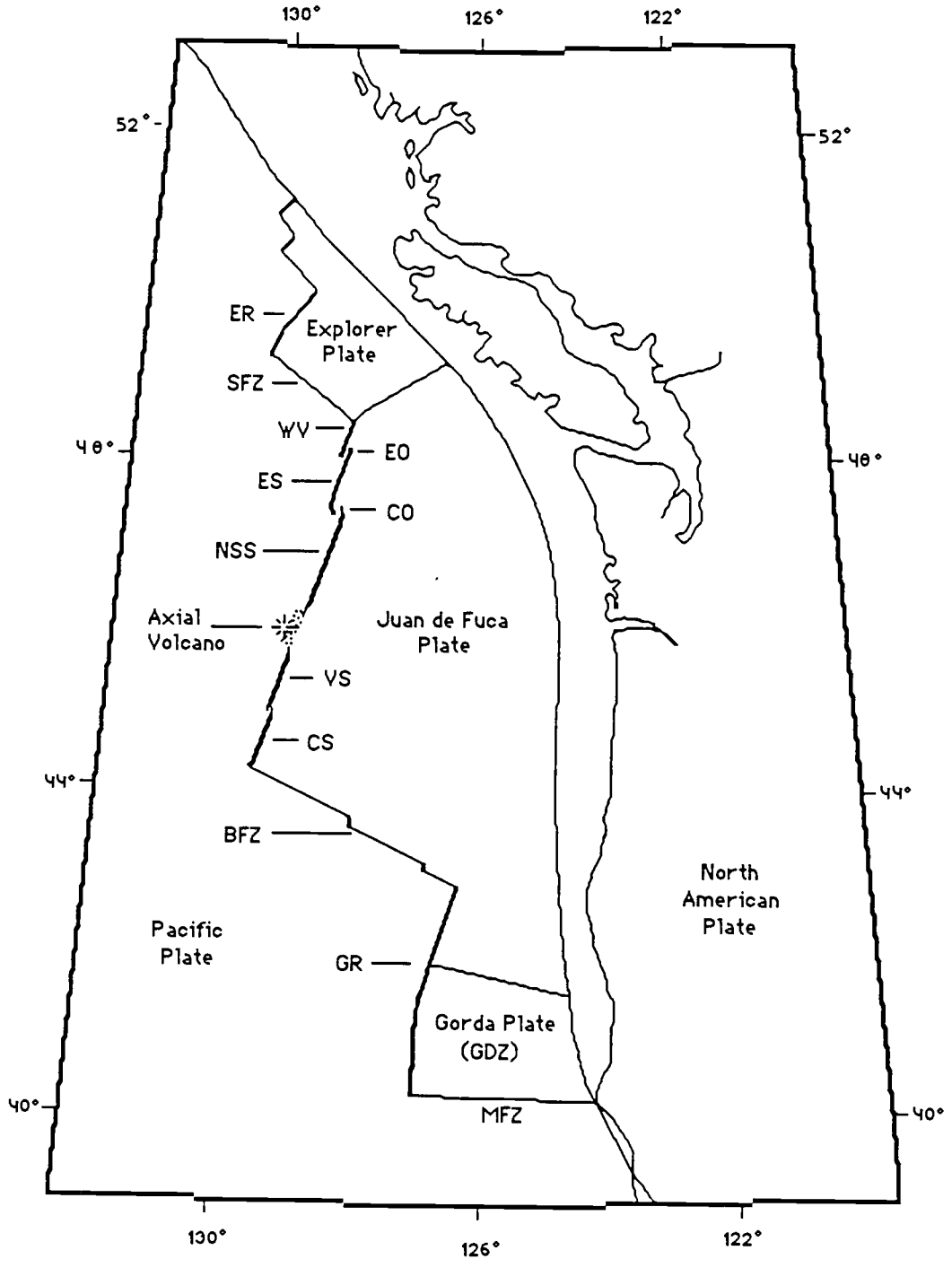
130°
126°
122°
52°
52°
ER
Explorer
Plate
SFZ
WV
EO
40°
40°
ES
CO
NSS
Axial
Volcano
Juan de Fuca
Plate
VS
CS
44°
44°
BFZ
North
American
Plate
Pacific
Plate
GR
Gorda Plate
(GDZ)
40°
40°
MFZ
130°
126°
122°

Figure 1.

to discriminate topographic structures that are not resolvable in the SeaBeam bathymetry, and its ability to discern differences in the composition of the seafloor. Specifically, the primary objectives of this sidescan survey are to establish 1) the precise location of the divergent plate boundary between 45°25'N and 45°50'N, where it is resolvable, 2) the presence or absence of a transform fault linking the offset spreading centers, and 3) the tectonic and/or volcanic processes that have contributed to construct the axial valley of the Vance spreading segment, and Axial volcano's southeast flank and southern rift zone. This paper discusses the processing and analytical techniques that were applied to these data, and presents a detailed discussion of the volcanic and tectonic features which were resolved within this survey area.

TECTONIC EVOLUTION OF THE JUAN DE FUCA SPREADING SYSTEM AND GEOLOGIC SETTING OF AXIAL VOLCANO

The Juan de Fuca (JDF) ridge system is an intermediate-rate divergent plate boundary (≈ 6 cm/year full spreading rate) that separates the Pacific plate from the JDF plate in the northeast Pacific Ocean (Figure 1). The ridge system is bounded to the north and south by the Sovanco and Blanco Fracture Zones, respectively, and is composed of six distinct spreading segments. Geometric reconstructions of the magnetic anomaly patterns in the northeast Pacific Ocean indicate that the JDF spreading system has experienced a complex tectonic evolution that has involved the separation and progressive isolation of the ridge system from the East Pacific Rise (EPR), a 20° reorientation in azimuth over a period of 10 Ma, and several episodes rift propagation. Recently, the central segment of the JDF ridge has jumped westward towards the Cobb-Eickelberg hotspot. The history of the JDF plate has been as complex as that of the ridge system, and included several changes in the relative pole of rotation between the JDF and Pacific plates, and the fragmentation of the initial JDF plate into two (or possibly three) smaller plates. These processes are discussed in detail within the following section.

Tectonic Evolution of the Juan de Fuca Ridge System

The spreading history of the JDF ridge system is recorded in the magnetic anomaly patterns in the seafloor of the northeast Pacific Ocean, which were initially mapped in detail by Raff and Mason (1961). Seafloor magnetic anomalies are the consequence of seafloor spreading and geomagnetic field reversals: as new oceanic crust is formed, it is magnetized in the ambient direction of the Earth's magnetic field. As seafloor spreading progresses, reversals in the polarity of the Earth's magnetic field are recorded as strips of crust parallel to the ridge crest that are either normally or reversely magnetized (Vine and Mathews, 1963; Vine and Wilson, 1965; Vine, 1966). Atwater (1970) applied the geomagnetic time scale of Heirtzler et al. (1968) to marine magnetic anomaly patterns to reconstruct the tectonic evolution of the plate boundaries in the northeast Pacific. Prior to 30 Ma ago, the Juan de Fuca ridge system and East Pacific Rise were part of a continuous seafloor spreading system that separated the Pacific plate from the now-extinct Farallon plate. The Farallon plate spread eastward from the ridge system and was consumed along the convergent margin at the western edge of the North American plate. The North

American plate was moving westward (in the absolute, hotspot frame of reference) and progressively encroached upon the Pacific/Farallon plate boundary until, between 27-25 Ma ago (Engebretson et al., 1985), the North American plate collided with and overrode the offshore ridge system along the southern California margin (Atwater, 1970). At this point, the Farallon plate was divided into two smaller plates, the Juan de Fuca in the north and the Cocos in the south. The original ridge system was cleaved into two subsystems, the JDF and the EPR, separated by the San Andreas transform fault. Continued westward movement of the North American plate has caused the two ridge systems to become progressively isolated from one another.

The magnetic anomaly pattern around the JDF ridge system is complex, and is not consistent with a simple model of uniform, bilaterally symmetric spreading about the ridge axis. The most recent magnetic reversal boundary, between the Bruhnes normal and Matuyama reversed epochs, is oriented 20° oblique (in a clockwise sense) to anomalies 10 Ma old; Carlson (1981) attributed this obliquity to a 20° clockwise rotation of the JDF ridge system, accommodated by asymmetric spreading, that resulted from a change in the direction of seafloor spreading. Several offsets in the magnetic anomaly pattern are evident on the JDF and Pacific plates that are oblique to both the trend of the ridge axis and of the nearby transform faults; these offsets have been interpreted as strike-slip faults that resulted from either non-rigid plate behavior (Vine, 1966: Elvers et al., 1973) or from the presence of several micro-plates attached to the JDF ridge (Silver, 1971; Riddihough et al., 1983). However, an elegant solution that reconciles virtually all of the observed complexities of the magnetic anomaly pattern about the JDF system, without resorting to non-rigid plate behavior, involves rift propagation.

The propagating rift hypothesis (Hey, 1977) describes the along-axis migration of an offset in a spreading center, involving the longitudinal growth of one segment (the *propagating rift*) at the expense of the other segment (the *doomed rift*). For each increment of length gained by the propagating rift, an equal increment is lost by the doomed rift; thus the propagating rift advances while the doomed rift retreats. Rift propagation is concomitant with active spreading on both ridges, and new crust generated by the propagating rift assumes a characteristic wedge shape that points in the direction of propagation. The angle at the vertex of the wedge reflects the ratio between the propagation rate and spreading rate (Hey et al., 1986). Since the propagating rift is offset from the doomed rift, the propagator continually penetrates into older crust. The boundaries of the wedge-shaped section of crust

constitute discontinuities in crustal age, and therefore mark the location of discontinuities in the magnetic anomaly stripes. These boundaries were termed 'pseudofaults' by Hey (1977) because the propagating rift model does not require strike-slip motion to account for the offset magnetic anomalies on either side of the boundaries. As a consequence of rift propagation, lithosphere from one plate is transferred to the other as the propagator 'unzips' the older crust it abuts. Forward models of the tectonic evolution of the JDF ridge system, involving seven discrete propagators, have yielded results that closely approximate the observed magnetic anomaly patterns (Hey and Wilson, 1982; Wilson et al., 1984).

The propagating rift model can also account for the 20° clockwise reorientation of the JDF ridge system over the past 10 Ma. Propagating rifts are generally observed to be oriented slightly oblique to their conjugate doomed rifts, such that the width of the offset between them progressively increases with increasing propagation (Hey et al., 1980). Wilson et al. (1984) proposed rift propagation to be a mechanism for ridge reorientation. Analyses of the magnetic anomaly patterns surrounding the JDF ridge system indicate a gradual drift in the pole of rotation of the JDF plate relative to the Pacific plate (Riddihough, 1984; Nishimura et al., 1984; Wilson et al., 1984). Wilson et al. (1984) recognized two major shifts in the location of the relative motion pole, one at 8.5 Ma and another at 5.0 Ma. The most recent shift, which indicates a 10° clockwise shift in the direction of spreading, precipitated a change in the azimuth of active propagating rifts such that the ridges behind the propagator tips formed at an orientation more orthogonal to the new direction of plate spreading than the doomed ridges (Wilson et al., 1984). The ridge system was thus reoriented along a N20°E trend from its previous N10°E trend. This major shift was presumed to be due to a readjustment of stresses within the JDF plate caused by the separation of the Explorer plate from the larger JDF plate around 5.0 Ma (Wilson et al., 1984). Similarly, the pole shift at 8.5 Ma corresponds to a 10° shift in the Pacific/JDF spreading direction, which instigated an episode of ridge reorientation (from N00°E to N10°E) accommodated by rift propagation (Wilson et al., 1984). The cause of this shift is not well understood (Riddihough's (1984) analysis does not resolve this shift), although Wilson et al. (1984) attributed it to the formation of an independent Gorda plate at about 8.5 Ma.

The plate motions of the JDF system are thought to be influenced by some form of resistance to subduction at the convergent margin (Riddihough, 1984). Menard (1978) proposed that the young crust entering a convergent margin near ridge-trench intersections (such as the triple junction at the northern end of the JDF

plate system) acts as an impediment to subduction, while older crust farther away from the ridge-trench junction subducts more readily. As a result, the subducting plate pivots about a point near the ridge-trench intersection, and the relative motion between the two converging plates increases away from the pivot point. Plate motions of the JDF system determined by Riddihough (1984) are compatible with this concept of pivoting subduction: prior to 4 Ma, the JDF plate was intact, and moved most slowly at its northern end where the youngest crust was entering the Cascadia subduction zone. The presumed resistance to subduction of the young, buoyant crust exceeded the strength of the plate such that the Explorer plate separated from the JDF plate along the Nootka fault 4 Ma (Riddihough, 1984), leading to a reorganization of the stresses within the JDF plate (Wilson et al., 1984; Riddihough, 1984). From this time on, the two plates behaved independently. After 4 Ma, the youngest JDF crust entering the subduction zone was located farther south, near Cape Blanco, and by 2.5 Ma the location of the slowest-moving part of the JDF plate had shifted to the southeast.

Two models have been proposed for the tectonic setting of the southernmost part of the Juan de Fuca plate system. Riddihough (1984) reconstructed the magnetic anomalies over the southern JDF plate according to the tenets of rigid-plate tectonics, and concluded that the Gorda plate broke free from the southern JDF plate around 3 Ma , and constituted an independent, rigid plate from that time on. Wilson (1986) modelled the southern Gorda region as a diffuse zone of distributed deformation within the JDF crust north of the Mendocino transform, and does not recognize it as an independent, rigid plate.

Although there are inconsistencies in the timing of events for the evolution of the JDF system in the models of Riddihough (1984), Wilson et al. (1984), and Wilson (1986), they all generally conclude that stresses within the JDF plate system are at least in part controlled by complex interactions between the Juan de Fuca and North American plates at the convergent margin. The fragmentation of the JDF plate evidently led to a reorganization of the stresses that drive plate motion, and, according to Wilson et al. (1984), the changes in the direction of plate motion precipitated episodes of ridge reorientation via rift propagation.

Tectonic Setting of the Northern Vance Segment and Axial Volcano

The Vance segment is the second discrete spreading segment of the Juan de Fuca ridge north of the Blanco Fracture Zone (Figure 1). This segment has been

referred to in the past as Rift B (Embley et al., 1983; Morten et al., 1987) and the Shingle segment (Kappel and Ryan, 1986); Embley (in prep.), however, has suggested that this segment be named after the Vance seamount chain, which intercepts the ridge crest near 45°15'N, and his terminology will be used hereafter.

The southern end of the Vance Segment is offset 3 km to the west of the Cleft ridge segment at 45°03'N (Embley et al., 1983), and from there the ridge axis extends northward along a N20°E azimuth. The crest of the segment is marked by a 6 km wide axial valley that is walled by boundary faults up to 120 m high (Embley et al., 1983). The axial valley is centrally located between the Brunhes/Matuyama magnetic reversal boundaries (Delaney et al., 1981), and is symmetrically flanked by two pairs of linear hills that are oriented parallel to the ridge crest. A central ridge 80-100 m high extends along most of the length of the valley (Embley et al., 1983; Kappel and Ryan, 1986), and very fresh sheet flows, lobate flows, and low-temperature hydrothermal deposits have been observed on the central ridge near a split volcano at 45°12'N (Embley et al., 1983). Based on sidescan sonar images, Kappel and Ryan (1986) concluded that the central ridge is a constructional volcanic feature, and inferred that it is growing over the axis of spreading.

Results from previous studies of the central segment of the Juan de Fuca ridge near Axial Volcano (between 45°30'N and 46°30'N) suggest that the divergent boundary between the Juan de Fuca and Pacific plates here is offset 15 to 20 km west of the spreading segments to the north and south. Delaney et al. (1981) found neither fresh glassy basalts, symmetrical axial bathymetry (based on seismic reflection data), nor a definitive axial magnetic signal along the geometrical centerline between the Brunhes-Matuyama (B-M) magnetic reversal boundaries between 45.5°N and 46.5°N. However, fresh volcanics were dredged along a linear trend 13 km west of the B-M bisector. Since the B-M magnetic reversal boundaries are not offset in this area, Delaney et al. (1981) inferred that the zone of active volcanism, which may represent the axis of spreading, shifted to the west after 0.7 Ma.

This shift may have been a response to renewed activity of the Cobb-Eickelberg (C-E) hotspot. The movement of the Pacific plate over the C-E hotspot has built the Cobb-Eickelberg seamount chain, which is composed of volcanoes that increase in age towards the northwest. The Juan de Fuca ridge has been migrating N25°W at 30 mm/yr with respect to an absolute (hotspot) reference frame for at least 10 Ma (Davis and Karsten, 1986), and has steadily encroached upon the site of seamount production above the C-E hotspot (Davis and Karsten, 1986; Karsten and Delaney, 1986). The decreasing separation between the hotspot and the spreading

ridge is indicated by the decreasing age difference, progressing from west to east along the seamount chain, between each successive seamount and the crust upon which it sits (Desonie and Duncan, 1986). The increasing proximity of the ridge to the hotspot through time is also reflected by the morphology of the seamounts in the Cobb-Eickelberg chain. Young seamounts display a more elongate, ridge-parallel shape than the older seamounts (Karsten and Delaney, 1986). This relationship is evident between Cobb, Brown Bear, and Axial Seamounts: Cobb is 1.3 Ma old, sits on 4.5 Ma old crust, and has a conical shape; Brown Bear formed after 1.0 Ma on crust 1.5 - 2.0 Ma old, and is elongate parallel to the surrounding tectonic fabric; and Axial Volcano, still in the throes of construction, displays even more ridge-parallel elongation. Karsten and Delaney (1986) interpreted the different shapes of successive seamounts to be the result of the interaction of the radially symmetric hotspot stress field with the uniaxially symmetric ridge crest stress field.

Following a period of volcanic quiescence after the completion of Brown Bear Seamount, renewed output by the hotspot may have shifted the zone of active spreading westward (Delaney et al., 1981) and constructed Axial Volcano on, or very near, the axis of spreading (Hammond et al., 1987). Based on an analysis of the tectonic fabric surrounding Axial Volcano, Hammond and Delaney (1985; and in prep.) concluded that the initial volcanism on Axial volcano, and the westward jump of the ridge segment, commenced between 250 ka and 550 ka.

High-resolution SeaBeam bathymetry reveals a linear ridge that extends 50 km south of the summit of Axial volcano (Figure 2), and a similar ridge extends northwards from the volcano's summit. These are Axial volcano's north and south rift zones. Both ridges exhibit bilateral topographic symmetry about their long axes, which has been cited as evidence to indicate that crustal extension is presently active, or has been very recently active, along the rift zones (Hammond and Delaney, 1985). Embley et al. (1983) noted that the morphology of the southern Axial rift zone is more complicated than the rifts of the southern Juan de Fuca spreading segments, and attributed the complexity to the proximity of the Cobb-Eickelberg hotspot. Complex topography at the distal southern end of the south Axial rift zone has been interpreted as the possible location of a transitional zone where the tip of the rift zone overlaps the more 'normal' Vance spreading segment to the south (Hammond et al.,1987). Hammond et al. (1987) suggested that the Axial volcano rift zones could also be analogous to the major, long-lived rift zones typically associated with large submarine and subaerial basaltic shield volcanoes.

Figure 2. Regional SeaBeam bathymetry (50 m contour interval) of the south flank of Axial Volcano and the northern part of the Vance spreading segment. The boundaries of the SeaMARC I survey area are outlined, and the main geographical areas discussed in the text are labelled (WMR, Western Marginal Ridge; WOR, Western Outer Ridge; EMR, Eastern Marginal Ridge; EOR, Eastern Outer Ridge).

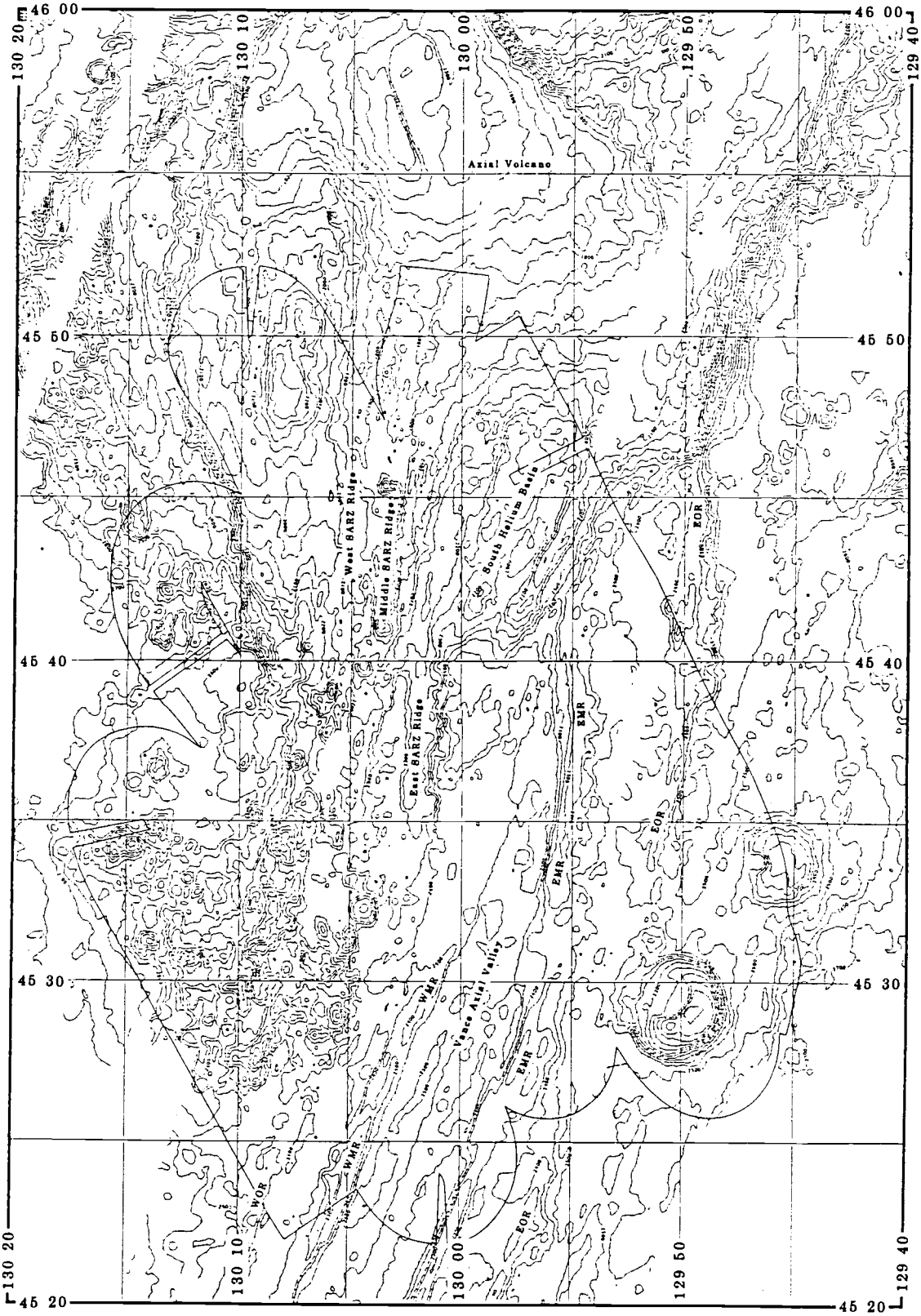
46 00
45 50
45 40
45 30
45 20
130 20
130 10
130 00
129 50
129 40
Axial Volcano
West BARZ Ridge
Middle BARZ Ridge
East BARZ Ridge
South Hollow Basin
Vance Axial Valley
WOR
WMR
EMR
EOR

Figure 2

Although the linear bathymetric highs that extend north and south of the summit of Axial volcano have been repeatedly interpreted as the possible site of the present-day spreading along the central segment of the Juan de Fuca ridge, the location of the spreading axis has not been unequivocally resolved. The purpose of this study is to utilize SeaMARC I sidescan sonar data to further define the spreading axis of the Juan de Fuca ridge in the area south of the summit of Axial Volcano (between 45°24'N and 45°50'N), as well as to elucidate the constitution and structure of the seafloor over the south Axial rift zone and southern flank of the main Axial volcanic edifice.

THE SeaMARC I SWATH MAPPING SYSTEM

SeaMARC I (SeaMARC is an acronym for **Sea**floor **Ma**pping and **R**emote **C**haracterization) is a deeply-towed, bilateral side-looking sonar mapping system that was jointly developed by scientists and engineers at the Lamont-Doherty Geological Observatory and International Submarine Technology of Redmond, Washington. The system was constructed to search for and locate the remains of the RMS *Titanic* (Farre, 1985), but has since been used as an effective tool for mapping the seafloor in a variety of geological settings. Detailed discussions of the development, design and operation of the SeaMARC I system have been presented by Chayes (1983), Kosalos and Chayes (1983), and Farre (1985); aspects of SeaMARC I pertinent to this study are presented below.

SeaMARC I is capable of insonifying the seafloor in swath widths of 500 m, 1 km, 2 km, or 5 km, depending on the degree of image resolution and survey rate desired. The 5 km swath width provided sufficient resolution for the scope of this study, and was exclusively used throughout this survey. In the 5 km swath width mode, the optimum operational ship speed is 2 knots, which results in a survey rate of 18 km^2/hour.

The overall SeaMARC I system may be separated into two primary components: the towed, submerged instrument platform (the SeaMARC "fish" or "vehicle") and the topside system for processing, displaying, and recording incoming data. The topside and subsea systems are connected by a single contrahelically armored coaxial conducting cable which serves the dual purposes of mechanically towing the sidescan fish as well as providing an electrical connection between the shipboard electronics and the towed instruments. Power, system commands, and gain settings are transmitted down the cable, while digital depth, pitch, heading, and analog acoustic data are telemetered up.

The Subsea System

The physical configuration of the SeaMARC I subsea system is shown in Figure 3. The towcable is attached to a 900 kg (in air) depressor weight, which in turn is connected to the SeaMARC I towfish by a neutrally buoyant umbilical 85 m long. The SeaMARC I towfish itself is 3 m long, 1.2 m wide, and 1.1 m high, and is made slightly buoyant with syntactic foam. As the system is towed through the water, the depressor weight occupies a position at the bottom of the towcable's

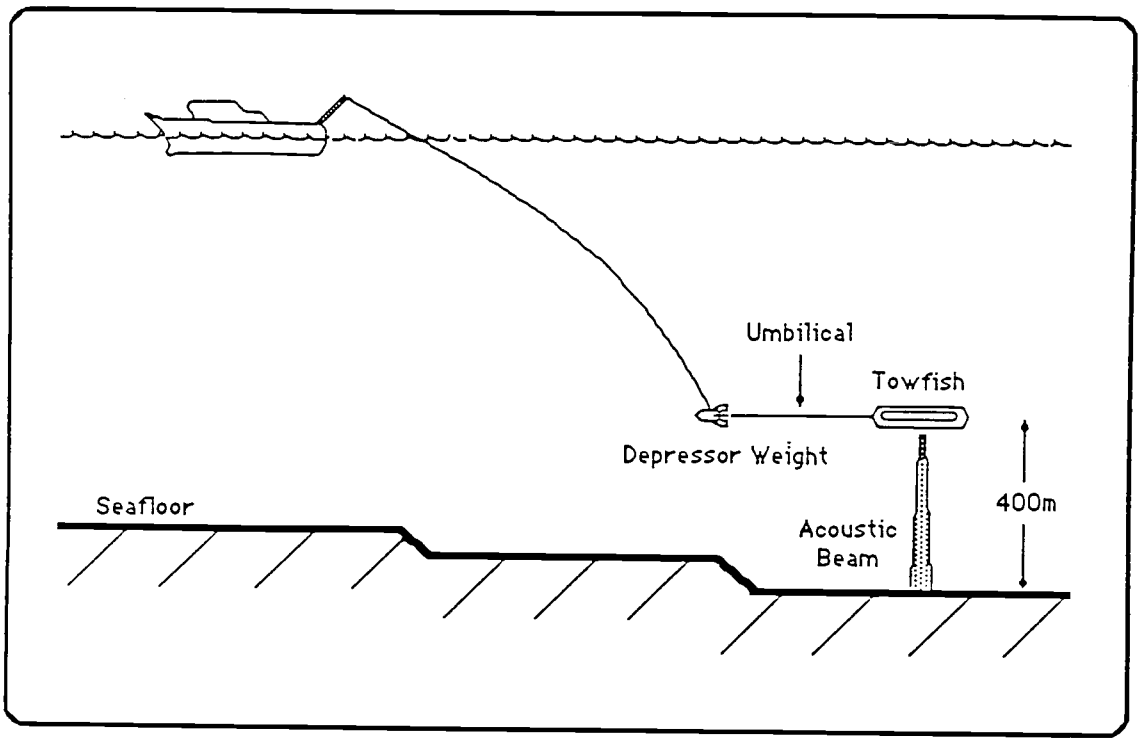

Figure 3. Physical configuration of the SeaMARC I sidescan sonar swath mapping system. The towfish and umbilical are neutrally buoyant and stream behind a depressor weight. This two-body towing geometry decouples the motion of the towfish from ship heave, and acts to passively stabilize the instrument platform. In the 5km swath-width mode (which was used exclusively throughout this survey), the sidescan vehicle is flown 350-400m above the seafloor.

catenary curve, and the towfish trails horizontally behind. The geometry of this relatively complicated 2-body towing scheme acts to passively stabilize the instrument platform and decouple the towfish from the motion of the ship (Chayes, 1983). Towfish stability is critical in the acquisition of sharply-focused wide-swath sidescan images of the seafloor; this towing configuration, although complicating the launch and recovery procedures, minimizes vehicle pitch and yaw.

The system's primary acoustical sensors, port and starboard side-looking sonars, are mounted with the long axes of their transducer arrays parallel to the long axis of the towfish. The sonars operate at slightly different frequencies, 27 kHz port and 30 kHz starboard, so that both sides of the swath may be insonified simultaneously without interfering with one another. The SeaMARC I system can be selected to transmit an acoustic pulse every 0.5, 1.0, 2.0, or 4.0 seconds, depending on whether the 500 m, 1 km, 2 km or 5 km swath width is employed. For each transmit cycle, an acoustic beam is emitted perpendicularly from the long axis of each of the transducer arrays (and thus perpendicularly from the heading of the towfish); each beam has an included horizontal angle of 1.7°, and an included vertical angle of 50°. This beam geometry insures that the area insonified by each transmit pulse is wide in the across-track direction, and narrow in the along-track direction.

Mounted within the frame of the towfish are the rest of the system's sensors: a 4.5 kHz down-looking subbottom profiler; a two-axis inclinometer that measures the vehicle's attitude; a bulk semiconductor strain gauge that measures pressure, from which the vehicle depth is calculated; and a gimballed fluxgate compass that measures the heading of the vehicle.

The SeaMARC I telemetry system is composed of two subsystems: 1) a full duplex digital communication system that sends system commands downlink, and transmits high resolution digital data uplink at a low data rate; and 2) an analog telemetry system that transfers acoustic data uplink at a high data rate (Kosalos and Chayes, 1983). Digital data includes towfish pitch and roll, towfish heading, and towfish depth data. Analog acoustic signals are transferred uplink via spectrally isolated channels of appropriate bandwidth and dynamic range for each signal: the subbottom profiler has 2 kHz bandwidth and 70 dB dynamic range; each sidescan channel has 5 kHz bandwidth and 70 dB dynamic range (Kosalos and Chayes, 1983; Farre, 1985).

Prior to uplink transmission, the sidescan signals are normalized in gain to correct for losses due to spherical spreading (an inverse-square-law phenomenon)

and attenuation within the water column. This enables the available dynamic range of the telemetry system to be maximized. Attenuation of acoustic energy within the water column increases roughly as the square of the frequency, so the total attenuation along a given raypath may be calculated as long as the slant range is known (Somers and Stubbs, 1984). For the operating frequencies of the SeaMARC I mapping sonars (27 and 30 kHz), the attenuation rate is roughly 9 dB km.

The Topside System

The shipboard SeaMARC equipment includes a telemetry system that decodes up-link digital data, and isolates, through band-pass filtering, the analog acoustic signals (Farre, 1985). Analog sidescan data are digitized and processed to correct slant-range, acoustic beam-pattern, and grazing angle distortions. Data from the 4.5 kHz subbottom profiler are also digitized and processed. Graphical recorders are used to display analog and processed sidescan images, and processed subbottom profiles, in real time. Data received during each transmit cycle -- including all processed acoustic data, vehicle attitude and depth measurements, and system commands -- are logged on 9-track magnetic tape.

Slant-range distortion is introduced into sidescan images because the sidescan transducers are towed above the ocean bottom, and transmit acoustic energy laterally and downwards to insonify a narrow strip of the seafloor. The slant range to a given target on the seafloor is therefore greater than the horizontal distance of the target from nadir. Horizontal range (R_h) is related to the slant range (R_s) by the relation

$$R_h = \sqrt{R_s^2 - h^2} \ ,$$

where h is the altitude of the towfish. In terms of two-way travel time, this relationship may be expressed as

$$T = \sqrt{t_0^2 + \frac{2R_h^2}{V_p}} \ ,$$

which is the equation of a hyperbola; T is the two-way slant-range travel time, V_p is the speed of sound through water, and t_0 is the two-way travel time to a point directly beneath the sidescan vehicle. Therefore if echo strength is displayed as a

gray-scale image in which echoes are assigned a shade of gray proportional to their magnitude and plotted at a distance from nadir proportional to their two-way travel time, individual targets will be displayed outboard of their true position by a distance that decreases towards the outside of the swath (Leenhardt, 1974; Flemming, 1976; Somers and Stubbs, 1984).

The SeaMARC I system applies a slant-range correction to remove much of this geometrical distortion by digitizing the received signal at a rate that decreases with time within each transmit cycle (Farre, 1985). The received backscatter echo sequence is thus redistributed as if it had returned from a planar, horizontal seafloor located below the towfish at a distance equal to the towfish altitude (Kosalos and Chayes, 1983). Since the seafloor is not actually flat, this process introduces a small but acceptable degree of across-track spatial distortion into the resulting scanline.

An empirically derived beam pattern and grazing angle correction is also applied to each pixel along a scanline. Within each acoustic beam, the strength of the outgoing signal along a given raypath varies according to the position (or *takeoff angle*) of the raypath within the vertical plane of the beam. Given a uniform seafloor roughness, the variation in outgoing acoustic strength causes the amount of energy available to be backscattered along the scanline to vary. Upon reaching the seafloor, the proportion of energy backscattered decreases as the grazing angle decreases (McKinney and Anderson, 1964). The grazing angle is the complement of the incident angle, so the degree of backscattering decreases away from the center of the swath. The corrections applied to account for these phenomena are strictly a function of angle -- takeoff angle and grazing angle -- and are based on the planar seafloor assumption (Farre, 1985). Once again, topographic undulations of the seafloor introduce slight but acceptable errors into the corrections.

Image Resolution

A sidescan sonar image is a visual representation of the strength of acoustic backscattering from the seafloor mapped onto a two-dimensional image medium . Sidescan sonar images are similar to images produced by aerial photographs and synthetic-aperture radars, in that they are shades-of-grey diagrams (or false-color images) high in horizontal resolution but with little 3-D information (Vogt and Tucholke, 1986).

Sidescan data are collected in two directions: perpendicular to the track of the towfish, and parallel to it. Sidescan sonars iteratively insonify narrow strips (or

scanlines) of seafloor with discrete pulses of acoustic energy, and measure the returning echo as a function of time. Each scanline is oriented orthogonally to the trackline of the sidescan vehicle. On the seafloor, individual scanlines are separated by an along-track distance equal to the distance the towfish travels between each acoustic pulse. SeaMARC I digitizes each scanline into a row of 2048 pixels, and assigns each pixel a numerical value that corresponds to its echo magnitude. Numerical backscatter values range from 0 for high backscatter to 255 for no backscatter (acoustic shadow). Once digitized, scanlines are processed to correct slant range, beam pattern, and grazing angle distortions, and may be displayed on either a graphic recorder or image processor. By displaying a series of successive scanlines, a two-dimensional image of the backscatter characteristics of the surveyed seafloor is constructed, with one axis proportional to the across-track horizontal range, and the other axis proportional to the forward progress of the sidescan vehicle over the seafloor.

The resolution of a sidescan image is different in the along-track and across-track directions. Resolution, as defined by Flemming (1976), is the minimum distance between two objects that are recorded by the sidescan as separate objects. Across-track resolution (the range resolution, R_r) is approximated by $V_p \tau /2$, where τ is the acoustic pulse length, and V_p is the speed of sound through water (Somers and Stubbs, 1983). The bandwidth of the acoustic signal determines its slant-range measuring ability; since bandwidth and pulse length are inversely related, a narrow pulse results in a broad spectrum, and therefore resolution is related to bandwidth as $1/\tau$ (Vogt and Tucholke, 1986).

In order to avoid image across-track smearing between pixels, SeaMARC I employs a pulse length that yields a range resolution approximately equal to the image pixel width. Since scanlines are digitized into 2048 pixels, the across-track width of each pixel in a 5 km-swath-width scanline is $\approx$ 2.4 m. In the 5 km swath width mode, SeaMARC I transmits a 3.2 ms pulse, which yields a range resolution of about 2.4 m.

The along-track resolution (or transverse resolution, R_t) is determined by either the width of the acoustic beam on the seafloor, or the distance travelled by the transducer between each acoustic pulse, whichever produces the minimum result. The along-track dimension of the acoustic footprint on the seafloor is a function of the horizontal beam angle and the distance of the insonified area from the sonar transducer. Each SeaMARC I transducer array, port and starboard, emits a formed acoustic beam having a 1.7° included angle in the horizontal plane. Due to this

horizontal beam angle, the width of the scanline progressively increases outboard from nadir. Beam width (B_W) at a given slant range distance (R_S) is

$$B_W = \sin\phi \, R_S$$

where ø is the horizontal beam angle. At an altitude of 300 m, the along-track pixel width therefore ranges from 9 m beneath the towfish to 75 m at the outer limit of the 5 km swath. The minimum distance between two resolvable targets is equal to the beam width at any particular point on the seafloor, resulting in a steady decrease of the transverse resolution away from the center of the swath (Flemming, 1976).

DATA PROCESSING

The ideal final product of a sidescan sonar survey is a geometrically corrected, consistently scaled mosaic (Telecki et al., 1981). Accordingly, the primary emphasis of the data reduction process involves generating a digital, navigated sidescan data set that can be used to plot orthorectified sidescan images directly onto an absolute (latitude/longitude) reference grid. A digital data set is desired because digitally processed sidescan images may be merged with navigation data, efficiently stored, rapidly retrieved, and redisplayed at a variety of scales. As a result, much more information may be extracted from digital data than from analog data.

Digitally stored, navigated SeaMARC I data afford the capability to construct computer-generated mosaics from adjacent or overlapping sidescan images. An accurate mosaic of sidescan imagery is a useful interpretive tool, since the proper alignment of adjacent swaths permits the integrity of areally extensive features to be maintained from swath to swath. Image continuity between swaths is especially important within this survey because tracklines are oriented oblique to the regional N20°E structural fabric, and many ridge-parallel structures extend across several swaths. Sidescan mosaics also enable a regional perspective to be gained that cannot be conveyed by single swaths. Several previous studies have demonstrated the utility of sidescan mosaics in the interpretation of both the structure of the seafloor and the geological processes responsible for generating the observed morphologies (e.g., Mudie et al., 1973; Somers and Stubbs, 1984; and Prior et al., 1979), and Prior et al. (1979) predicted that the ability to image the seafloor in true dimensions will ultimately contribute as much to the field of marine geology as aerial photography did to subaerial topographic mapping.

Computer-produced mosaics of digital sidescan data offer several distinct advantages over manually-produced mosaics of analog data. The computer process utilizes a consistent, objective algorithm to construct a reproducible final image, eliminating the subjectivity inherent in the manual construction of mosaics. Adjacent sidescan swaths may be more precisely matched when fitted together by computer (Telecki et al., 1983), and the resulting digital format of the mosaic is able to support processing operations that are impossible to perform on analog data. For instance, digital mosaics may be efficiently stored on magnetic tape, quickly retrieved, and plotted at a variety of scales and projections (Mercator, Universal Transverse Mercator, etc.). Image processing techniques may be applied to digital sidescan

data, allowing the imagery to be enhanced and manipulated in order to resolve subtle backscatter variations and structural patterns. Digital sidescan data are amenable to quantitative analyses that will ultimately permit operations such as seafloor texture classification and object detection to be performed, which are impossible to execute on analog data. Digitally stored sidescan images will also allow temporal variations in the bottom topography or texture to be recognized in areas that are surveyed more than once (Vogt and Tucholke, 1986), and, when digital sidescan surveys are conducted over the same site on a regular basis, will provide a means for actually monitoring the evolution of the morphology of areas where volcanic, tectonic or erosional processes are active.

A sidescan image is a combination of the small scale reflecting properties of the bottom (the "roughness" of the bottom) and the specular reflections from bathymetric slopes, and one of the inherent limitations of sidescan sonar is its inability, in some cases, to discriminate between the two (Blackinton et al., 1983; Farre, 1985). However, sidescan and bathymetric data used in concert permit reflectivity variations due to topographic relief to be differentiated from those due to lithology or surface roughness of the seafloor. Since digital, navigated sidescan mosaics may be plotted directly onto a latitude/longitude grid, detailed SeaBeam bathymetric data may be superimposed on the sidescan imagery, facilitating the comparison of the two data sets. Ancillary geophysical data such as magnetics, gravity, and seismic reflection may be similarly integrated with digital sidescan mosaics for correlative analyses (Paluzzi et al., 1981; Telecki et al., 1981).

Navigating the Path of the Sidescan Vehicle

Since the location and orientation of the sidescan vehicle must be known at the time of each sonar pulse in order to assign absolute positions to individual sidescan pixels, significant emphasis was placed on developing a means for navigating the position of the SeaMARC I instrument package. Although methods exist for acoustically determining the position of deeply-towed instruments via bottom-moored transponder networks (discussed by Boegeman et al., 1972), or ship-based ultra-short baseline systems (one example is presented by Ransford and Ioupp, 1987), none of these systems were available during this survey. However, the general tracking behavior of the SeaMARC I vehicle is known from previous surveys conducted within transponder nets. The towfish typically tracks directly aft of the ship during straight sections, and follows a path inside the trackline of the ship

during turns. Similar tracking relationships have been documented for deeply-towed instrument platforms in other studies (e.g., Ivers and Mudie, 1973; Farre, 1985; Le Guerch, 1987). Using these observations as guides, a simple numerical model was constructed to describe the tracking behavior of the towfish behind the ship in order to estimate successive positions and orientations of the sidescan vehicle.

Towfish positions relative to the ship were calculated for each sonar pulse (every 4 seconds for the 5 km swath mode) using fish-depth and ship-to-fish slant range data, and were assigned latitude and longitude coordinates based on the Loran-C ship navigation. Sidescan vehicle depth was measured with a bulk semiconductor strain gauge mounted on the frame of the vehicle, and was recorded topside on magnetic tape for each transmit cycle. Slant ranges to the fish were determined at 30-second intervals by acoustically interrogating a relay transponder attached to the sidescan tow cable and converting the two-way travel time to meters. Both data sets were postprocessed using a computer-assisted graphical editor to remove spurious points, and low-pass filtered to remove high frequency variation from the data.

The horizontal ship-to-fish distance may be regarded as a radius that defines a circle about the ship (Figure 4). The position of the sidescan vehicle is constrained to the perimeter of the circle, but without additional data the actual point on the circle that corresponds to the vehicle's position cannot be resolved. However, assuming that the towfish follows the ship as if it were attached to a rigid wire that responds only to the movement of the ship, the position of the fish on the circle may be uniquely determined if the previous fish position is known. For example, consider the case presented in Figure 5, in which a ship and towfish move from their initial (time=t_1) positions, which are both known, to new (time=t_2) positions, of which the ship position is known but the towfish position must be derived. Figure 5a shows the positions of the ship and towfish at t_1. The ship advances to a new position at t_2 (Figure 5b), pulling the towfish to a new, unknown position. The horizontal ship-to-fish distance is calculated at t_2 and is used to define a circle around the t_2 ship position (Figure 5c). The position of the towfish at t_2 is determined by drawing a line from the ship position at t_2 to the t_1 towfish position; the point where this line intersects the circle marks the location of the towfish at t_2. The new towfish position is derived mathematically by simultaneously solving the equations for a circle and a line,

$$r^2=(x_2-a)^2+(y_2-b)^2$$

$$y_2=(x_2-x_1)+y_1$$

Figure 4. Schematic diagram of the method used to determine the horizontal distance of the towfish from the ship. A) The horizontal distance of the towfish from the ship may be calculated from the depth of the sidescan vehicle and the slant range of the fish from the ship. B) The towfish lies somewhere on the perimeter of a circle that is centered on the ship and has a radius equal to the horizontal ship-to-fish distance. The precise position of the towfish on the circle cannot be uniquely determined from this information alone -- additional data is required to constrain the location of the towfish on the perimeter of the circle.

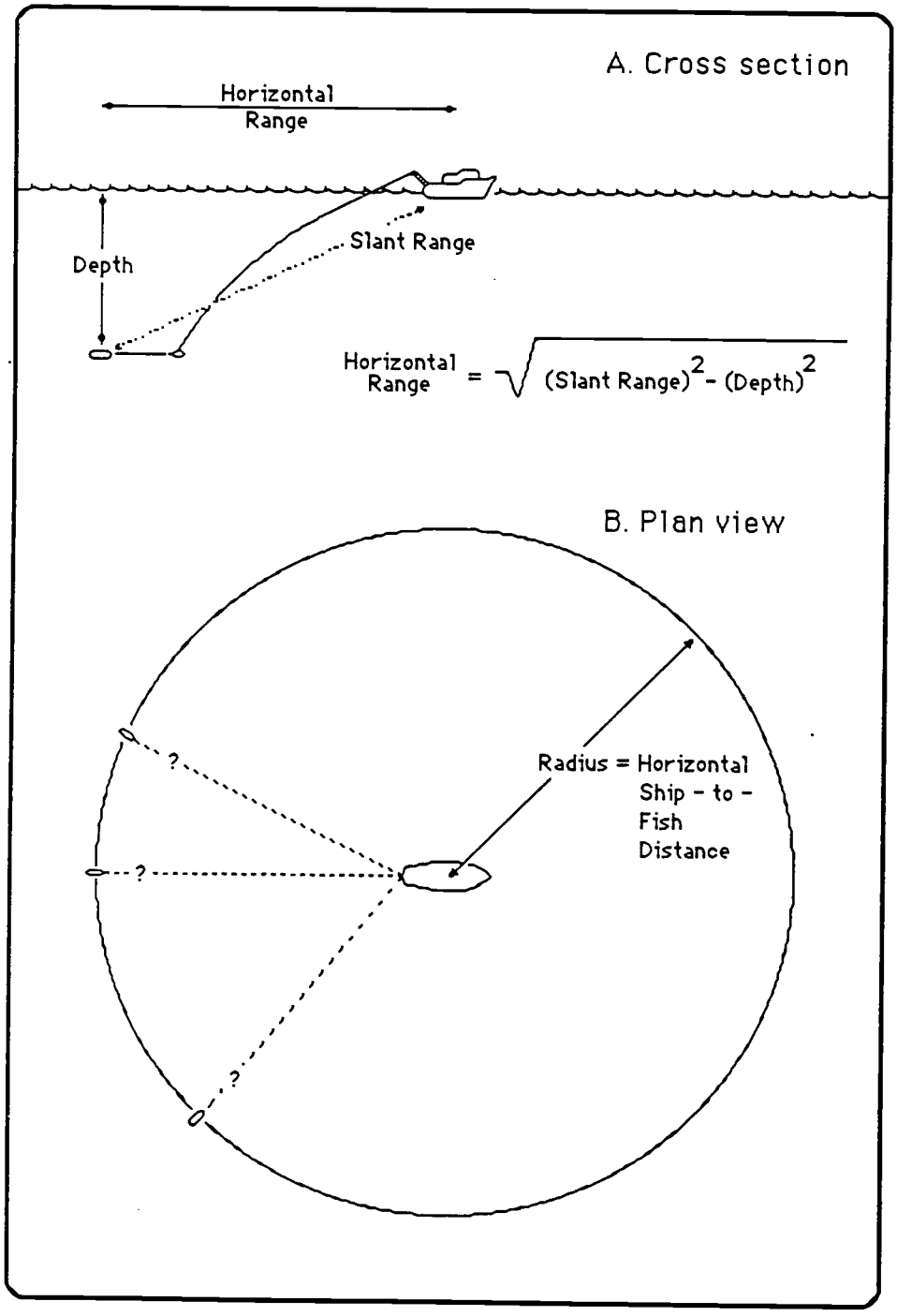
A. Cross section
Horizontal
Range
Depth
Slant Range
Horizontal
Range
=
(Slant Range)2 - (Depth)2
B. Plan view
Radius = Horizontal
Ship - to -
Fish
Distance
?
?
?

Figure 4

Figure 5. Step-by-step illustration of the process used to estimate the position of a towed instrument behind the ship, given that the previous towfish position is known, and assuming the towfish responds to the movements of the ship as if the towfish and ship were connected by a rigid cable.

A) The initial ship and towfish positions are shown -- the ship is represented by a hollow square, the towfish by a hollow triangle.

B) The ship advances from its initial position at t_1 to a new position at t_2 (shown by a solid square). The position of the towfish at t_2 is unknown and must be determined.

C) The horizontal range of the towfish from the ship is calculated for t_2 and is used to define the radius (r) of a circle about the position of the ship at t_2. The towfish position at t_2 lies on the perimeter of the circle, although its precise location is not yet constrained.

D) A line is drawn between the ship position at t_2 to the towfish position at t_1. The intersection of this line with the circle around the ship marks the location of the towfish at t_2.

E) The positions of the towfish and ship at t_1 and t_2 are shown. The hollow triangle and square are the t_1 positions of the towfish and ship, respectively, and the solid symbols represent their t_2 positions.

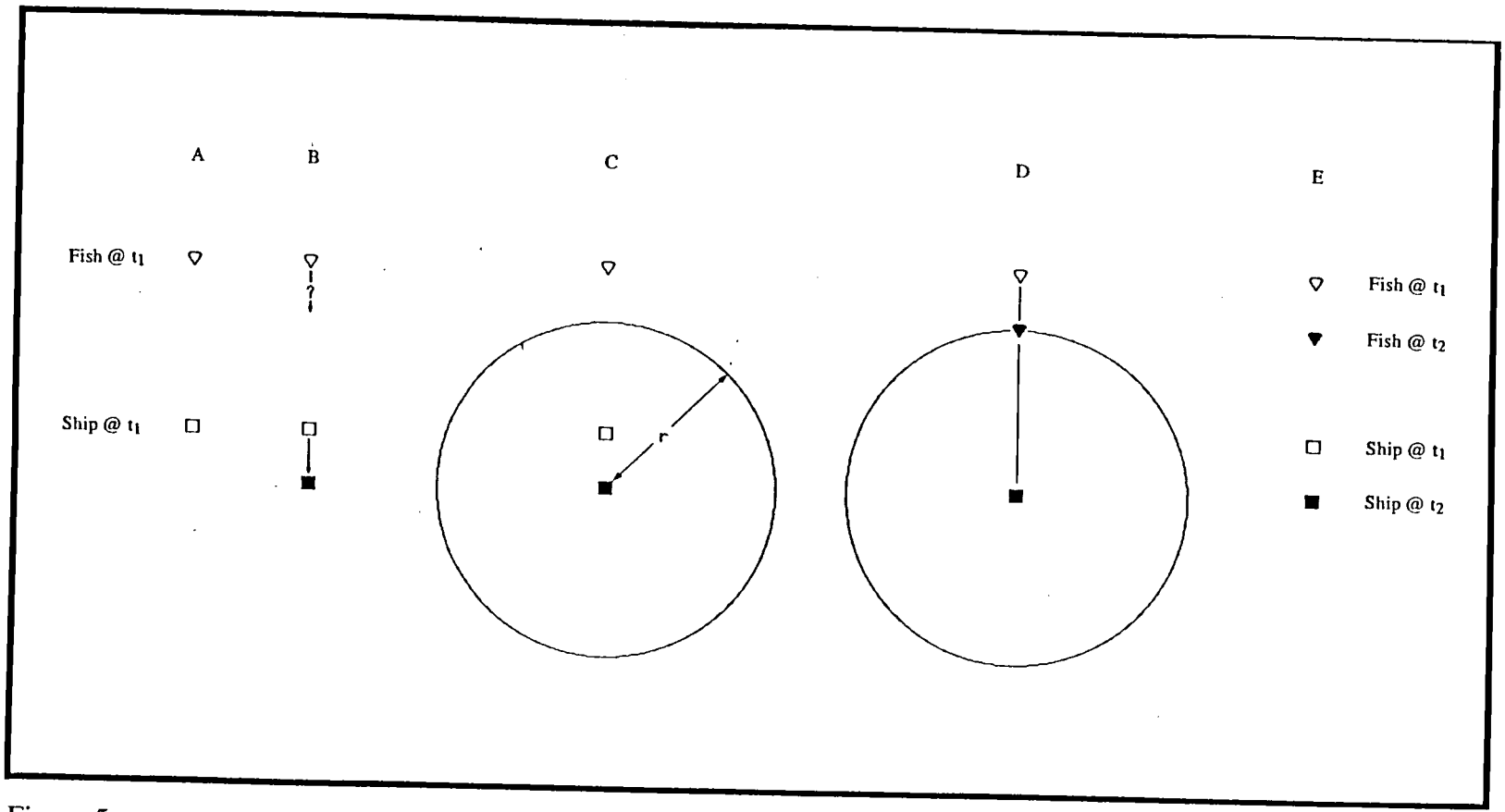

Figure 5

where a and b are the longitude and latitude of the ship at t_2, r is the horizontal distance of the fish from the ship, x_1 and y_1 are the longitude and latitude of the fish at t_1, m is the slope of the line connecting the fish position at t_1 to the ship position at t_2, and x_2 and y_2 are the longitude and latitude of the fish at t_2. The quadratic form of these equations results in two solutions for the position of the fish, one in front of the ship, which is ignored, and one behind the ship, which is selected as the fish position at t_2.

The path of a towed body that results from this model is diagrammed in Figure 6. At a given time *t* , the instantaneous towfish position occupies the intersection between an arc defined by the horizontal ship-to-fish distance at time *t* with a line that connects the ship position at time *t* to the towfish position at time *t* -1. Successive ship and fish positions (represented by squares and triangles, respectively) are numbered to indicate coeval instantaneous positions, and the direction of progress is shown by arrows. To best illustrate the tracking characteristics of the towfish, the horizontal ship-to-fish distance and the separation between ship positions were held constant. Between positions S_0 and S_1, the ship sails due south, and the fish position determined for F_1 lies on the ship's trackline. The model outlined above predicts that the towfish will continue to track directly behind the ship as long as the ship maintains a straight course. As the ship enters a 180° turn to starboard, however, the path of the towfish deviates from that of the ship, and the towfish negotiates the turn inside the trackline of the ship. As a consequence, successive fish positions become more closely spaced through the turn. At position S_{10} the ship exits the turn and resumes a straight course, and the towfish positions determined for F_{10} - F_{17} asymptotically approach the ship's trackline and progressively become more widely spaced.

This model incorrectly assumes that the towcable behaves rigidly, when in fact the cable flexes in response to changes in the ship's direction (Schram and Reyle, 1968; Cassarella and Parsons, 1970; Choo and Cassarella, 1972; Ivers and Mudie, 1973). Flexure of the towcable must be taken into account in the towfish navigation process in order to accurately determine successive towfish positions and orientations, and to construct properly rectified sidescan images. Most of the distortion introduced into sidescan images due to cable flexure may be eliminated by introducing a parameter into the navigation algorithm that dampens the response of the towfish to variations in the ship's track. Damping was accommodated within the navigation routine by modifying the procedure used to calculate the slope of the line that connects the F_{t-1} and F_t towfish positions (Figure 7). Instead of using the

Figure 6. Schematic diagram of the towfish trackline that results after a series of iterations of the model presented in Figure 5 as the towfish follows the ship through a 180° turn. Towfish positions are depicted by solid triangles, and ship positions are shown by hollow squares; each are labelled (F = towfish, S = ship) and numbered to indicate coeval instantaneous positions. The circle at the right, centered on the S_1 ship position, is defined by a radius (r) equal to the horizontal ship-to-fish distance. For clarity, arcs are substituted for circles throughout the rest of the diagram, and the ship speed and the horizontal ship-to-fish distance are held constant. The intersection of this circle with the line $\overline{F_0S_1}$ marks the location of the F_1 towfish position. Expressed generally, the intersection of the circle about the ship at S_t with the line $\overline{F_{t-1}S_t}$ marks the location of the towfish at F_t; this procedure was iterated for subsequent ship positions to construct the towfish path shown. Note that as the ship enters the turn, the towfish positions deviate from the ship trackline, and the towfish executes the turn inside of the path described by the ship. During the turn, the spacing between successive towfish positions decreases. After the ship exits the turn and resumes a straight course, the spacing between successive towfish positions increases, and the path of the towfish asymptotically approaches the trackline of the ship.

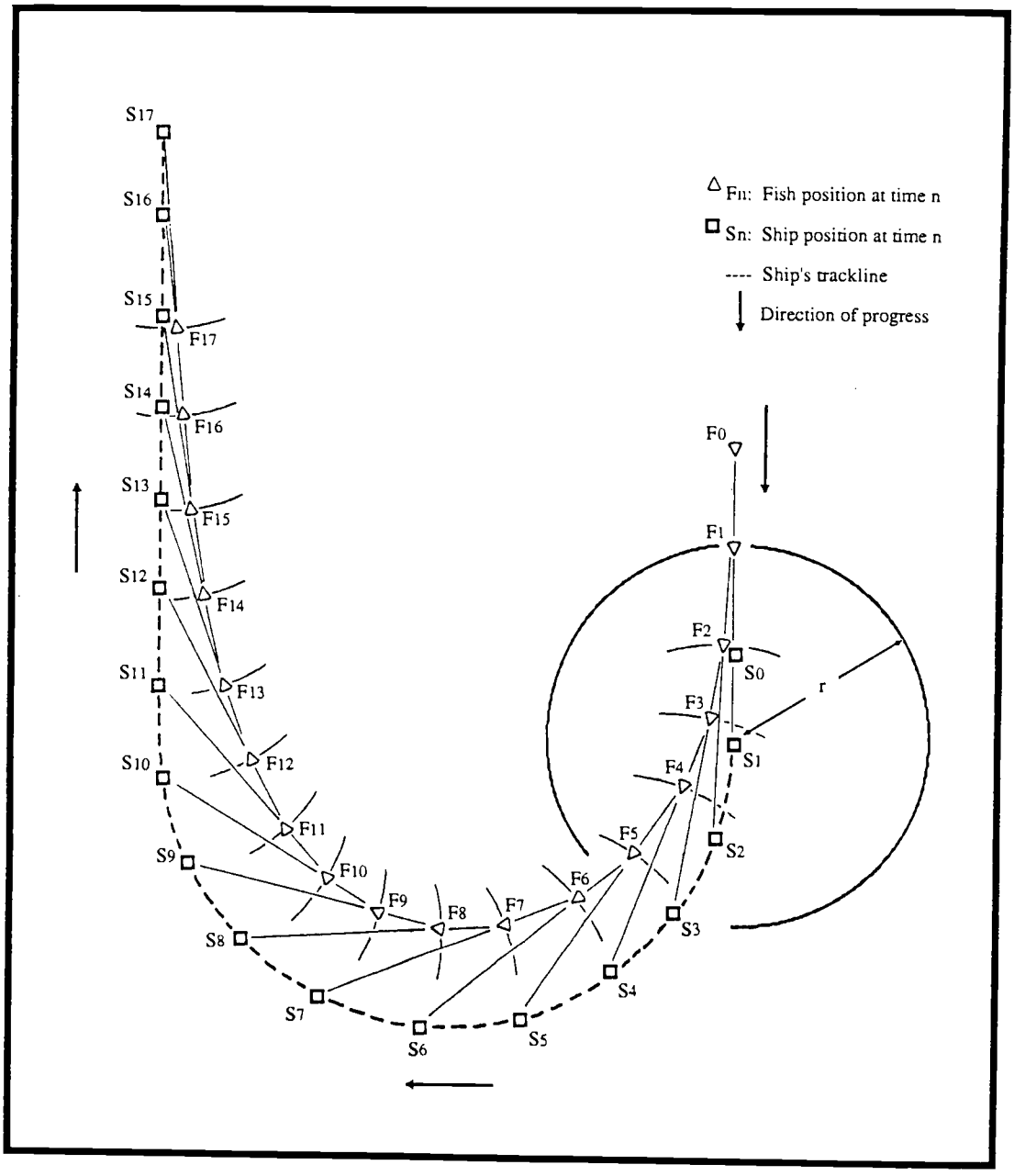
Fn: Fish position at time n
Sn: Ship position at time n
---- Ship's trackline
Direction of progress
S17
S16
S15
S14
S13
S12
S11
S10
S9
S8
S7
S6
S5
S4
S3
S2
S1
S0
F17
F16
F15
F14
F13
F12
F11
F10
F9
F8
F7
F6
F5
F4
F3
F2
F1
F0
r

Figure 6

Figure 7. Illustration showing the process for estimating successive towfish positions, modified from the simple rigid-wire model to account for flexure of the towcable.

A) Initial geometry of the fish and ship at t_0. The ship has advanced to its position at S_1, and the new (F_1) towfish position is to be solved. The heading of the towfish at t_0 (shown by an arrow) will be used to estimate the F_1 towfish position.

B) The horizontal ship-to-fish distance at t_1 is calculated, as is the bearing from the t_0 towfish position to the t_1 ship position. In the simple rigid-wire model, the intersection of this line with the arc defined by the horizontal ship-to-fish distance would have been used to define the fish position at t_1.

C) An average slope is calculated from the fish heading at t_0 and the line $\overline{S_1F_0}$, which is used to project a line from the fish position at t_0. The intersection of this line with the horizontal ship-to-fish distance at t_1 defines the towfish position at t_1.

D) Geometry of the the ship and towfish at t_1. The instantaneous heading of the towfish at t_1 will be used to estimate the next (t_2) towfish position in the next iteration of the navigation process.

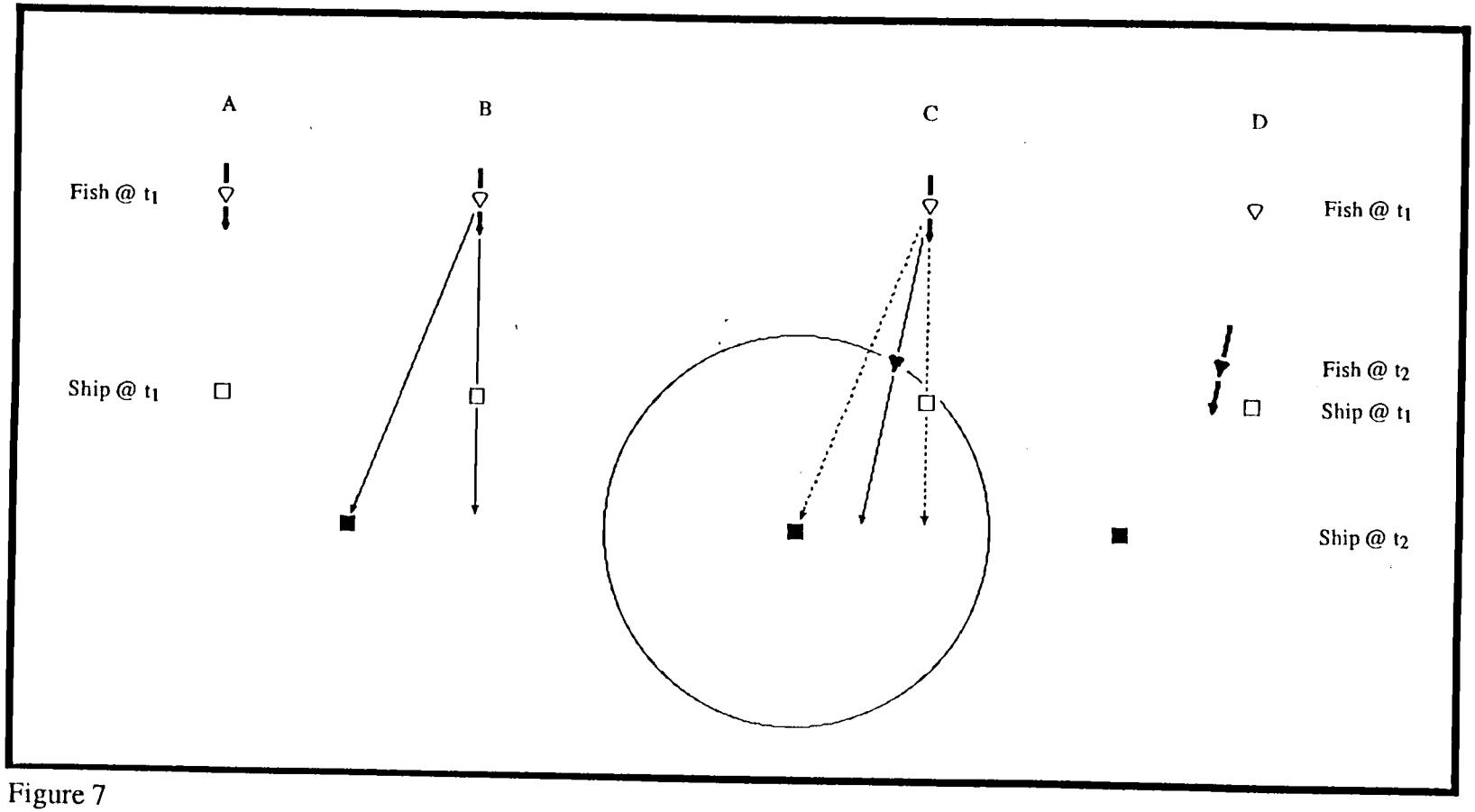

Figure 7

slope of the line $\overline{F_{t-1}S_t}$ to describe the towfish heading and determine the F_t towfish position, an average slope is calculated from the slope of the line $\overline{F_{t-1}S_t}$ and the slope of the towfish heading Δt minutes prior to F_t. This average slope is projected from the F_{t-1} towfish position to determine the F_t towfish position in the manner outlined for the 'rigid-wire' model. The resulting towfish trackline contains less high-frequency variation, follows the ship's trackline more closely, and, after exiting a turn, reassumes a position directly aft of the ship more quickly than the towfish trackline determined using the 'rigid-wire' model (Figure 8). In order to determine an optimum value for Δt, the vehicle navigation was iteratively processed using Δt values ranging from 0 to 15 minutes. A Δt value of 5 minutes yielded optimum results -- the sidescan mosaic generated using $\Delta t = 5$ minutes most accurately imaged the seafloor around major turns, and displayed the best-matched swaths -- and was used in the towfish navigation algorithm throughout the survey.

Gridding and Plotting Navigated Sidescan Imagery

Once the vehicle navigation process is complete, a planview sidescan image can be constructed that is free of distortion caused by deviations in the vehicle trackline and vehicle speed. First, the vehicle navigation is merged with the sidescan backscatter data using a program written by T-K Andy Lau at the National Oceanic and Atmospheric Administration's Marine Resources Research Division in Newport, Oregon. Merging is accomplished by combining the latitude and longitude of the towfish at the time of each ping with the sidescan data that was recorded for that time. Sidescan pixels are then mapped onto a latitude/longitude grid by "driving" the sidescan vehicle along its navigated trackline over a framework of square, equally sized, initially empty grid cells (Figure 9). Adjacent vehicle positions are used to calculate a fish heading for each transmit pulse. Square sidescan pixels are then projected from the vehicle position onto the grid along a scan line perpendicular to the fish heading. Individual grid cells may be registered by more than one sidescan pixel, depending on the grid cell size and the number of times a grid cell is insonified by different scan lines. Backscatter intensity values for individual sidescan pixels range from 0 (strong echo) to 255 (weak echo). The average backscatter intensity of each grid cell is determined by summing the intensity values of all the sidescan pixels that registered within each grid cell, and dividing that value by the number of pixels that fell within the grid cell.

Figure 8. Schematic illustration of the towfish trackline calculated according to the modified rigid-wire model. The ship's path is identical to that shown in Figure 6. The short line segments inboard and outboard of each towfish position represent the line $\overline{F_{t-1}S_t}$ and the F_{t-1} towfish heading, respectively. The F_t towfish position is located at the intersection of the S_t ship-to-fish distance (arcs) with the line that bisects the acute angle formed by the two line segments. Compare the path of the towfish in this figures with that shown in Figure 5: the fish trackline here follows the ship's path more closely, and enters and exits the turns at positions nearer to the point where the ship begins and ends the turn, than in the simple, rigid-wire model. As diagrammed in this figure, the time difference (Δt) between the saved fish heading and the fish position being solved is equal to on time increment (F_{t-1} vs. F_t). By varying the value of Δt, different towfish tracklines are calculated: greater Δt values result in a fish path that follows the course of the ship more closely; smaller Δt values result in a fish path that swings farther into the center of the turn.

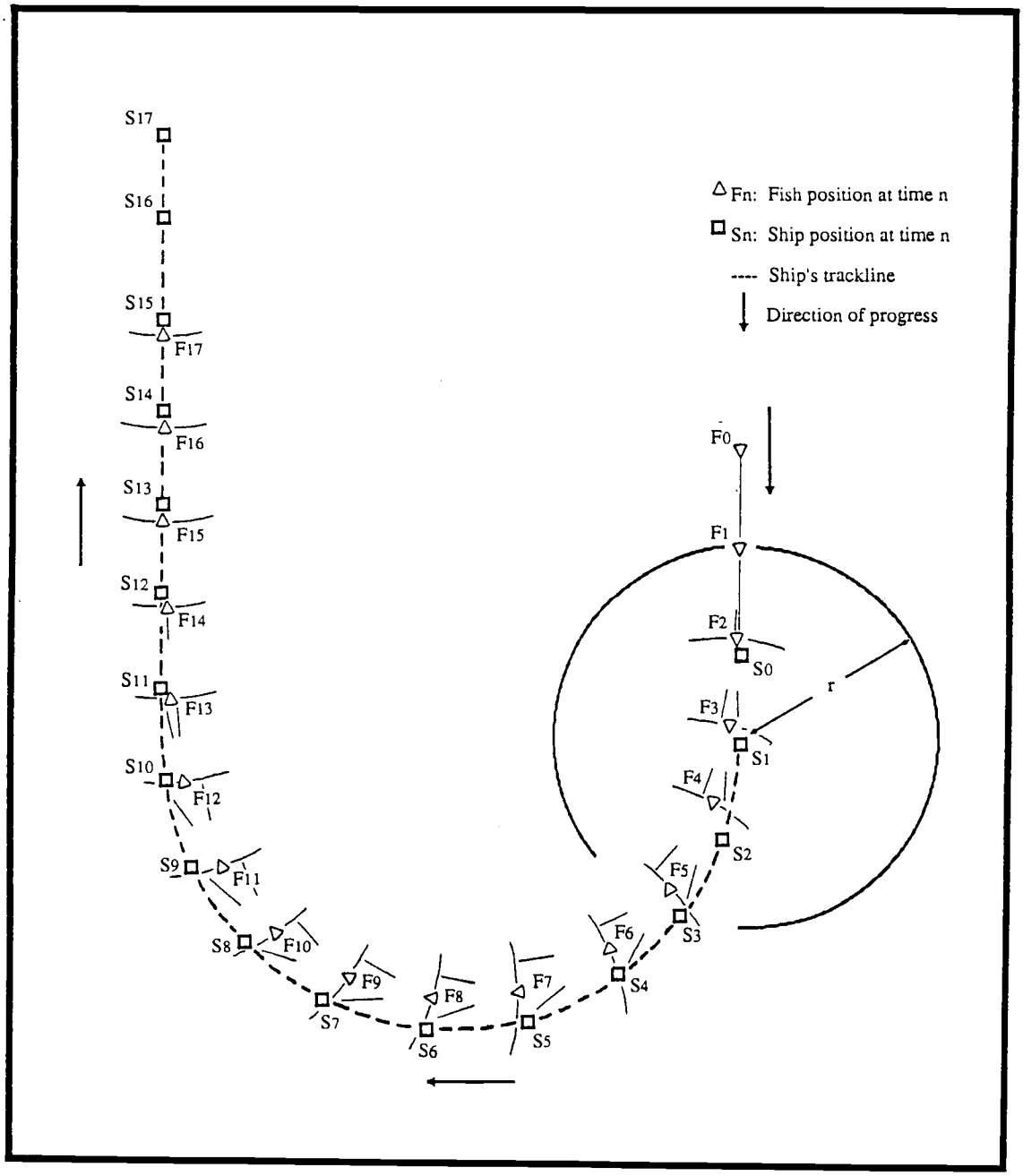
Fn: Fish position at time n
Sn: Ship position at time n
Ship's trackline
Direction of progress
S17
S16
S15
S14
S13
S12
S11
S10
S9
S8
S7
S6
S5
S4
S3
S2
S1
S0
F17
F16
F15
F14
F13
F12
F11
F10
F9
F8
F7
F6
F5
F4
F3
F2
F1
F0
r

Figure 8

Figure 9. Graphical representation of the computer process involved in gridding the digital sidescan data in order to construct a navigated sidescan image. An array of initially empty, square grid cells is defined over the geographical area of interest, using grid sizes appropriate for the resolution desired and the amount of data to be displayed (empty grid cells are shown in the upper left part of the figure). Successive scanlines are projected onto the gridded surface from the position of the towfish at the time of each acoustic pulse, with each scanline oriented orthogonally to the instantaneous towfish heading. Each scanline is composed of 2048 pixels, although for simplicity the scanline shown here contains only 18 pixels. The numerical backscatter intensity for each projected sidescan pixel is registered within every grid cell it overlies -- therefore an individual pixel may register within several grid cells. The number of pixels that register within each grid cell is used to calculate the average backscatter intensity for each grid cell, and the average backscatter intensity of each grid cell is displayed as a shade of grey, in this case with lighter shades corresponding to higher backscatter intensities. Since the grid cells display average backscatter intensities, the shades within individual grid cells do not necessarily correspond to the intensities of the sidescan pixels shown along the scanline. In this figure, the towfish is progressing towards the upper left corner, and the grid cells behind it have been registered by pixels and display average backscatter intensities, and the grid cells forward of the towfish have not yet been filled.

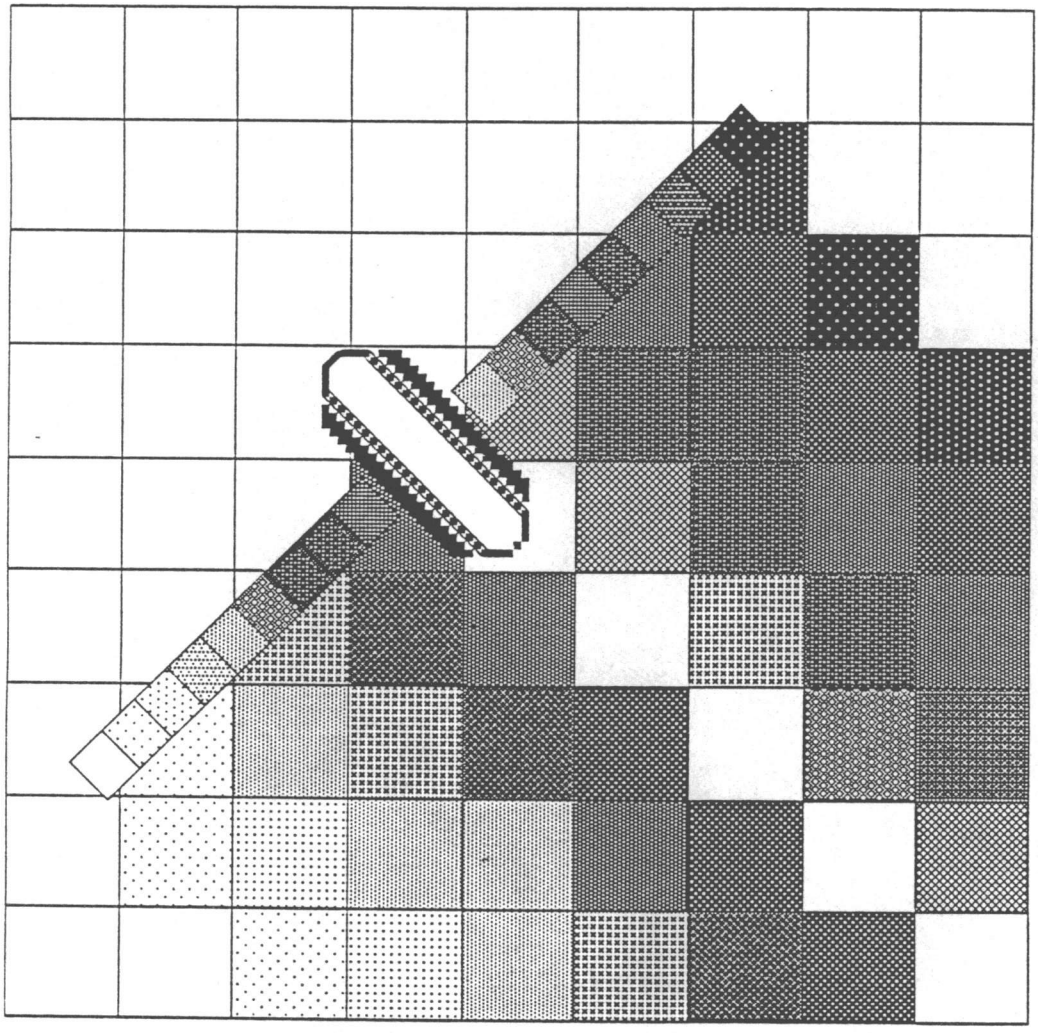

Figure 9

In order to prevent averaging bias in areas where sidescan swaths overlap, the gridding process limits the maximum number of pixels which are allowed to register within a given grid cell. The maximum number of pixels allowed to accumulate within each grid cell is user selectable, and varies with the grid cell size selected for a given plot. Figure 10 is an idealized cartoon of a sidescan mosaic, constructed from overlapping sidescan swaths, that shows how redundantly-insonified areas are displayed. Where regions are insonified by more than one swath, only the data from the first swath is displayed on the gridded sidescan mosaic.

The size of the grid cells used in the gridding process determines the resolution of the resulting sidescan image. Large grid cells are registered by a greater number of sidescan pixels than small grid cells, and therefore the backscatter intensity values calculated for large grid cells reflect a greater degree of pixel averaging than occurs for small grid cells. The gridding program treats the framework of grid cells as a two-dimensional array, so a given geographical area requires less computer storage space if it's covered by a small number of large grid cells rather than a large number of small grid cells. Each time a new plot is generated, the scale and geographic extent of the plot are taken into consideration in order to select a grid cell size such that the resolution of the resulting plot is maximized given the storage capacity of the computer. An enormous quantity of data is generated during a SeaMARC I survey (roughly 1.78 megabytes of raw data per hour, or about 309 megabytes of raw data in this data set), and large-scale plots require a significant amount of pixel averaging; the 1:100,000 scale plot of the entire survey area uses grid cells 20 m long by 20 m wide. Subsets of the data may be plotted with greater resolution, using smaller grid cells that average fewer pixels -- for instance, 1:20,000 scale plots are generated using 5 m x 5 m grid cells.

The accuracy of the navigated sidescan imagery was evaluated based on two criteria: 1) the internal consistency of the resultant sidescan image (that is, how well individual structures lined up between overlapping or adjacent swaths); and 2) the degree to which positions of structures in the sidescan mosaic correlated with the positions of their topographic expression in the SeaBeam bathymetry. Plate 1 (inside the pocket in the last page) is a mosaic of all the navigated sidescan data within the South Axial survey area, displayed in reverse black-and-white (white = high backscatter, black = low backscatter/acoustic shadow) at 1:100,000. Structures that extend between adjacent swaths consistently line up within 0-100 m of each other (note that when a scarp is insonified from opposite directions, it displays high

Figure 10. Cartoon showing the backscatter patterns that results when adjacent sidescan swaths are mosaicked together. Areas of high backscatter are represented by light stippling, and low backscatter is indicated by dark stippling. The sidescan vehicle is represented schematically, and the course it has followed is shown by the heavy dark line that bisects the swath behind it. The cross-sectional profile of the terrain is shown beneath the plan-view cartoon, which allows the relationships between backscatter patterns and topography to be seen. Scarps appear in the sidescan image as bands of either high or low backscatter, depending on whether the scarps face towards or away from nadir, respectively. Note that the sense of backscatter intensity over a scarp reverses where the scarp passes beneath the path of the towfish, and where the scarp passes between adjacent swaths. The circular features down the center of the figure are positive-relief structures; each displays a pattern of paired high- and low-backscatter zones, with high backscatter on the flank of the structure that faces nadir, and an acoustic shadow (low backscatter) on the side facing away from the sound source. The strip of seafloor in the region of overlap between the swaths is redundantly insonified; however, only the imagery from the vehicle's first pass is displayed. This is accomplished within the gridding algorithm by limiting the number of sidescan pixels that can register within a given grid cell. If the grid cells were permitted to accumulate an unlimited number of sidescan pixels, then high and low backscatter intensities associated with topographic features in the area of overlap would cancel each other out when the swaths are mosaicked together and backscatter intensities within grid cells are averaged.

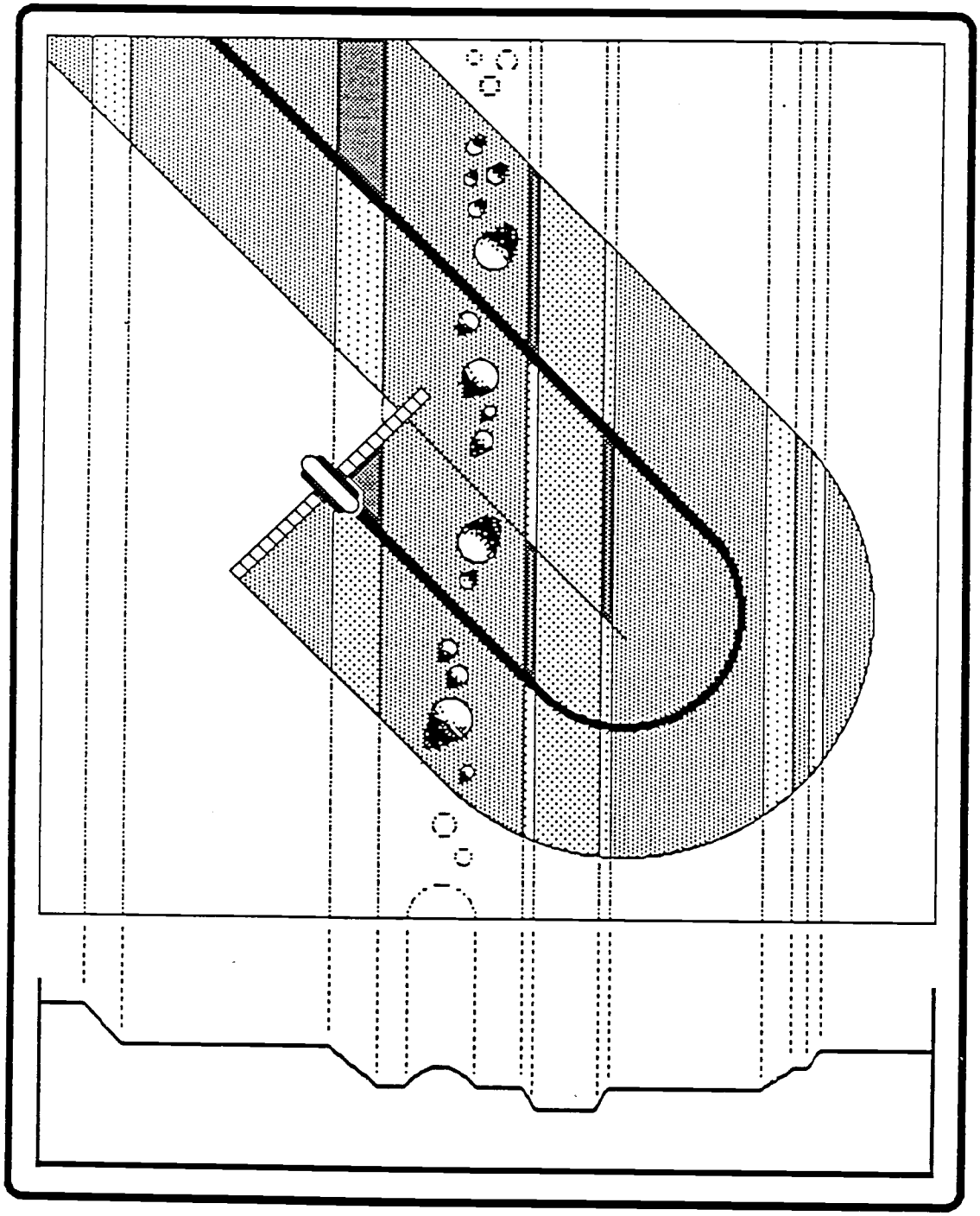

Figure 10

backscatter on the swath that images its face, and low backscatter or an acoustic shadow on the swath that looks from behind the top of the scarp down onto the seafloor below it). The offset between distinct structures on the sidescan imagery and SeaBeam bathymetry ranges from 0 to 150 m. However, the swath-to-swath offsets and the differences between the positions of structures on the sidescan and SeaBeam maps are not solely due to errors in the navigation; over rough topography, such as the seafloor within this survey area, the planar seafloor assumption used in the SeaMARC I slant-range correction is not valid, and cross-track distortions are introduced into the sidescan imagery. Without applying a sophisticated terrain correction, however, this distortion cannot be eliminated, and simply must be tolerated. For the purposes of this study, in which map scales of 1:100,000 and 1:20,000 were used to analyze the tectonic and volcanic processes over a large area, offsets of up to 150 m along adjacent swaths and between the sidescan mosaics and SeaBeam bathymetry are considered acceptable.

INTERPRETING SIDESCAN IMAGES

After an orthorectified sidescan mosaic has been constructed from data processed to minimize slant range, spherical spreading, grazing angle, and vertical-plane beam pattern distortions, the factors which influence the appearance of a sidescan image are limited to the surface roughness of the seafloor, and the acoustic impedance contrast between the water and the seabed material (Somers and Stubbs, 1983). The following section discusses the affects of the roughness of the seafloor and of the material properties of the seabed on the sidescan image, outlines important concepts for interpreting geological structures from sidescan mosaics, and presents several "type" examples of geological structures interpreted from sidescan data .

The spectrum of seafloor roughness has been shown to be continuous over a wide range of size scales (Fox and Hayes, 1985), and the relative roughness or smoothness of the seafloor, as perceived by a given sonar device, is dependent upon the sonar frequency used. Large-scale surface roughness refers to features having length scales many times that of the wavelength of the sonar, and describes the variation in the topography from the horizontal plane assumed when making the slant-range and grazing angle corrections (Blackinton et al., 1983; Somers and Stubbs, 1983). Large-scale roughness affects the degree of specular reflection either back towards or away from the sound source. For instance, surfaces that slope towards the sound source reflect a higher proportion of incident acoustic back to the sidescan vehicle than surfaces that are inclined away from the sound source (Blackinton et al., 1983). Small-scale roughness refers to features having length scales on the order of less than one wavelength of the acoustic signal (roughly 5 cm over the operational frequencies of SeaMARC I), and influences the amount of non-specular scattering of the incident acoustic energy (Blackinton et al., 1983), such that acoustically rough surfaces scatter more energy than smooth surfaces, some of which is directed back towards the sound source as *backscatter* (Vogt and Tucholke, 1986).

The amount of acoustic energy reflected from the seabed also depends on the contrast in acoustic impedance (the product of density by velocity) between the water and the seafloor (Dobrin, 1976). The reflection coefficient (R) gives the relative amplitudes of the incident and reflected waves, and can be expressed in terms of the acoustic impedance (z) in the form

$$R = \frac{z_2 - z_1}{z_2 + z_1}$$

where z_1 is the acoustic impedance of seawater, and z_2 is the acoustic impedance of the seabed material. Since the acoustic impedance of seawater is relatively constant, differences in the reflecting properties of the bottom from place to place may be attributed to material differences of the seafloor. In general, bare rock is a better reflector than sediment (Flemming, 1976) due to its higher seismic velocity and density.

Fundamental Concepts for Interpreting Backscatter Patterns

In order to assess the geological significance of sidescan backscatter patterns, the mode by which the sidescan data are graphically displayed must be specified. The sidescan images within this report are shown in reverse black-and-white, so that pixels containing the higheat backscatter values are white, and pixels that are within acoustic shadow zones (and therefore scatter back no acoustic energy) are black. The range of backscatter values between these two extremes are displayed in shades of grey, with increasing backscatter values corresponding to lighter (more white) shades.

The direction of insonification must be known in order to differentiate positive-relief structures from negative-relief structures, as well as to facilitate the interpretation of fault-generated scarps and constructional volcanic escarpments. As shown schematically in Figure 10, areas on the seafloor that are inclined toward the sound source reflect more acoustic energy back to the towfish than horizontal areas or regions that slope away from the sound source (McKinney and Anderson, 1964; Flemming, 1976). Therefore, positive-relief structures such as cones and ridges display high amplitude returns on the side closest to the sound source, and low amplitude returns (or a complete lack of reflected energy) on the side farthest from the sound source. Figure 11 shows two examples of positive-relief structures, (a) a circular structure rising up from a relatively flat seafloor, and (b) a ridge topped by a series of aligned cones.

Negative-relief structures, such as pits and fissures, display the opposite sense of backscatter and shadow: the nearer side displays low/no backscatter, and the farther side appears as a strong reflector. Figure 12a shows an example of a group of pits located on an otherwise smooth surface; Figure 12b is an image of a

Figure 11. Sidescan images of positive-relief structures. The direction of insonification is from right to left (the sidescan vehicle is to the right of the images), and high backscatter intensities are represented by light shades. A) A circular, flat-topped volcanic cone. High backscatter is recorded over the flank of the cone that faces the sidescan vehicle, and the seafloor behind the cone is cast in the acoustic shadow that results from the positive relief of the structure. The homogeneity of the backscatter intensity on the oval summit of the cone indicates that the surface of the top of the cone is relatively flat. A subtle depression is evident in the center of the summit plateau, marked by a region of slightly lower backscatter on the right side of the depression, and higher backscatter on the left. The cone overlies several small-offset fault scarps that face the sound source, evident on the lower part of the image. B) A volcanic ridge topped by several small aligned cones. The ridge extends from the upper right corner of the image to the lower left corner. The flank of the ridge facing the sound source displays slightly higher backscatter than the flat seafloor in the lower right part of the image. The cones along the crest of the ridge display the paired high- and low-backscatter patterns characteristic of round, positive relief structures: high backscatter marks the flank facing the sound source, and low backscatter (or complete acoustic shadow) is displayed over the flank facing away from the sound source.

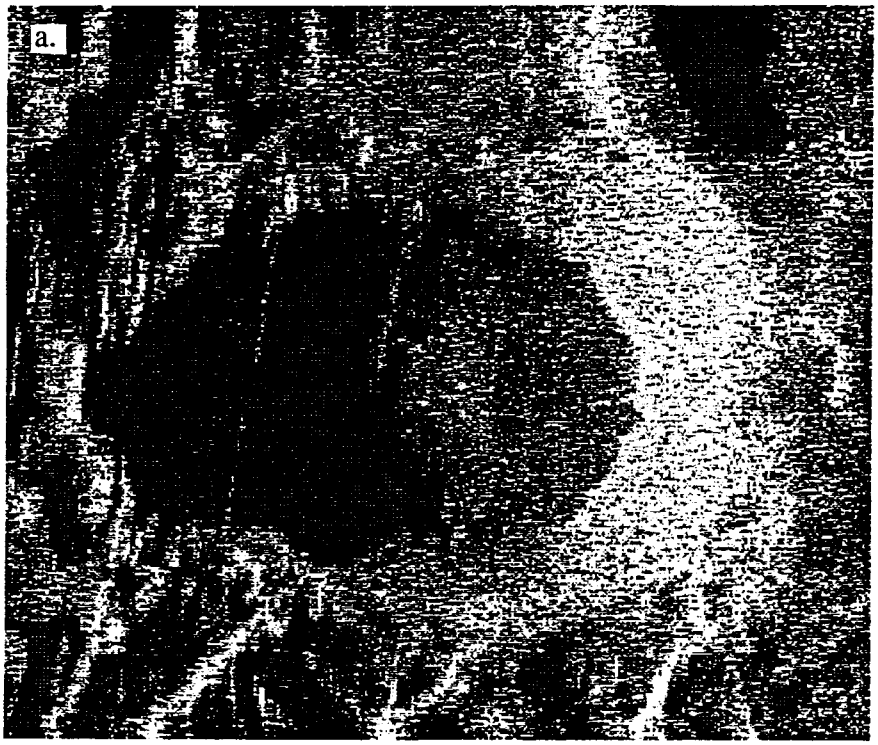

<--- INSONIFICATION ---

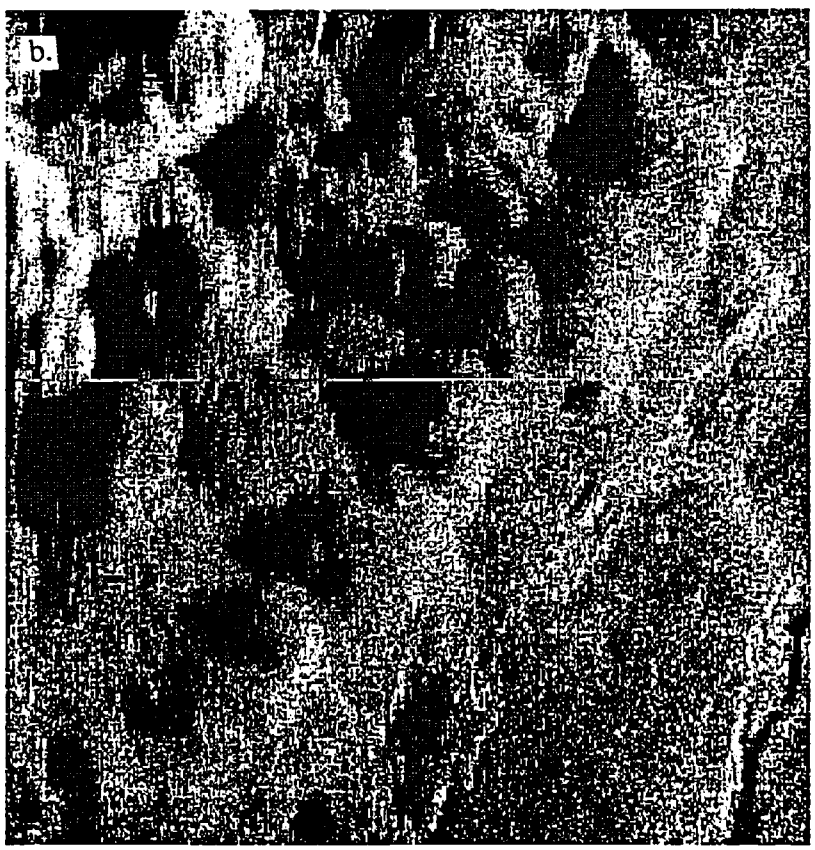

PATH OF SIDESCAN TOWFISH

Figure 11

Figure 12. Sidescan images of negative-relief structures. Insonification is from right to left, and high backscatter is represented by light shades. A) A series of pits on a flat surface. The sides of the pits closest to the sound source are cast in acoustic shadow, and the far sides, which face the sound source, display high backscatter. Note that if the direction of insonification were not known, these features could easily be misinterpreted as positive-relief structures. The bulbous features in the upper left and lower middle areas of the image are volcanic, positive-relief structures. B) Several fissures cutting a low-relief mound. The fissures trend ≈ 020° on the image, and display acoustic shadow on their sides closest to nadir, and high backscatter on their far sides.

<--- INSONIFICATION ---

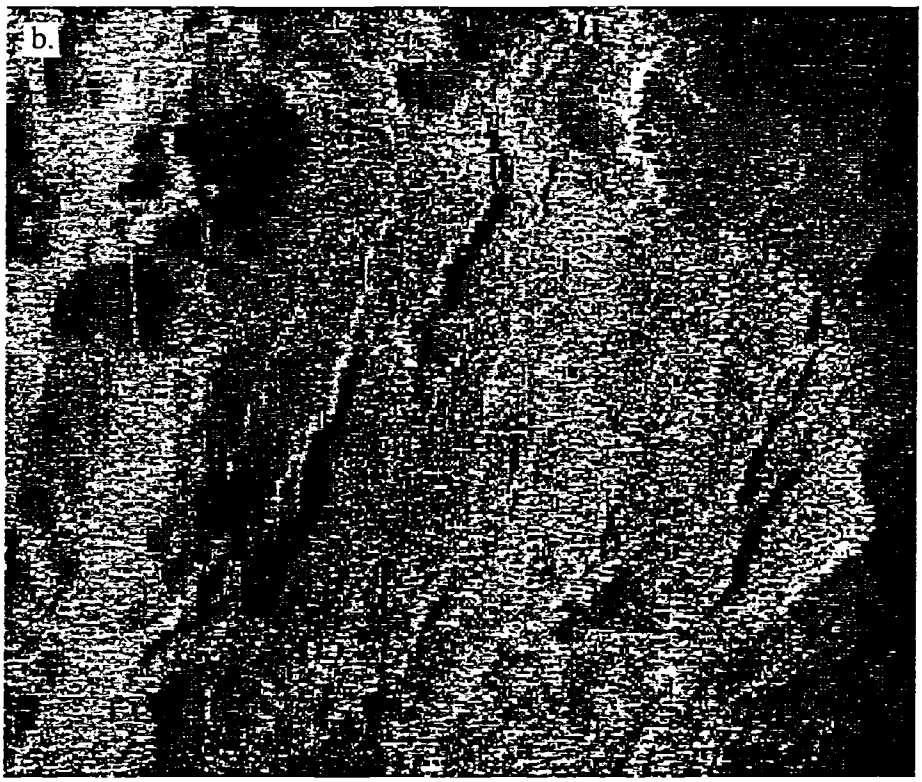

PATH OF SIDESCAN TOWFISH

Figure 12

series of fissures. As can be seen in Figures 11 and 12, positive- and negative-relief structures can appear quite similar, and the sense of relief of a given structure can only be ascertained when the direction of insonification is known.

The insonification direction also affects the appearance of escarpments. Scarps that separate two horizontal (or uniformly dipping) surfaces typically appear in sidescan images as either strong linear reflectors or linear shadow/low-backscatter zones, depending on whether the scarp faces towards or away from the sound source. Since scarps by definition are monoclinal structures, they do not exhibit paired high and low reflectivity zones that are characteristic of ridges or fissures. Scarps which are obliquely crossed by the sound source will display high backscatter on the side of the swath that insonifies the face of the scarp, and low backscatter or an acoustic shadow on the side of the swath that insonifies the scarp from the uphill side (Figure 10). Therefore, the backscatter pattern displayed by a fault will reverse when the fault crosses obliquely beneath nadir, and also when the fault passes obliquely between adjacent swaths on a mosaic (Figure 10). In order to accurately interpret the direction an escarpment is facing, it's always necessary to know the direction from which the scarp is acoustically illuminated.

Interpreting Geologic Structures From Backscatter Patterns

Given these fundamental rules for interpreting morphologies based on backscatter distribution, a wide variety of tectonic and volcanic forms (including tectonic fault scarps, and constructional volcanic cones, ridges and scarps) can be inferred from navigated sidescan imagery. Figure 13 shows a series of fault scarps imaged from their facing side. Fault scarps are recognized by their linear to curvilinear traces, and often crosscut lobate constructional features. The tops and the bases of the fault scarps are well defined, and the scarp faces display uniform high backscatter devoid of internal structure. Figure 14 shows a fault scarp imaged from the upthrown block, looking down over the fault scarp onto the downthrown block below. Once again, the trace of the fault scarp is nearly linear, and the top of the scarp is sharply defined. The slope of the scarp is great enough to prevent the face from being insonified, and an acoustic shadow is cast onto the seafloor below the base of the scarp. Since the face and base of the scarp are not imaged, the constitution of the seafloor there -- for example, the presence or absence of fresh lavas draping the scarp or pooling at the base -- cannot be determined.

Figure 13. Sidescan image of faulted, low-backscatter terrain. Insonification is from top to bottom, and high backscatter is represented by light shades. Several fault scarps are evident, with a major fault extending from the upper left corner of the image to the lower right. The high backscatter intensities recorded over the scarps indicates that they face towards nadir; the seafloor to the right of the scarps is downthrown relative to the seafloor to the left. These scarps display the characteristics that were used as criteria for identifying fault scarps throughout the survey: linear to curvilinear scarp traces; distinct, well-defined backscatter boundaries at their bases and tops; and generally homogenous high backscatter over their faces (contrast these characteristics with those of constructional volcanic scarps shown in Figure 15). The low-backscatter surfaces that are crosscut by the faults are considered to be indicative of sedimented terrain. The area of homogeneous low backscatter in the upper right is interpreted to a flat, sediment covered surface. The area in the lower left contains numerous positive-relief structures separated by low-backscatter seafloor, and is interpreted to be a field of constructional volcanic features that have been partially buried beneath a veneer of sediment, with the tops of the volcanic structures poking out of sediments that have accummulated on the topographic lows between them.

PATH OF SIDESCAN TOWFISH

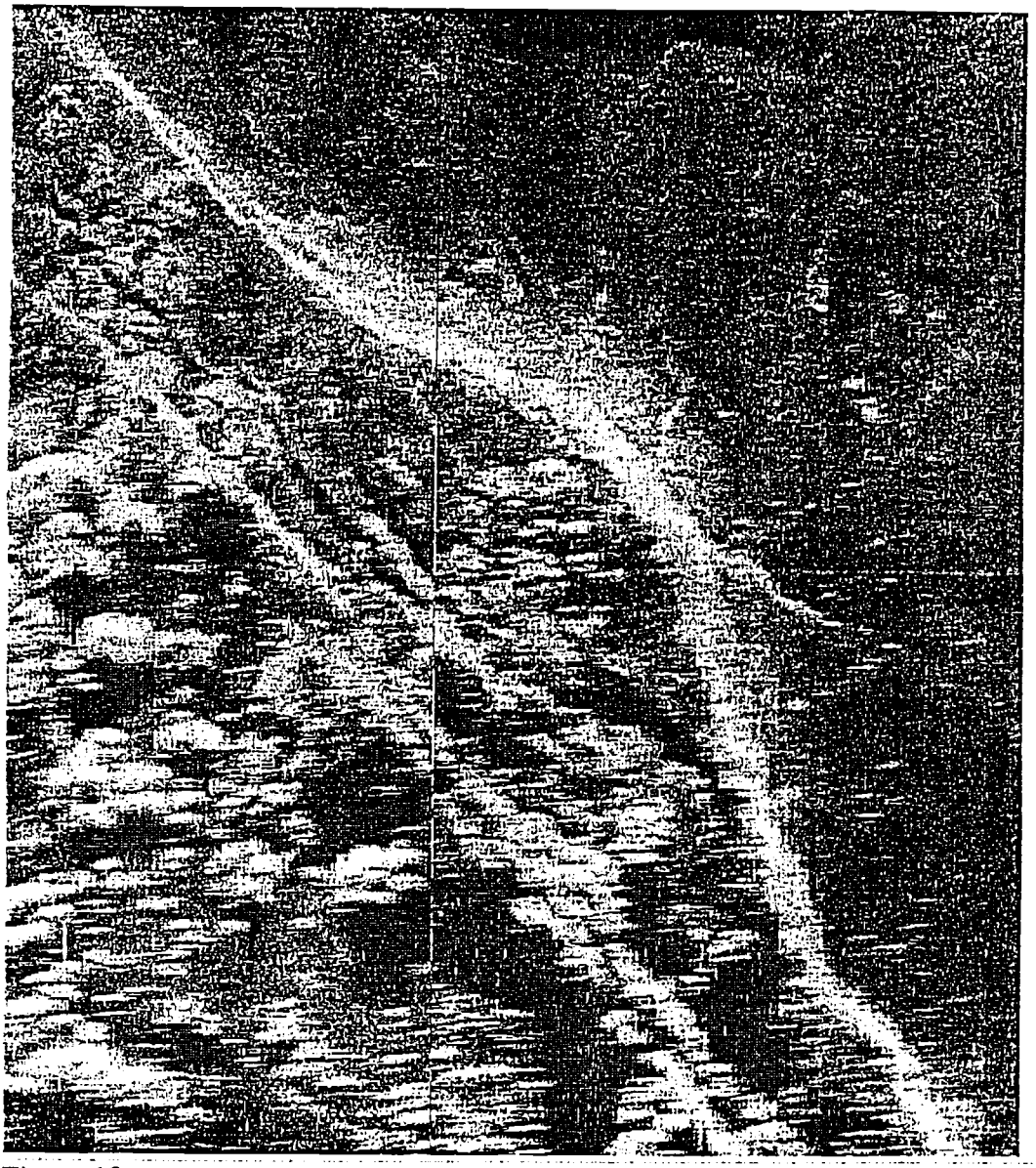

<--- INSONIFICATION ---

Figure 13

Figure 14. Sidescan image of low-backscatter terrain crosscut by a fault that faces away from nadir. Insonification is from right to left, and high backscatter is represented by light shades. A major fault scarp trends from the upper right corner of the image to the lower left. This scarp exhibits backscatter characteristics common to fault scarps that face away from the sound source: a fault trace that varies from linear to curvilinear; a sharp backscatter boundary along the top of the scarp that marks the break in slope; and low or no backscatter over the face of the scarp. The seafloor to the right of the fault is upthrown relative to the seafloor on the left. The surface of the seafloor to the right displays a mottled backscatter pattern composed of blotches of low- and intermediate-intensity backscatter; this pattern is considered to be indicative of slightly hummocky, sedimented seafloor. A pair of fault scarps are evident in the upper left corner of the image that face towards nadir, and several smaller faults, many of indeterminate throw, are oriented parallel to the trend of the major fault.

<--- INSONIFICATION ---

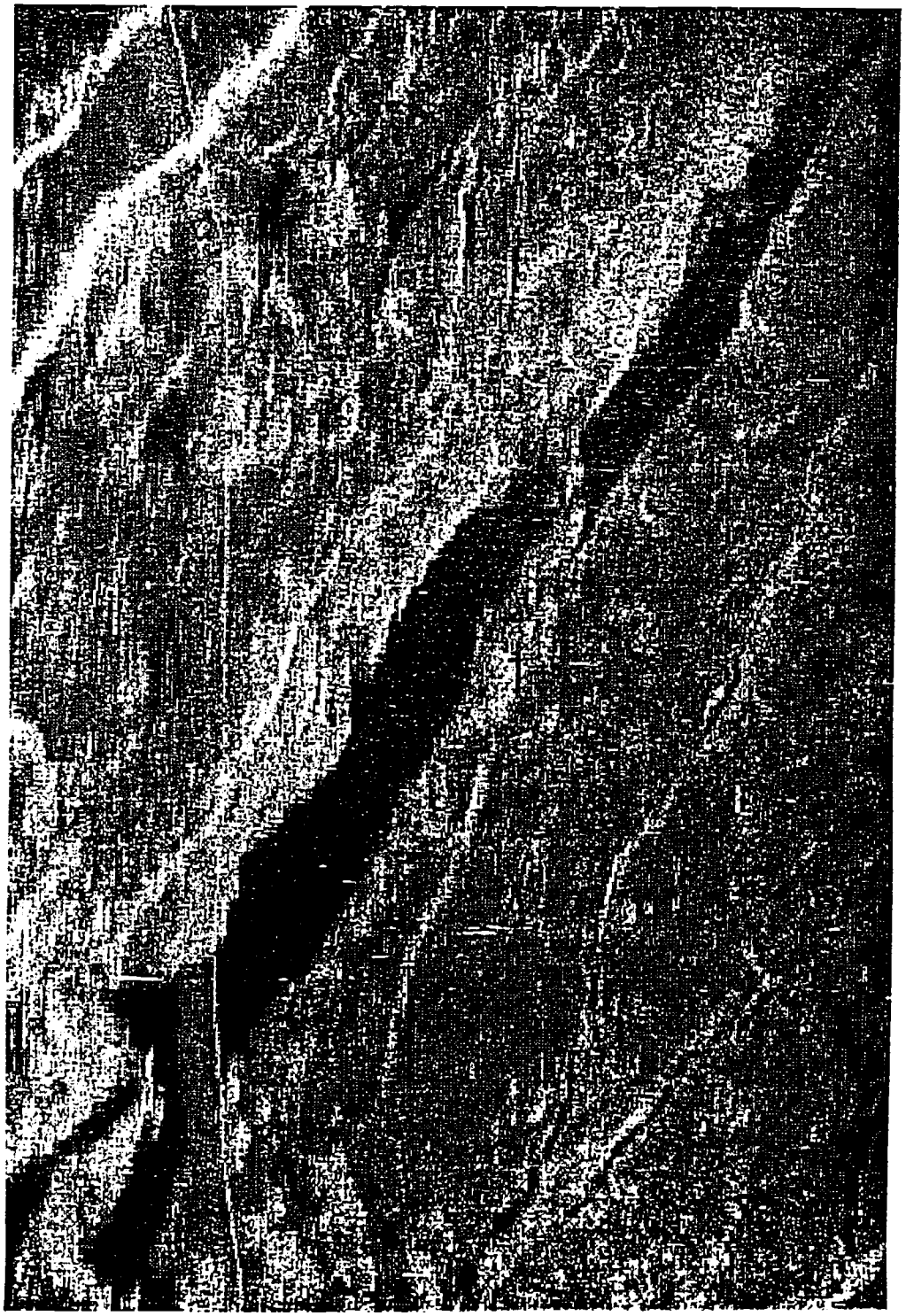

PATH OF SIDESCAN TOWFISH

Figure 14

Sidescan imagery is an effective tool for discriminating tectonic scarps from constructional volcanic scarps. Generally, volcanic scarps (including flow fronts, the flanks of constructional ridges and cones, and flows that mantle older tectonic scarps) do not exhibit the sharp, well-defined tops and bases or very high, homogeneous backscatter on the scarp face that are characteristic of fault scarps. Lobate or scalloped structures are often visible on the face and near the base of volcanic escarpments. The difference between backscatter patterns displayed by tectonic and volcanic scarps is shown in Figure 15. The insonification direction here is from right to left, and the face of a ≈ 100 m scarp is illuminated. An along-strike change in vertical relief and slope across the scarp is evident in the SeaBeam bathymetry over this area (shown in Figure 20, near 45°32.5'N/129°59.4'W); however, the bathymetry alone cannot discriminate the nature (volcanic versus tectonic) of the scarp . The sidescan imagery reveals that the scarp is constructed from several faults (evident in the upper right and lower left corners), and that the scarp in the central part of the image is buried beneath lavas. Although most of the vertical relief over the middle part of the scarp is probably due to tectonic rather than volcanic processes (the lavas here flowed over the preexisting tectonic scarp), the general morphology of the scarp is representative of other volcanic scarps within the survey area.

In areas where large scale topographic features do not contribute to the observed backscatter distribution, the intensity of the echo is controlled by the small scale roughness of the region, and by the acoustic impedance contrast between the water and seabed. An example of an area that displays several different backscatter patterns due to variations in these factors is shown in Figure 16. With the exception of the two major fault scarps in the lower left corner, the seafloor in this area is relatively flat, and topographic influence on the backscatter pattern is minimal. Three different terrains, each exhibiting a different backscatter intensity, are evident here: a bright, high-backscatter field that occupies the center of the image; a dark, low-backscatter area in the bottom left, located on the upthrown side of the inner fault scarp; and regions of intermediate-backscatter above and below the high-backscatter field. On the bottom part of the image, the contact between the high- and intermediate-backscatter areas does not display topographic relief, and there is no evidence to suggest the presence of a scarp between the two backscatter fields. Several small faults in the upper part of the image abruptly terminate against the edge of the high-backscatter field, which is not itself cut by any of these faults. High-backscatter "fingers" extend into grabens and along small faults on the top part of the

Figure 15. Sidescan sonar image of lavas overlying a fault scarp, illustrating the different backscatter patterns displayed by tectonic and volcanic scarps. Insonification is from right to left, and high backscatter is represented by light shades. A series of discrete faults compose a scarp that extends diagonally across the image from upper right to lower left. The high-backscatter recorded along the faces of the faults indicates that they face towards nadir; therefore the seafloor to the left of the fault is upthrown relative to the seafloor on the right. Intermediate-backscatter lavas are evident in the upper left corner of the image. These lavas overlie a low-backscatter patch of seafloor above the fault scarps in the uper right corner, and bury the fault scarps in the center of the figure. A negative-relief structure is apparent within the intermediate-backscatter lavas above the point where the lavas overlie the fault scarps. The area of the scarp covered by lavas displays nearly constant backscatter intensities over the upper part of the scarp, and the base of the scarp is marked by lobate features that are defined by bands of higher backscatter. Several high-backscatter stripes, oriented roughly transverse to the trend of the scarp, appear on the face of the lava-covered part of the scarp. A lobate feature extends from the base of the scarp towards the lower right corner of the image, which has been cut by a small fault.

<--- INSONIFICATION ---

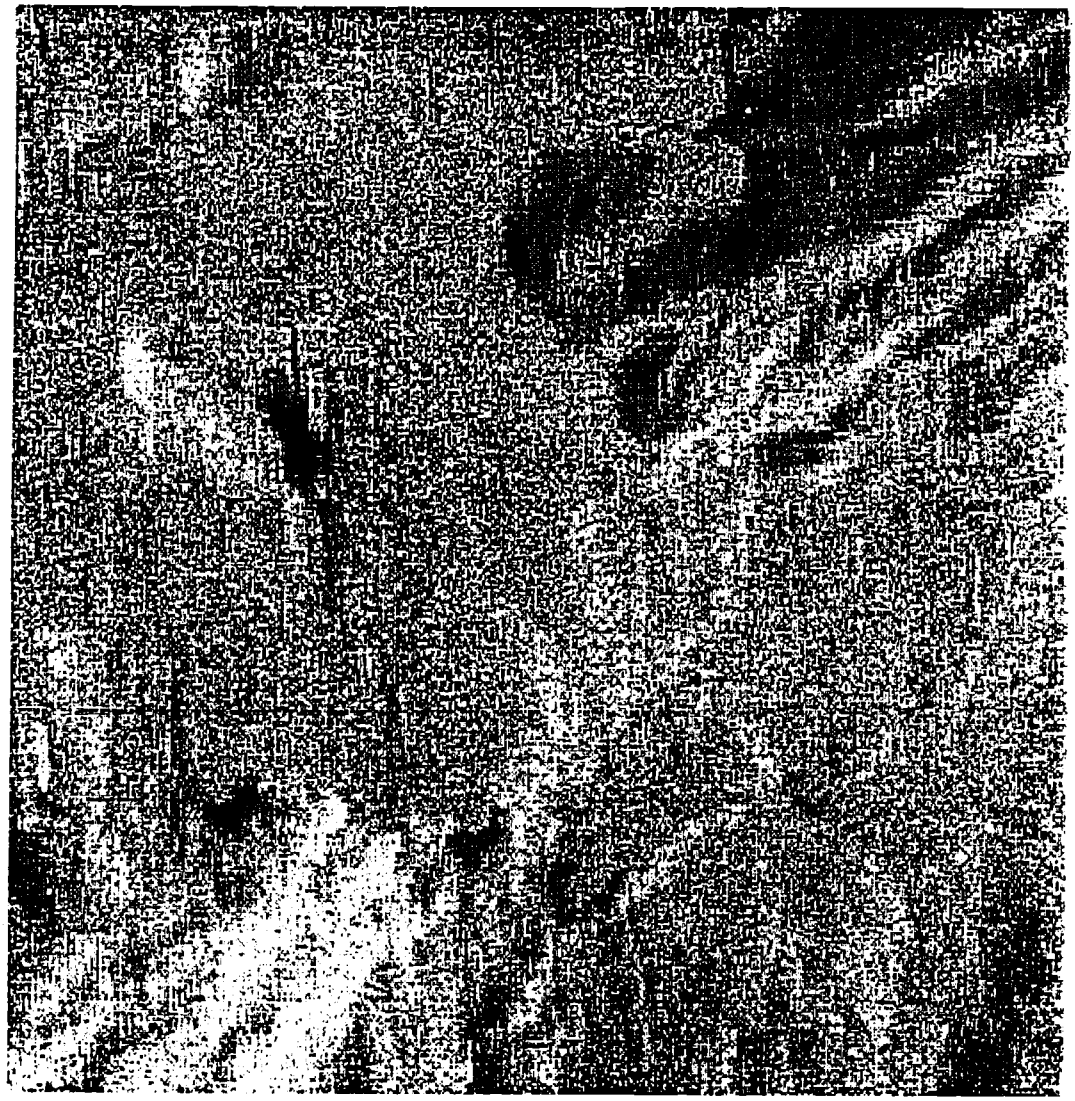

PATH OF SIDESCAN TOWFISH

Figure 15

Figure 16. Sidescan sonar image showing three distinct backscatter-intensity zones over a planar, faulted seafloor. Insonification is from bottom to top, and high backscatter is represented by light shades. Two major fault scarps, facing nadir, trend diagonally across the left side of the image. A region of high backscatter in the central part of the image, located to the right of the fault scarp, is bounded on the top and bottom by patches of intermediate-backscatter seafloor. The seafloor on the upthrown side of the inner fault displays low backscatter. Since each of these surfaces is flat, topographic effects do not contribute to the observed backscatter patterns, and therefore the difference in backscatter intensity between each region is due to variations in the small-scale roughness or reflection coefficient between each surface. Regional structural relationships indicate that the surface in the lower left corner is the oldest, and the high-backscatter surface is the youngest. A sequence of events is inferred for this area, involving: 1) emplacement of the **A** lavas; 2) displacement along fault **B**, elevating the **A** lavas above the area within the axial valley subject to volcanic flooding; 3) emplacement of the **C** lavas, followed by a period of sedimentation; and 4) deposition of the **D** lavas over the **C** lavas. The dark region in the upper right corner is an artifact caused by the proximity of this area to nadir. Nadir is just below the bottom of the image.

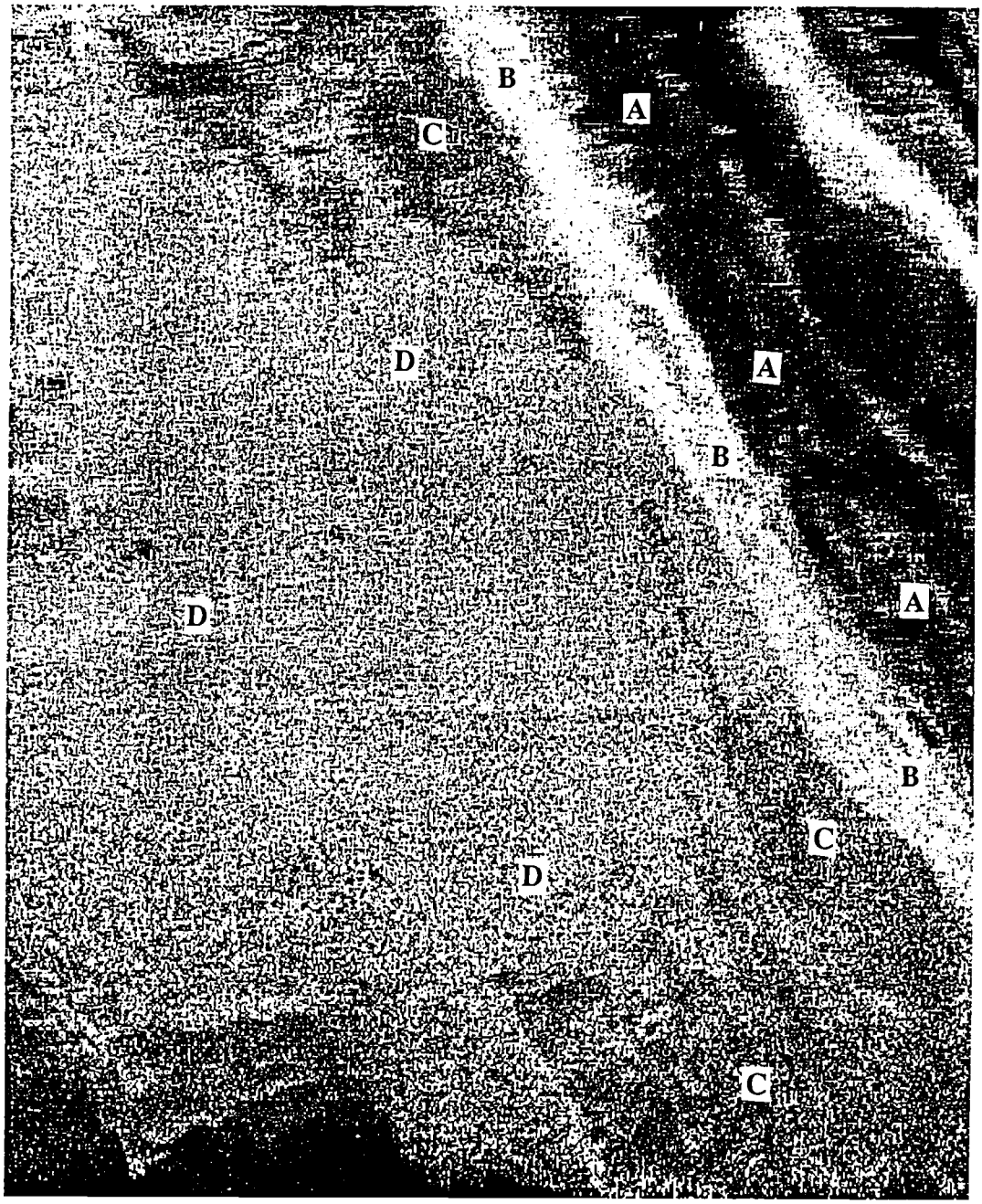

Figure 16 PATH OF SIDESCAN TOWFISH

high-backscatter region, suggesting that the faults predate the field of high-backscatter material.

The geological significance of the broad backscatter patterns displayed over each of the three surfaces in Figure 16 is difficult to assess with certainty; however, previous studies have documented a general relationship between backscatter intensity and the presence of sediment. Results from McKinney and Anderson (1963) and Flemming (1976) suggest that the presence of sediment over a surface results in low acoustic backscatter values. Bare lavas typically display high backscatter relative to sedimented surfaces (e.g., Kappel and Normark, 1987; Barone and Ryan, 1988), although the amount of acoustic energy backscattered from bare lavas is a function of the surficial flow morphology, and bare lavas conceivably could display either low or high backscatter. For example, small areas of low backscatter within the caldera of Axial volcano have been shown to be lightly sedimented flat sheet flows (R. W. Embley, personal communication, 1988). Low backscatter values measured from bare, flat-lying lavas probably result from the forward specular reflection of acoustic energy away from the sound source (Leenhardt, 1974).

The backscatter patterns evident in Figure 16 may be interpreted in two different ways. First, the backscatter variation may strictly be due to the surficial flow morphology of the lavas. In this case, the bright areas may represent rough, rugged lavas (such as jumbled sheet flow, for example) that scatter a high proportion of the incident acoustic energy back towards the sound source; the darker areas may indicate smoother flow forms that reflect sound away from the sound source in a mirror-like fashion. An alternate interpretation is that the backscatter differences between the three terrains represent different degrees of sediment cover over each surface, with the high-backscatter area being the least sedimented. Structural relationships in this area indicate that the low backscatter surface is probably the oldest, and the high backscatter surface is the youngest, suggesting that, in this case, the latter interpretation may be correct.

Backscatter patterns alone are probably not capable of accurately and consistantly discriminating between individual flows within a lava field, since the surface roughness of individual flows may change drastically along the length of the flow (as demonstrated for subaerial flows by Holcomb, 1980, and by Guest et al., 1987), and the physical boundary of a lava flow may not necessarily correspond to a surface roughness boundary between flows. For the purposes of this study, high backscatter intensities over flat areas are generally considered to indicate a relative

lack of sediment over a volcanic surface, and individual flows were not mapped. Low backscatter intensities over flat regions are inferred to indicate the presence of either sediment, or flat-lying unsedimented lavas.

RESULTS

The final navigated mosaic of the SeaMARC I data collected within the south Axial survey area is shown on Plate 1 (located inside the pocket on the final page). For reference, the outline of the survey area is superimposed on the regional bathymetry in Figures 2 and 17. The image is presented in reverse black-and-white, such that areas of low backscatter and acoustic shadow appear dark, and high-backscatter areas are light. Several separate provinces may be identified within the survey area, each exhibiting distinct morphological characteristics: the northern tip of the Vance segment, which enters the survey area from the south at 45°24'N, 130° 02'W, displays generally high backscatter and is surrounded by darker terrain on its eastern and southwestern sides; the seafloor of the Juan de Fuca plate east of the Vance segment, which exhibits low general backscatter and includes two small circular volcanoes and ridge-parallel tectonic fabric; the south Axial volcano rift zone (SARZ), which is characterized by highly reflective, linear volcanic ridges near the volcano's summit, and rugged, irregular terrain around its distal southern end; and South Helium Basin, a semi-rectangular embayment in the southeast flank of Axial volcano located east of the SARZ. The detailed morphologies of each of these areas are discussed in the following sections.

The Vance Segment

The axis of the Vance Segment enters the survey area from the south at 45°24'N, 130°02'W, and exhibits many of the general characteristics observed along the ridge crest farther south (discussed by Kappel and Ryan, 1986; and Embley et al., 1983). The axial valley here is 5.5 km wide and bounded on either side by steep, linear walls up to 200 m high (Figure 2). Beyond the valley walls, two pairs of N20°E-trending ridges symmetrically flank the axial valley. The crests of the inner pair of ridges (the east marginal ridge and west marginal ridge -- referred to herein as the EMR and WMR) shoal to 2275 m (east) and 2225 m (west). Each is located approximately 3.5 km from the geometric center of the valley. The crests of the outer ridges each lie roughly 7.1 km from the valley's axis, and are slightly deeper (2300 m) than the marginal ridges.

In general, the seafloor beyond the valley walls displays low backscatter relative to the floor of the axial valley. The seafloor outside the axial valley locally displays a distinctive mottled backscatter pattern, characterized by bulbous

constructional features surrounded by flat, low backscatter material. Previous sidescan surveys of the JDF ridge (e.g. Kappel and Normark, 1987; Barone and Ryan, 1988) have revealed similar backscatter patterns outside of the axial valleys of the Cleft and Endeavour segments, and photographic ground-truthing of these areas indicates that these areas are typically composed of mounds of sediment-covered pillow lavas. Photographs of the high-backscatter axial valleys of the Cleft and Endeavour segments reveals that the lavas in these regions are covered by less sediment thatn outside the valley walls (Kappel and Normark, 1987; Barone and Ryan, 1988). By analogy, the regional low backscatter displayed by the seafloor surrounding the northern tip of the Vance segment is inferred to indicate thicker sediments there than within the high-backscatter axial valley.

The backscatter characteristics of the seafloor in and around the Vance segment are shown in more detail in Figures 18 through 22. For reference, the positions of each of these images are superimposed on the bathymetry of the area in Figure 17; each figure encompasses an area covering 3' in latitude and 6.5' in longitude, beginning at the southern end of the survey area with Figure 18 and progressing northwards along the rift zone to Figure 22. Included with each sidescan image is an interpretation of the tectonic and volcanic features revealed by the imagery, and a detailed SeaBeam contour plot of the bathymetry of the area shown.

--- *The Vance Segment From 45°26'N to 45°32'N*

Between 45°26'N and 45°32'N the axial valley of the Vance segment contains three general structural elements: 1) steep valley walls constructed from longitudinally discontinuous normal faults that are commonly offset from one another in plan view by as much as 500 m; 2) A linear volcanic ridge, oriented parallel to the strike of the axial valley (N20°E), that sits slightly east of the valley's geometric center and displays up to 60 m of vertical relief; and 3) a 1 km-wide, N20°E-trending graben located immediately west of the central ridge, defined by inward-facing faults that accommodate as much as 40 m of vertical relief from the valley floor down to the base of the graben.

Both sides of the valley are bounded by major fault scarps. On the west side of the valley, near 45°27'N/130°02.5'W, two inward-facing fault scarps step up to a fault-bounded ridge that shoals to 2350 m, and two additional inward-facing scarps occur west of the ridge (Figure 19). At the northern edge of Figure 18, near

Figure 17. Location map for the detailed sidescan mosaics and SeaBeam bathymetry presented in Figures 18 through 29. The region encompassed by each detailed figure is outlined. Numbers correspond to the figure numbers of the detailed plots.

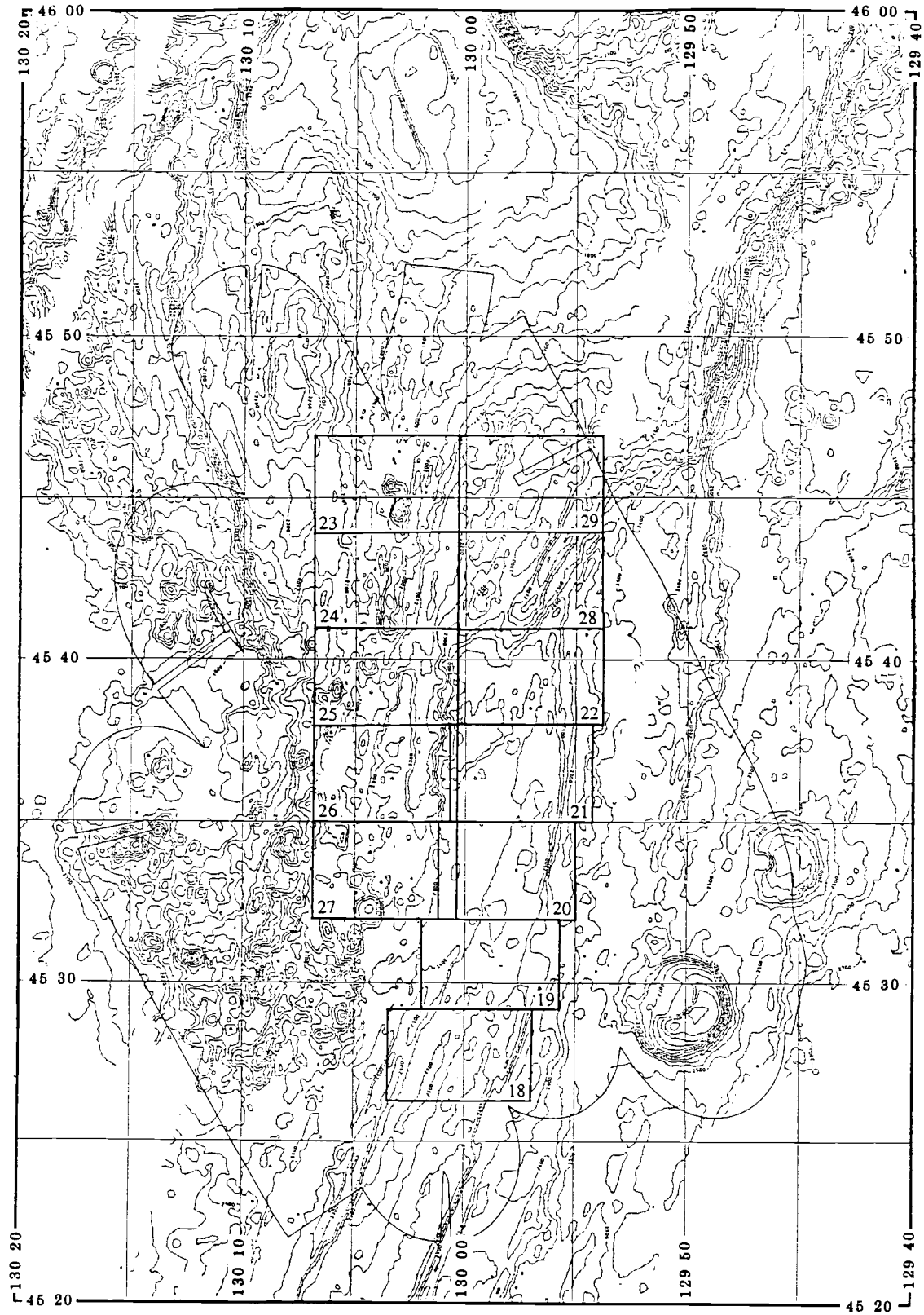
46 00
45 50
45 40
45 30
45 20
130 20
130 10
130 00
129 50
129 40
23
29
24
28
25
22
26
21
27
20
19
18

Figure 17

Figure 18. Sidescan sonar mosaic, geological interpretation, and detailed bathymetry of the axial valley of the Vance segment. See Figure 17 for location of this subplot. The figures are constructed so that the pages may be flipped back and forth to compare the sidescan imagery, bathymetry and interpretation. A) Sidescan mosaic. High backscatter is represented by light shades, and the path of the towfish is marked by white bands. The boundaries between adjacent swaths are evident between the towfish tracklines; insonification direction depends on which swath covers a given area. B) Interpretation of sidescan imagery. Major faults are depicted by heavy lines, minor faults by fine lines, with hatchures on the downthrown block. Small-offset faults of indeterminate throw are not hatchured. Faults are dotted where they are covered by lavas. Constructional volcanic features are marked by fine scalloped lines, and contacts are dashed where inferred (usually because they are lost in acoustic shadow). Labelled features are discussed in detail in the text. The fault scarps mapped in the southeast corner are offset from the structures shown in the SeaBeam bathymetry due to an error in towfish navigation. C) SeaBeam bathymetry contoured at 10 m intervals. Relevant features discussed in the text are marked.

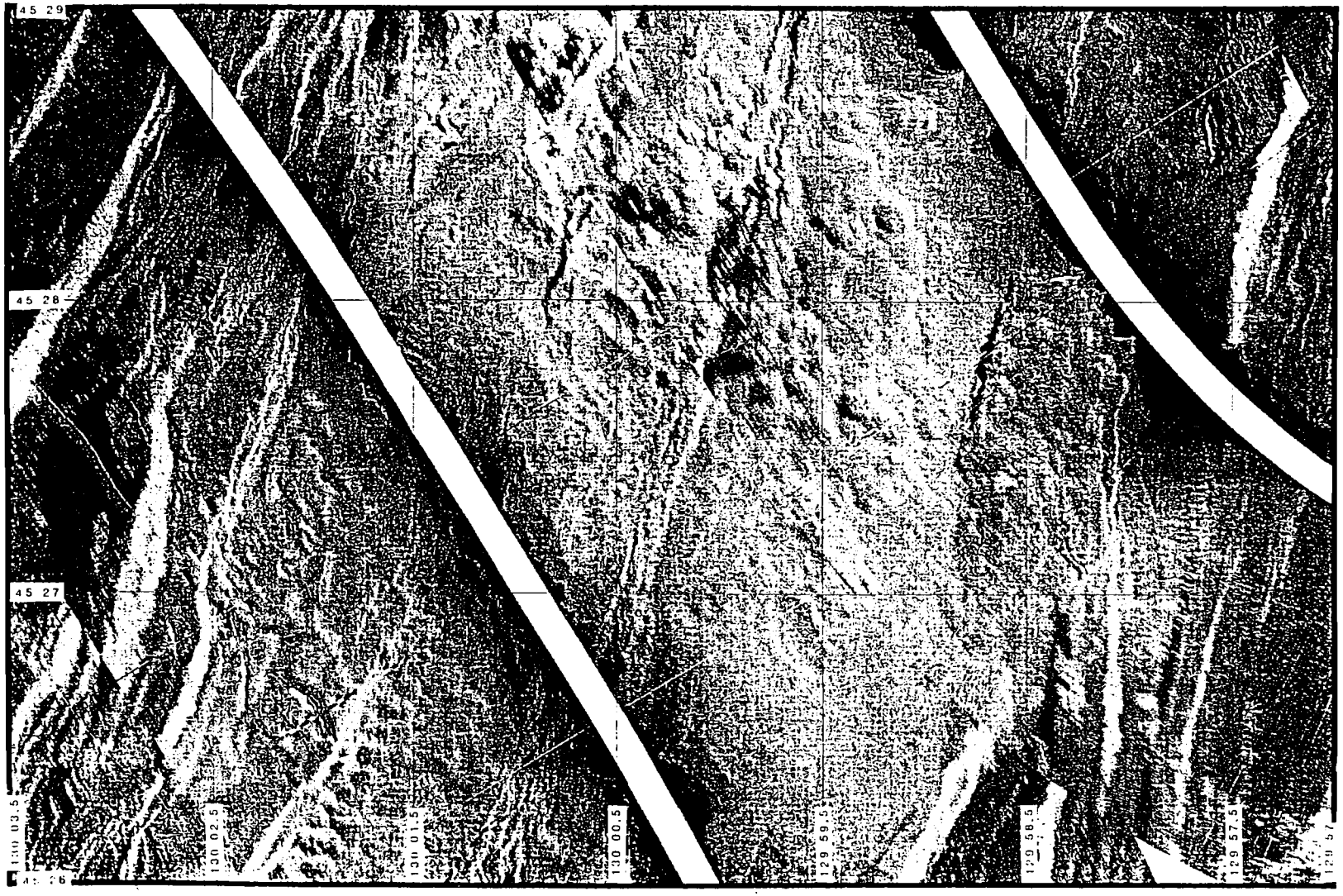

Figure 18 a.

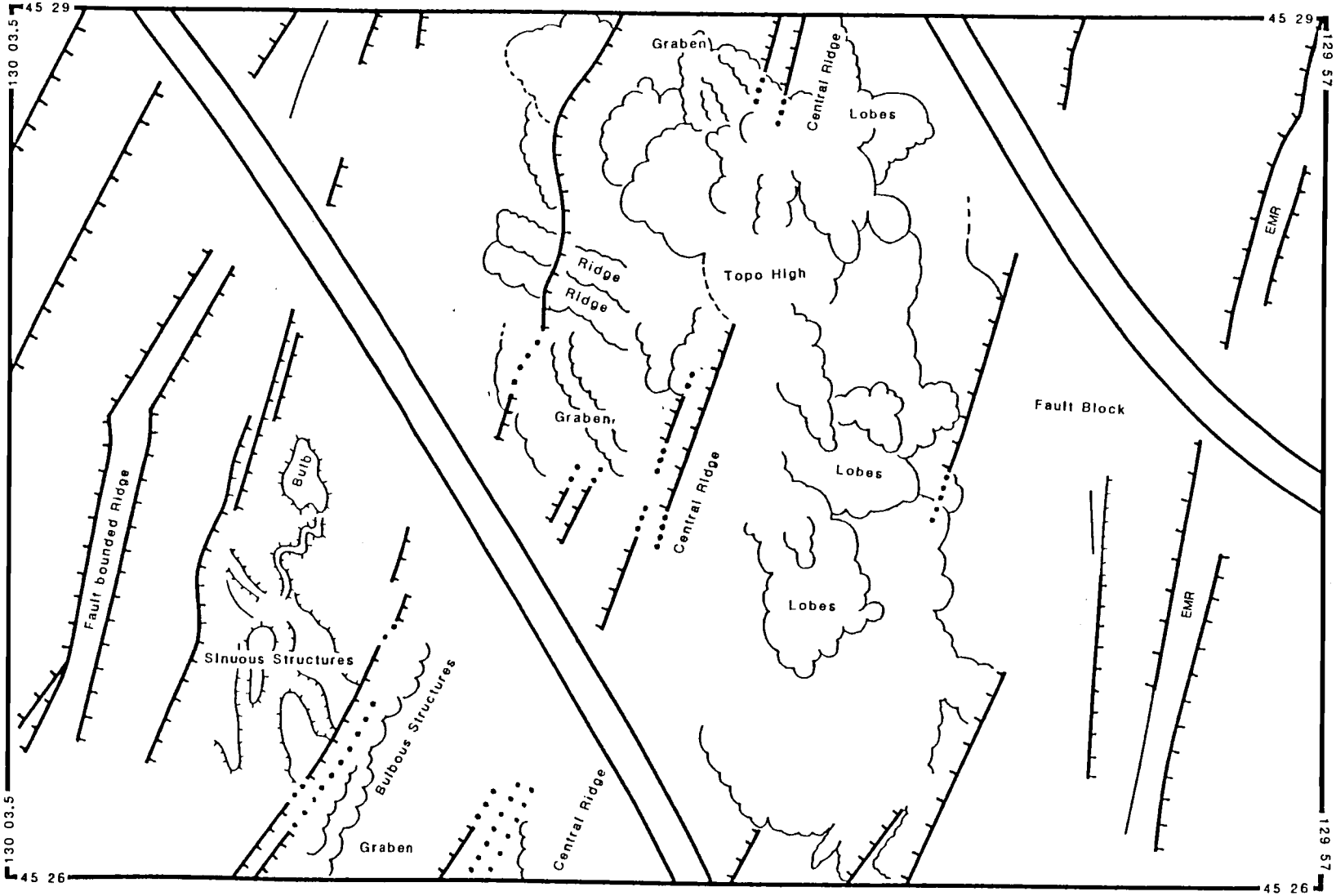
45 29
130 03.5
129 57
45 26
Graben
Central Ridge
Lobes
Ridge
Ridge
Topo High
Graben
Central Ridge
Lobes
Lobes
Fault Block
EMR
EMR
Fault bounded Ridge
Bulb
Sinuous Structures
Bulbous Structures
Graben
Central Ridge

Figure 18 b.


45 29
130 03.5
129 57
45 26
WMR
Graben
Lobe
Lobe
Lobe
Central Ridge
Spur
Graben
LMR
LMR

Figure 18 c.

Figure 19. Imagery of the Vance segment's axial valley, see Figure 17 for location. A) Sidescan mosaic, high backscatter is represented by light shades. B) Geological interpretation. Symbolism is consistent with that in Figure 18. Arrows show inferred flow direction of lavas based on the surface morphology as revealed by the sidescan imagery, and on the local bathymetry. C) SeaBeam bathymetry, 10 m contour interval.

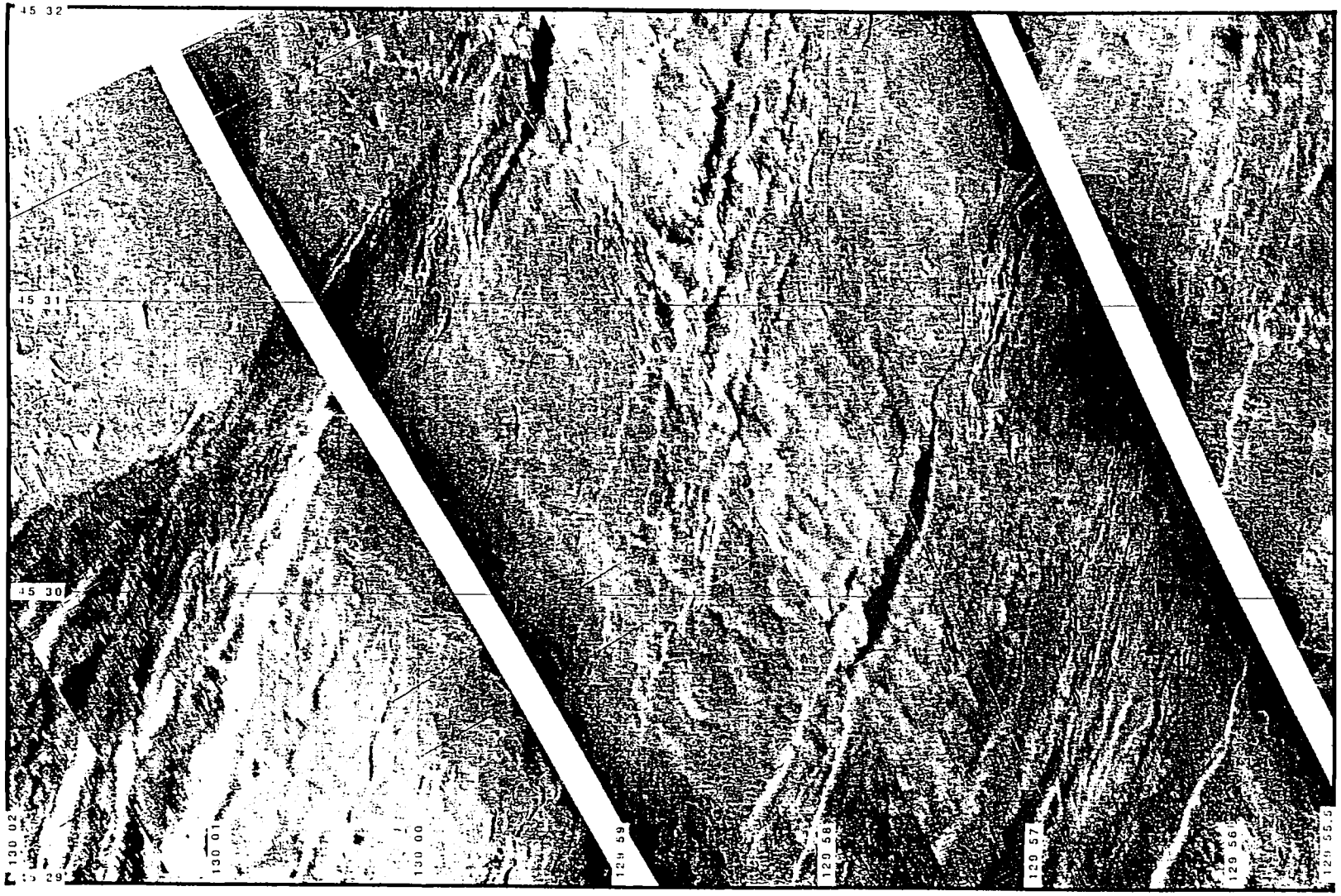

Figure 19 a.

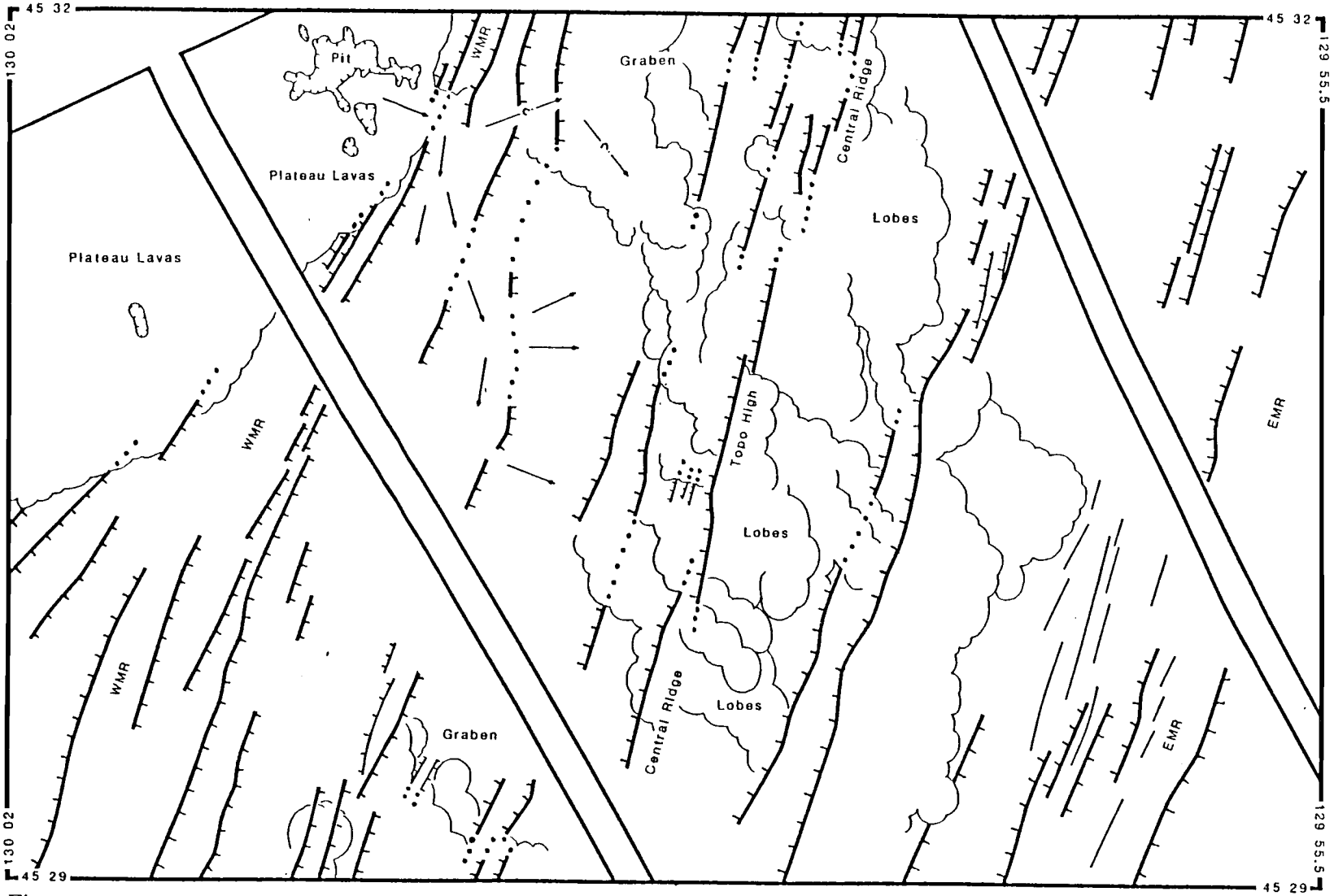
45 32
130 02
129 55.5
45 29
Pit
WMR
Graben
Central Ridge
Plateau Lavas
Lobes
Todd High
EMR
Central Ridge

Figure 19 b.

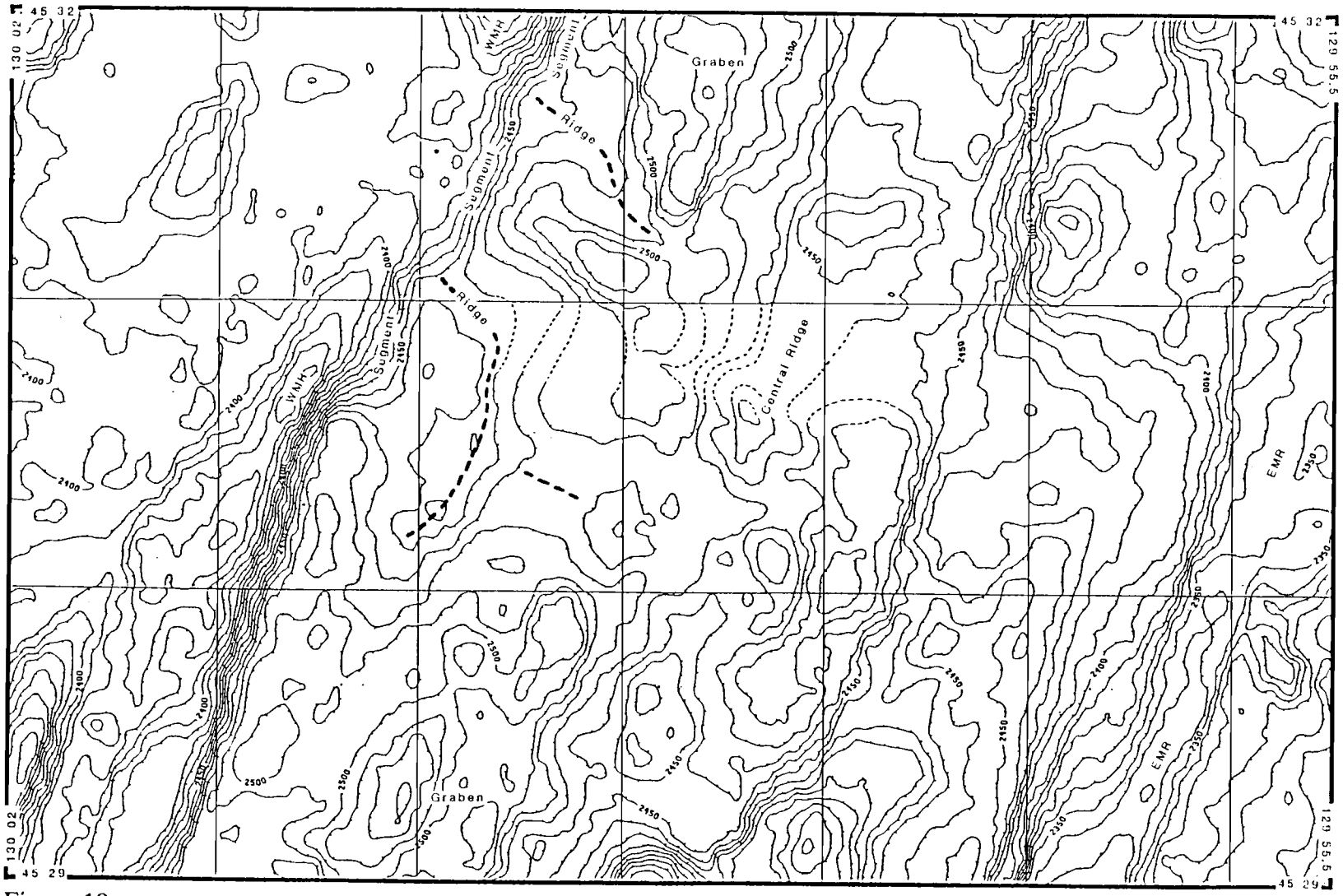
45 32
130 02
129 55.5
45 29
WMH
Segment
Ridge
Graben
Central Ridge
EMR
2400
2450
2500
2550

Figure 19 c.

Figure 20. Imagery of the Vance segment's axial valley, see Figure 17 for location. A) Sidescan mosaic, high backscatter is represented by light shades. B) Geological interpretation. Symbolism is consistent with that in Figure 19. C) SeaBeam bathymetry, 10 m contour interval.

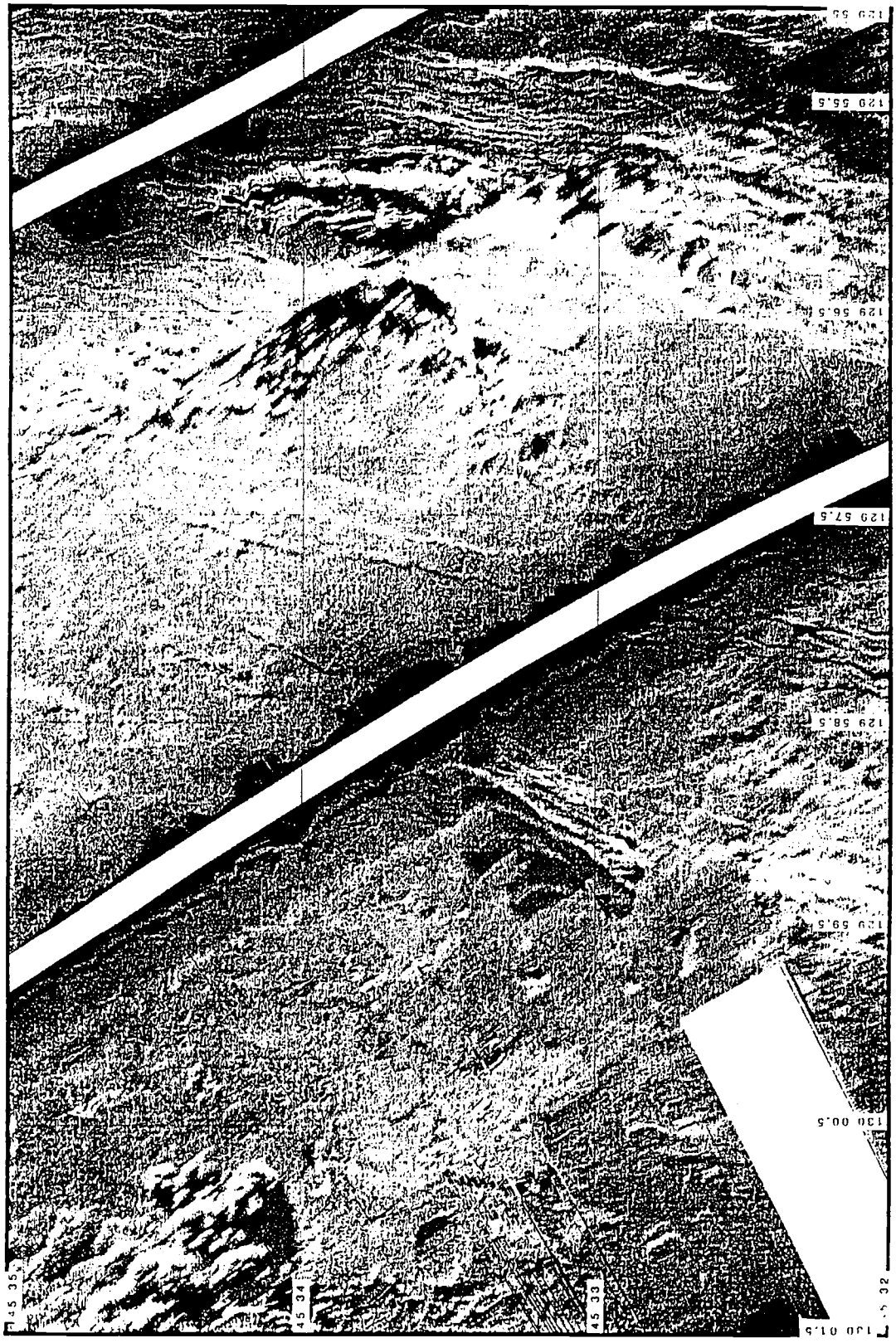
129 55
129 55.5
129 56.5
129 57.5
129 58.5
129 59.5
130 00.5
130 01.5
45 35
45 34
45 33
45 32

Figure 20 a.

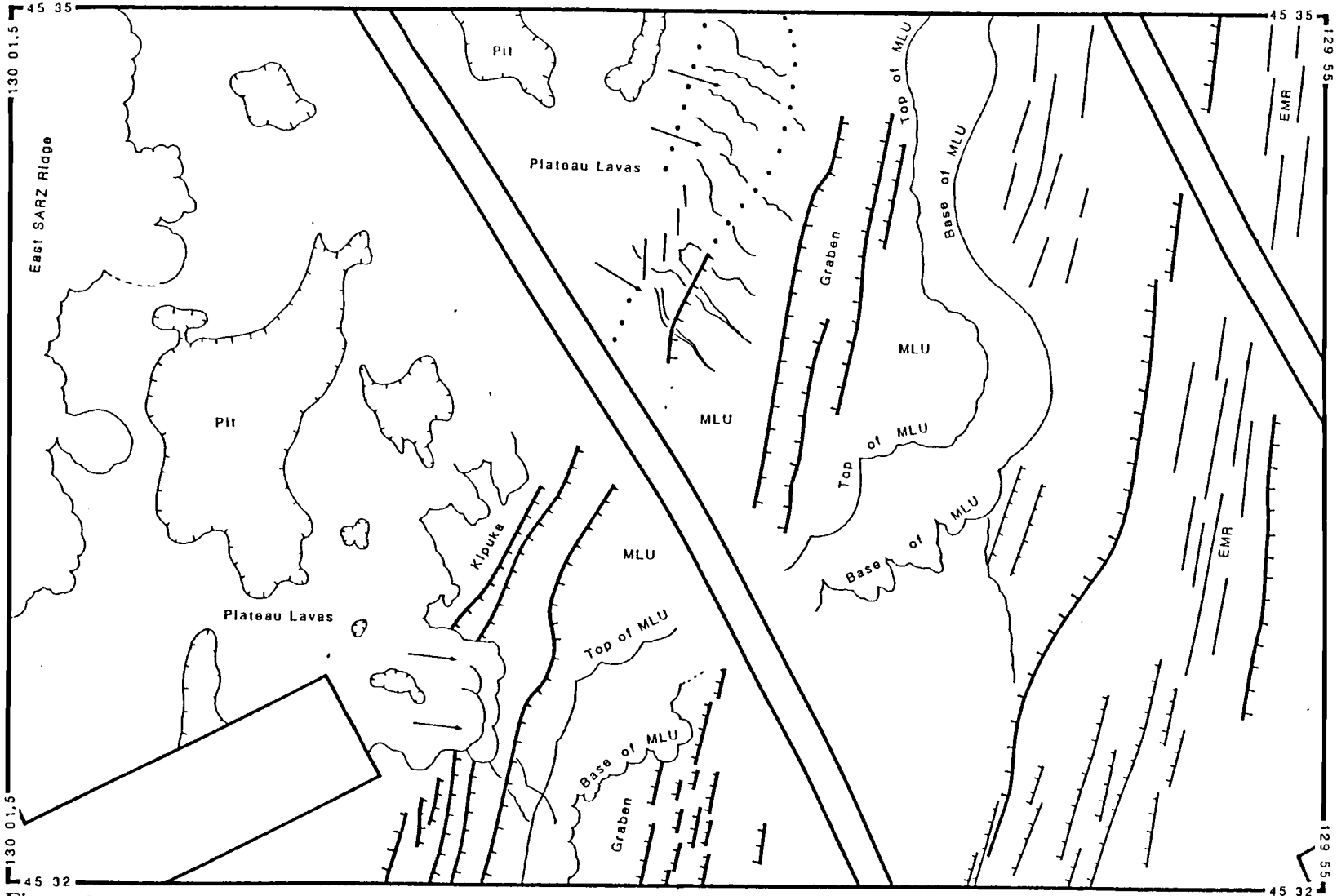
45 35
130 01.5
East SARZ Ridge
Pit
Plateau Lavas
Pit
Plateau Lavas
MLU
Top of MLU
Base of MLU
Graben
Kipuka
MLU
Top of MLU
Base of MLU
Graben
MLU
Top of MLU
Base of MLU
EMR
EMR
45 35
129 55
130 01.5
45 32
45 32
129 55
Figure 20 b.

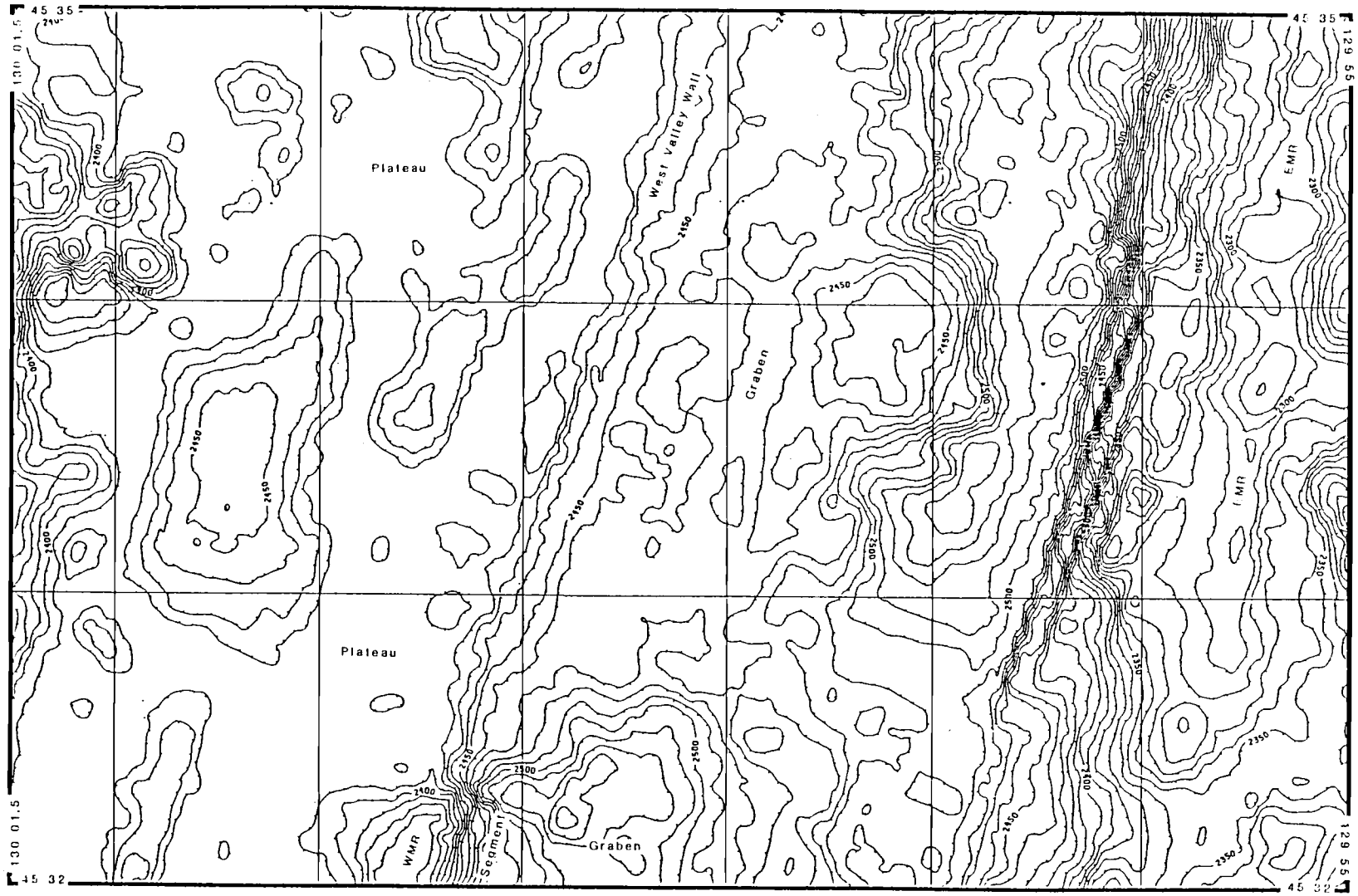
45 35
130 01.5
129 55
Plateau
West Valley Wall
Graben
EMR
IMR
WMR
Segment
45 32

Figure 20 c.

Figure 21. Imagery of the Vance segment's axial valley, see Figure 17 for location. A) Sidescan mosaic, high backscatter is represented by light shades. B) Geological interpretation. Symbolism is consistent with that in Figure 19. C) SeaBeam bathymetry, 10 m contour interval.

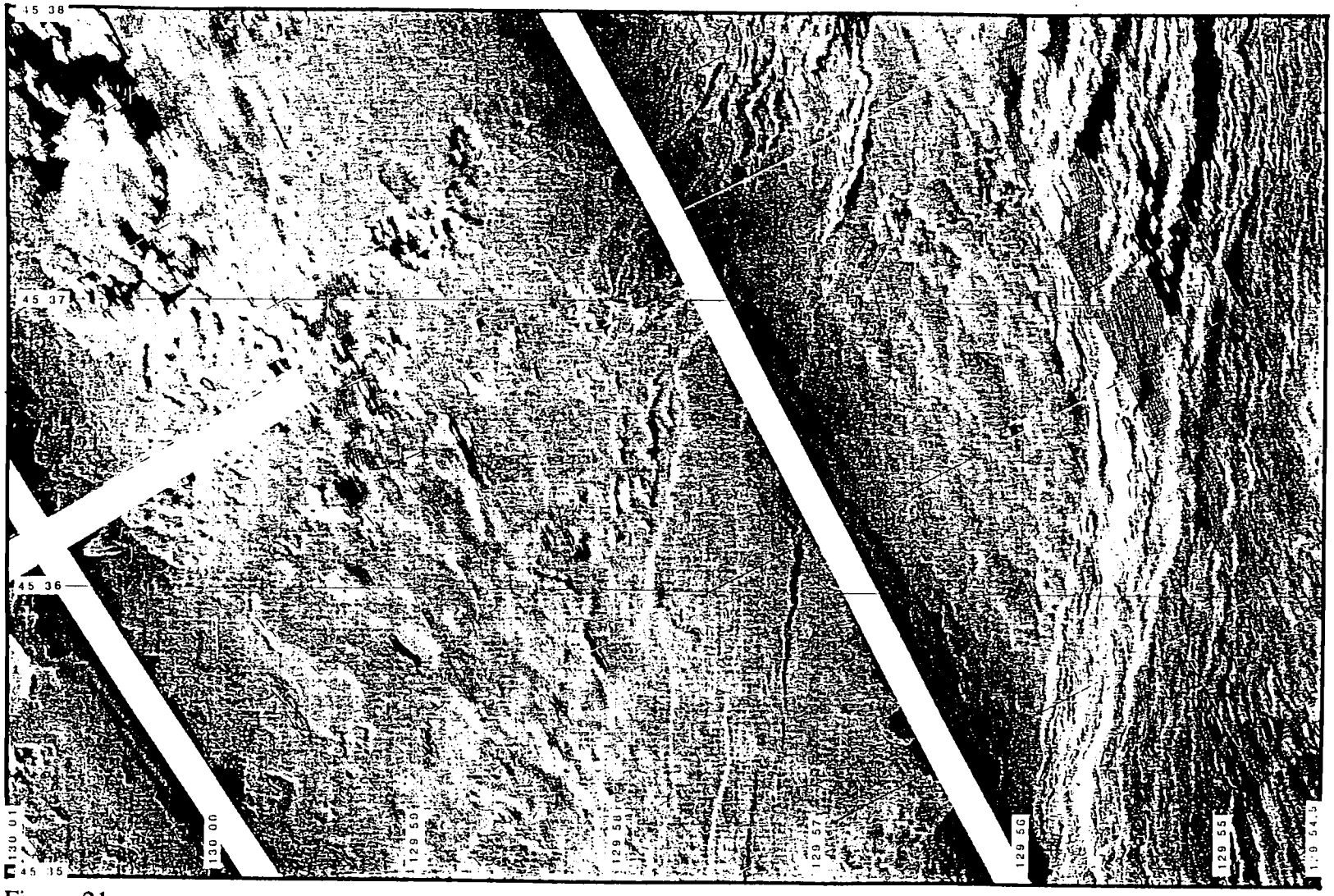
45 38
45 37
45 36
45 35
130 01
130 00
129 59
129 58
129 57
129 56
129 55
129 54.9

Figure 21 a.

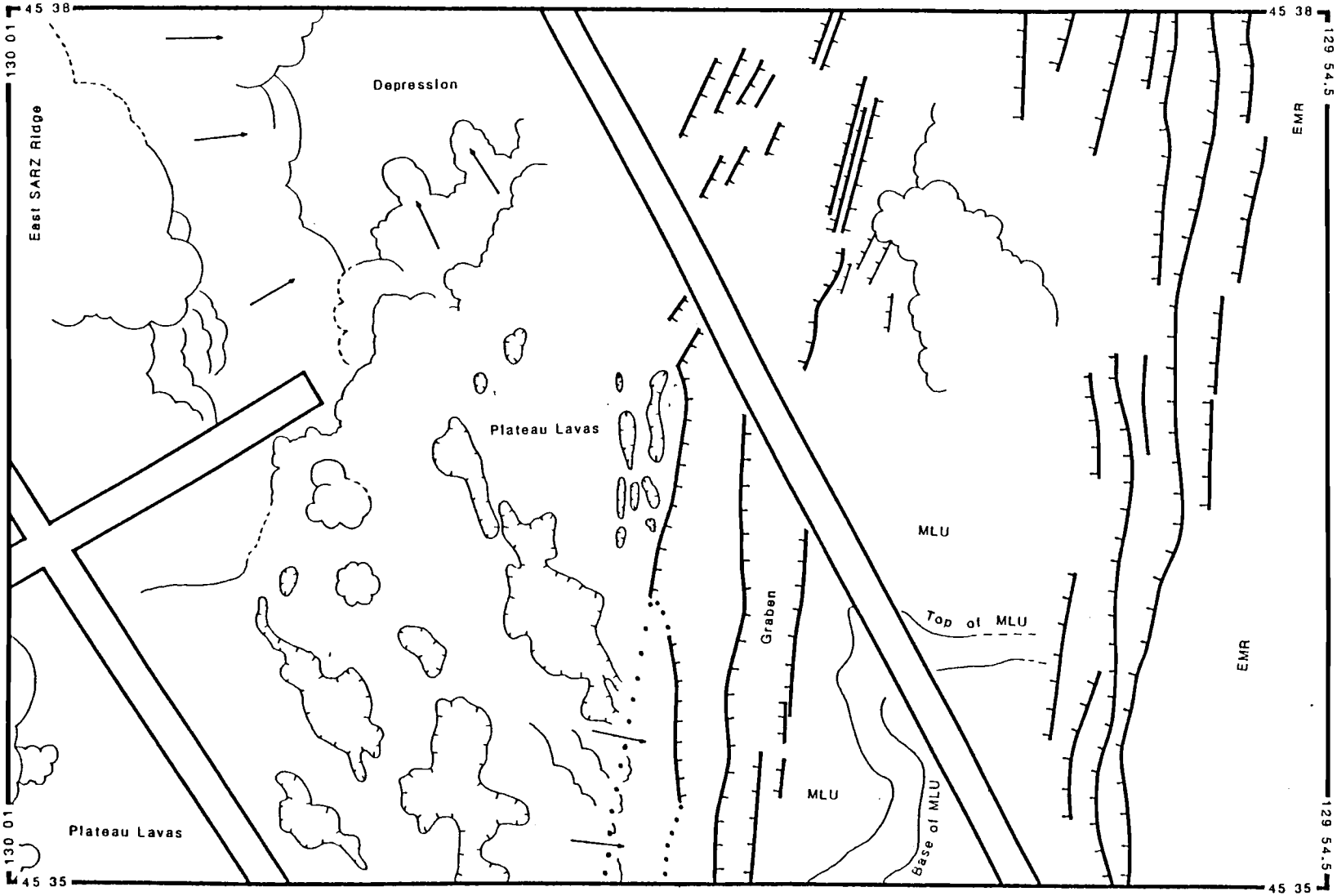
45 38
130 01
East SARZ Ridge
Depression
Plateau Lavas
Plateau Lavas
130 01
45 35
Graben
MLU
MLU
Top of MLU
Base of MLU
45 38
129 54.5
EMR
EMR
129 54.5
45 35

Figure 21 b.


45 38
130 01
129 54.5
45 35
Depression
Plateau
Plateau
West Valley Wall
West Valley Wall
Graben
Axial Valley
EMR
EMR
2500
2450
2400
2350
2300
2250
2200
2150
2100
2050

Figure 21 c.

Figure 22. Imagery of the Vance segment's axial valley, see Figure 17 for location. A) Sidescan mosaic, high backscatter is represented by light shades. B) Geological interpretation. Symbolism is consistent with that in Figure 19. C) SeaBeam bathymetry, 10 m contour interval.

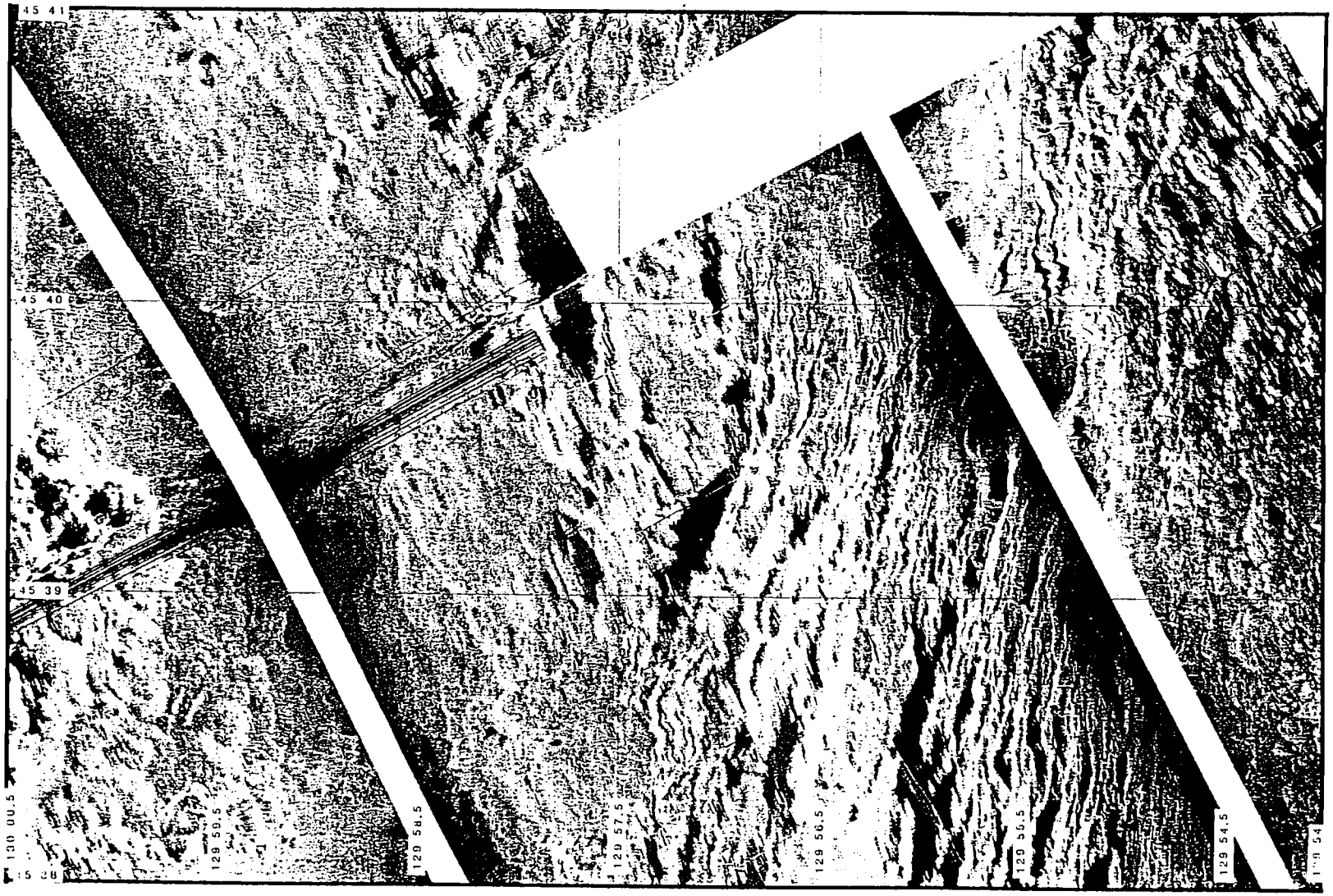

Figure 22 a.

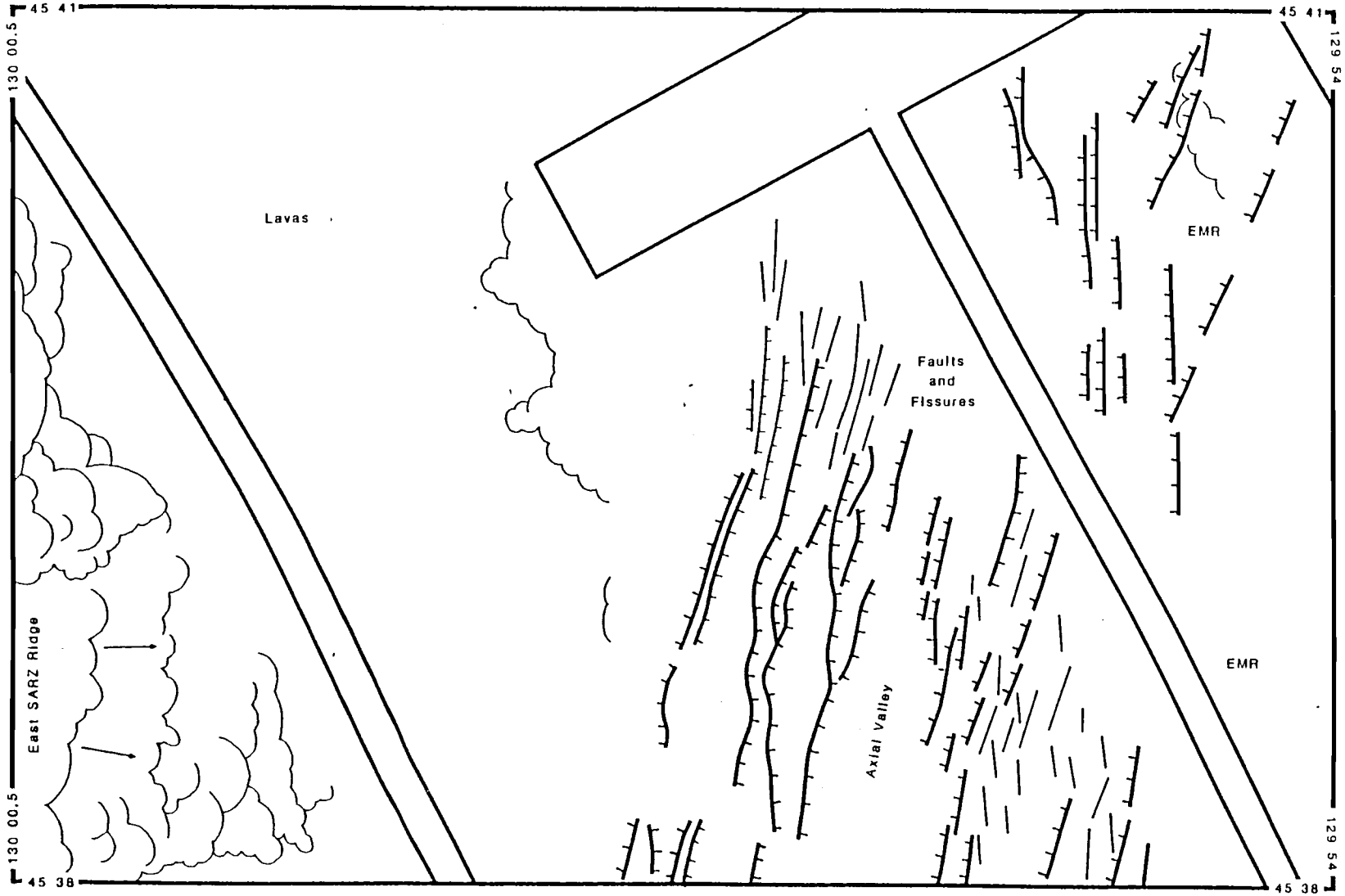
45 41
130 00.5
Lavas
East SARZ Ridge
Faults
and
Fissures
Axial Valley
EMR
EMR
129 54
45 38

Figure 22 b.

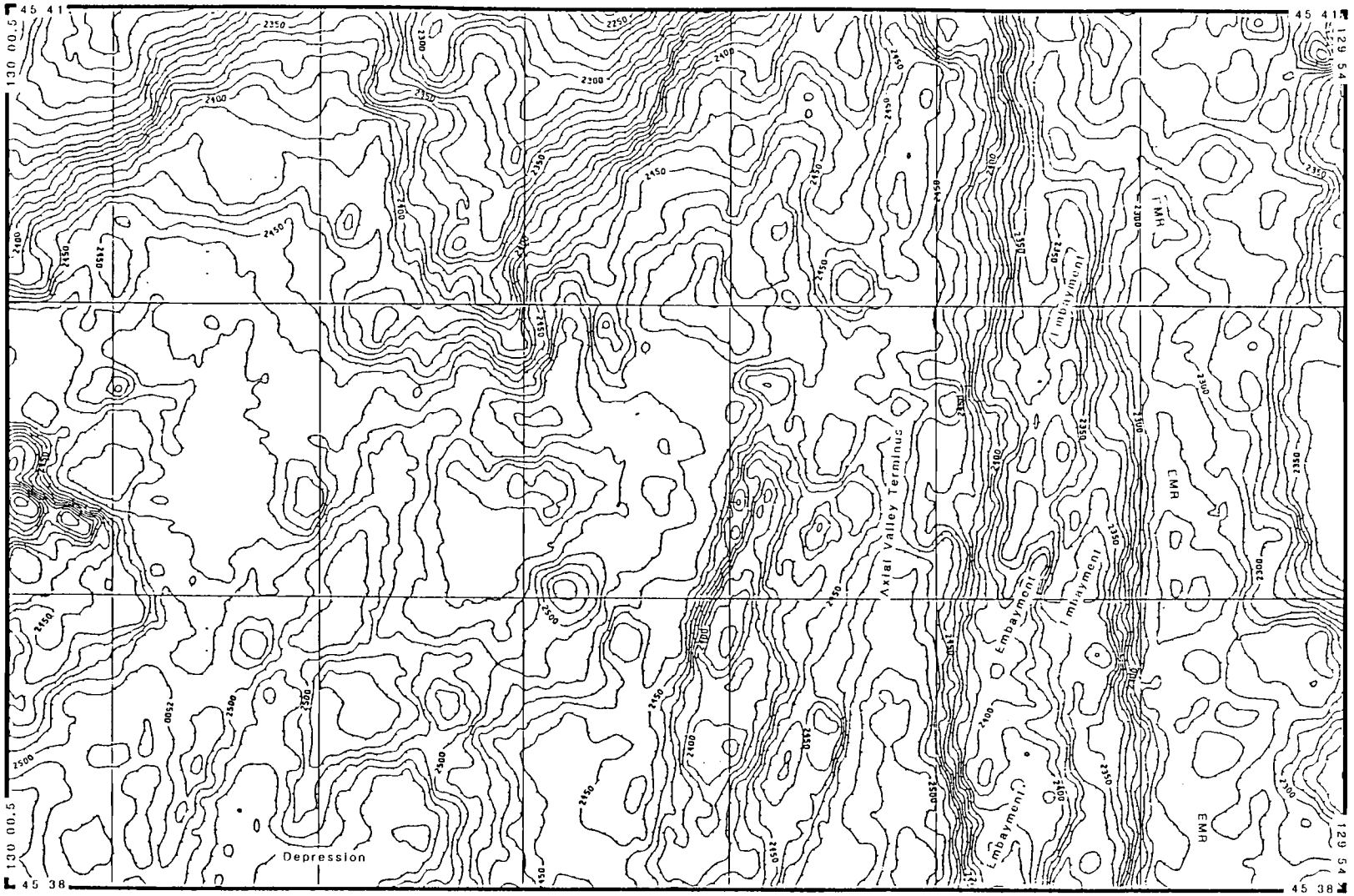
45 41
130 00.5
129 54
45 38
Depression
Axial Valley Terminus
Embayment
EMR
2350
2400
2450
2500

Figure 22 c.

130°01.5'W, a series of small-offset faults are visible. These faults are the southern tip of the next major valley-bounding fault to the north (evident in Figure 19), which is offset 500 m to the east. This fault segment displays 130 m of relief from valley floor to the top of the WMR (Figure 19c), and is the main valley-bounding fault on the west side of the valley between 45°29'N and 45°31'N. West of the main fault, several smaller faults are evident near 45°29.5'N/130°01.5'W, all of which face the valley except for one west-facing scarp near the southwest corner of Figure 19. The seafloor immediately west of the main fault displays low backscatter, probably due to greater sediment cover, implying an older age for the lavas there than in the valley floor below.

Between 45°30.75'N and 45°32.25'N, the west valley wall is divided into three short, right-stepping *en echelon* segments. These features are best seen in the bathymetry shown in Figure 19c. The offset between segments decreases with each successive offset to the north, ranging from 500 m to 200 m. The southern and middle segments appear broader and less steep, and display less vertical relief (60 to 80 m), than the valley wall to the south (ie., south of 45°30.75'N). Near the southern end of the middle segment (45°31.25'N), a 20-30 m high ridge extends from the western wall into the axial valley for several hundred meters, where it bends toward the southwest and trends parallel to the valley wall to about 45°30'N/130°00.2'W. Another ridge, displaying similar relief, extends into the axial valley from the north end of the middle segment near 45°31.8'N/129°59.5'W.

Outside the axial valley, west of the middle segment at 45°31.5'N, an extensive, flat, intermediate-backscatter lava field is visible on the sidescan imagery. This lava field is pockmarked by numerous negative-relief structures, and overlies faults that cut the low backscatter seafloor between the valley wall and the lava field. The lava field itself is not faulted, which indicates that it is younger than the dark seafloor and faults that it overlies. South of 45°31.25'N and north of 45°31.75'N, the lava field and the axial valley are separated by the positive relief of the WMR; however, lavas from this lava field can be traced through a saddle in the WMR at 45°31.5'N and down the upper part of the middle segment of the west valley wall (arrows on Figure 19b), where they overlie several small fault scarps. The backscatter pattern associated with these lavas extends through the offset between the south and middle segments and onto the valley floor (arrows, Figure 19b), and spreads along the base of the wall and out into the valley. The face of the middle scarp is veiled in acoustic shadow, and the presence or absence of lavas over the fault scarp itself cannot be resolved.

The northernmost of the three segments is steep, and displays 120 m of vertical relief (Figures 19c and 20c), similar to the valley wall south of 45°30.75'N. The high backscatter pattern of the scarp suggests that this is a sheer fault scarp. West of the scarp is the northern tip of the WMR, and beyond that, the lava field.

These observations suggest that lavas in the lava field west of the axial valley erupted after most of the faulting associated with the western valley wall and WMR occurred. The lavas spread outward to abut the western side of the WMR, and flowed downhill through the saddle in the WMR at 45°31.5'N. The lavas continued downhill, using the area of offset between the south and middle segments as a route to flow onto the floor of the axial valley. Although the faces of the middle and south segments of the wall here are constructional (in the sense that they are at least partially draped by lavas from the west), the *en echelon* geometry of the offset segments suggests that the primary relief associated with the valley wall here is due to tectonic processes, and the lavas overlie older fault scarps. Within the valley, the lavas flowed first inward and then toward the south, forming the ridge which extends into the axial valley from the base of the southern end of the middle fault segment. The presence of the ridge that extends into the axial valley from the north end of the middle segment (near 45°31.8'N/129°59.5'W) indicates that lavas may have breached the west valley wall at this location, although the sidescan data cannot confirm this, since this part of the wall is in shadow.

The eastern wall of the axial valley is also constructed from a series of offset fault scarps. A major west-facing boundary fault enters Figure 18 from the south at 130°58.75'W. This fault displays 120 m of vertical relief and trends N20°E to 45°27'N, where it abruptly terminates. Another inward-facing fault, located 500 m to the east, displays about 30 m relief south of 45°27'N. Relief along this fault increases to 150 m at the same latitude that the inner fault terminates. This outer fault accommodates nearly all of the relief along the west flank of the EMR northward to 45°29.5'N. Beyond this point the outer fault splays into a series of small-offset, west-facing faults that distribute the vertical relief between valley floor and EMR crest over an area 1.5 km wide (Figure 19).

The southern tip of a 30 m west-facing scarp is visible in Figure 18 near 45°27.5'N/129°59.3'W. This fault scarp is part of a linear series of faults that trend N20°E and gradually increase in vertical relief until, at 45°31'N/129°57.1'W, they become the primary valley-bounding faults and accommodate 80 m of vertical relief (Figure 19c). Between 45°27'N and 45°28'N, this fault defines the west side of a fault block. The surface of the fault block displays intermediate backscatter relative

to the high-backscatter seafloor within the axial valley and the low-backscatter seafloor atop the EMR. Lobate constructional features are evident on top of the block. The fault that defines the western side of the fault block is overlain by high-backscatter lavas of the axial valley south of 45°27.4'N; these lavas can be traced to the center of the axial valley. The surface atop the fault block displays backscatter that is intermediate in intensity relative to the seafloor within the axial valley to the east, and to the seafloor over the EMR. The difference in backscatter suggests that the lavas on the top of this block are somewhat younger than the lavas of the very dark (low backscatter) seafloor to the east, but were faulted up above the valley floor prior to the most recent episode of volcanism within the axial valley, which spawned the lavas that abut the west and south sides of the fault block.

A 40-60 m high volcanic ridge extends up the middle of the axial valley, located slightly east of the valley's geometric center. The crest of this central ridge is not well defined in the sidescan imagery (Figure 18a), although the SeaBeam bathymetry (Figure 18c) indicates that it extends along a N20°E trend from 45°26'N/130°0.75'W to 45°32'N/129°57.8'W (Figure 19c). A major constructional feature marks the crest of the ridge near 45°28'N/129°59.6'W (Figure 18), and several high-backscatter, low-relief lobate structures extend eastward from the ridge. The valley floor between the ridge and the valley's east wall is blanketed by lavas that display homogeneously high backscatter and lobate, positive-relief structures. These lavas stretch across the valley floor and abut the base of the valley wall, overlying older, less reflective lavas that are visible between flow lobes. The lavas also overlie older small-offset faults that are visible to the south. Elongate fingers of lava extend south from the main flow field and conform to the tectonic fabric within the valley, flooring narrow grabens and abutting the bases of small faults. Fault scarps are not evident in the most recent lavas east of the central ridge.

Another major constructional volcanic hill occupies the crest of the central ridge near 45°30.6'N/129°58.4'W (Figure 19). This structure is morphologically similar to the volcanic hill at 45°28'N/129°59.6'W; both structures appear in the bathymetry as local topographic highs on the crest of the central ridge, bordered on the east by the shallowly eastward-sloping floor at the axial valley. The east flank of the hill at 45°30.6'N exhibits high backscatter, and lobate constructional features radiate away from the hill's crest towards the east and south. The lobate features extend across the eastern floor of the axial valley, partially burying one eastward-facing fault, and abutting the base of another at 45°30.2'N/129°57.8'W. None of the lavas east of the hill are crosscut by younger faults.

Although none of the high-backscatter lavas on the east side of the central ridge are offset by faults, the ridge's west side is cut by several west-facing fault scarps. These faults have been partially overrun by lavas that can be traced from the crest of the central ridge and downslope over the faults, giving the linear faults a discontinuous appearance (e.g., near 45°27.5'N/130°00.25'W and 45°30.3'N/129°58.5'W). Flow-over-fault relationships can be seen best where the fault scarps face the sound source. In places where fault scarps face away from nadir, crosscutting relationships are difficult to determine because the faces of the scarps are cast in acoustic shadow.

The faults that define the western side of the central ridge also mark the eastern boundary of a 40 m-deep graben that occupies the western side of the axial valley (Figures 18c and 19c). South of 45°27'N, the western side of the graben is defined by several east-facing fault scarps (Figure 18). The floor of the graben here is covered by high-backscatter lavas that display subtle surface undulations and are not faulted. Near the base of the graben's west wall at 45°26.5'N/130°02'W, lobate constructional features protrude away from the wall toward the interior of the graben; fault scarps along the graben's west wall directly above these features are locally buried beneath high-backscatter lavas. West of the lobate structures, several sinuous positive- and negative-relief features extend across the top of a 1.0 km wide plateau situated between the graben and the west wall of the axial valley. The general outline of the area covered by the sinuous structures appears in the bathymetry as a subtle topographic high defined by the 2490 m contour. The sidescan imagery shows that the sinuous structures originate near a spot at the base of the valley wall where a small spur (marked by the 2460, 2470, and 2480 m contours) protrudes outward from the wall onto the plateau. Several sinuous structures extend towards the south and east, and abut the edge of the graben; another positive-relief structure meanders northward along the plateau and terminates in a bulb-shaped mound at 45°27.4'N/130°02'W (Figure 18a). The sinuous positive-relief structures are not fault-bounded, and appear to be constructional features. The local topographic gradient here slopes down towards the east.

The sinuous features on the plateau and the lobate structures at the base of the graben's west wall probably formed from lavas that flowed across the plateau from a source near or above the base of the valley's west wall. Where the flow intercepted the graben's west scarp, lavas cascaded stepwise down a series of faults, into the graben, and formed the small flow lobes that appear in the sidescan image as a line of scalloped, positive-relief structures aligned along the base of the faults. The

sinuous structures on the plateau are morphologically similar to pressure ridges that have been described on subaerial flows (Holcomb, 1980; Theilig and Greeley, 1986; Chitwood, 1987), and may represent submarine analogs.

Farther north, near 45°27.5'N/130°00.6'W, small faults on the floor of the graben are partially buried beneath lavas. Around 45°27.8'N/130°00.5'W, the graben's western fault system has been overlain by lobate lavas. The floor of the graben near the top of Figure 18 a (near 45°28.5'N/130°00'W) contains high-backscatter lavas that form constructional mounds with enough relief to throw acoustic shadows on the seafloor behind them. All these lavas could have erupted in place; however, several lines of evidence suggest that many of these lavas may have erupted on the crest or western flank of the central ridge and flowed eastward into the graben. The bathymetry (Figure 18c) indicates that the seafloor across the graben's entire width here slopes down towards the west. Three major lobate structures, each about 500 m in diameter, protrude into the graben from the east near 45°27.3'N/130°00.6'W, 45°27.9'N/130°00.5'W, and 45°28.3'N/130°00.3'W (evident in the bathymetry in Figure 18c). This part of the graben lies directly west of a large constructional hill on the central ridge. Lobate features extend south and east from the hill, indicating that the hill has served as a source for lavas that cover most of the eastern axial valley here. Several west-facing fault scarps along the east side of the graben are buried beneath lavas near 45°27.4'N/130°00.3'W. The proximity of the lavas within the graben to the volcanic hill on the central ridge, and the evidence of lavas from the central ridge burying faults on the east side of the graben here, suggest that the lavas on the graben floor are associated with volcanism along the central ridge.

In this same vicinity, a pair of volcanic ridges can be traced across the entire width of the graben floor, extending westward from the base of the graben's east wall at 45°27.75'N/130°00.3'W (Figure 18). These lavas are inferred to be related to volcanism associated with the central ridge for the reasons given above. A pair of ridges on the seafloor immediately west of the graben displays similar backscatter characteristics, and follows the same trend, as the ridges within the graben. These structures appear to be related features, although their continuity is interrupted at 45°28.2'N/130°00.6'W by the eastward-facing fault that defines the west side of the graben. These two pairs of ridges are inferred to have been initially contiguous, and to have been displaced by movement along the graben's western fault.

The morphology of the western valley graben changes near 45°29.5'N. South of this point, between 45°28'N and 45°29.5'N, the western and eastern margins of the graben are distinct, marked by inward-facing faults that are well-defined in the sidescan imagery (Figures 18a and 19a). Between 45°29.5'N and 45°32'N, however, the faults along the graben's east margin become distributed over a 500 m wide area. These faults are locally overlain by lavas, giving the faults a segmented, discontinuous appearance. The lavas that bury the faults can be traced uphill to the central volcanic ridge, which flanks the graben to the east. The graben's western faults become indistinct near 45°29.8'N, and north of 45°30'N only one small-offset, eastward-facing fault is visible along the trend of the west margin of the graben. The seafloor within the axial valley near 45°30.5'N/129°59.5'W displays homogeneous intermediate backscatter; this area corresponds to the position of a subtle ridge, evident in the bathymetry, that can be traced from the base of the west valley wall, into the axial valley, and across the graben. This region is located directly below the site where lavas, originating from the plateau west of the axial valley, flowed over the west valley wall. The structures evident in the bathymetry and sidescan sonar imagery indicate that these lavas probably overlie the western part of the axial valley, the eastern wall of the graben, and part of the floor of the graben, covering an area roughly defined by the 2480 m isobath between 45°30'N and 45°31.8'N.

--- *The Vance Segment From 45 °32'N to 45 °40'N*

The physiography of the axial valley changes dramatically near 45°32'N. In general, the axial valley between 45°32'N and 45°40'N exhibits three significant morphological characteristics: 1) A progressive decrease in the distance between the valley walls towards the north, resulting in an axial valley that tapers to a point at 45°39'N; 2) an extensive, thick lava unit (or series of units) that covers the valley floor nearly wall-to-wall, which erupted west of the axial valley and flowed eastward over the west valley wall into the axial valley; and 3) a shallow, narrow graben, incised atop the large lava unit, that extends roughly up the center of the axial valley. Each of these features will be discussed in more detail below.

The west wall of the axial valley exhibits a very different morphology north of 45°32.3'N compared to its expression farther south. At this point, the wall is offset to the west by 500 m, and the vertical relief over the wall decreases from 150 m to 40 m (Figure 20c). The slope of the wall also decreases here, changing

abruptly from 15° (south) to 6° (north). Between 45°32.3'N and 45°37'N, the west wall is composed of three linear scarps (evident in the bathymetry of Figures 20c and 21c), which are separated by left-stepping offsets at 45°35.9'N (200 m offset), at 45°36.7'N (100 m offset), and at 45°36.9'N (250 m offset). Each of the segments trends roughly N20°E, and all display shallow slopes showing 30 m-40 m of total relief.

Several lines of evidence indicate that the west valley wall here (between 45°32'N and 45°37'N) is composed of scarps which were formed tectonically and subsequently buried beneath eastward-flowing lavas. The linear, segmented nature of the scarps suggests that they are tectonic in origin, and the N20°E trend of the scarps is comparable to the general N20°E orientation of the axial valley's western boundary faults farther south. The sidescan imagery over this region (Figures 20a and 21a), however, reveals that discrete fault scarps are not apparent along this part of the west wall (with a significant exception between 45°32.8'N and 45°33.6'N). Instead, the seafloor over the west valley wall displays intermediate to high backscatter similar in intensity to the backscatter of the seafloor on either side of the wall.

A wide, flat plateau lies immediately west of the axial valley. The surface of the plateau displays homogeneous intermediate-intensity backscatter, and is pockmarked by numerous pits and depressions that display as much as 30 m of negative relief (Figure 20a). The interiors of the depressions typically exhibit high backscatter relative to the top of the plateau. The plateau's surface, defined by the 2420 m isobath, is 40 m above the most shallow point at the base of the west valley wall, and 110 m higher than the deepest part of the western axial valley. The plateau region is interpreted as a large plain that has been covered by flat-lying lavas.

The presence and shape of constructional volcanic features near the valley's west wall indicate that lavas flowed eastward from the plateau into the axial valley. Near 45°32.75'N/130°59.5'W, lavas from the plateau overlie the west valley wall and extend eastward into the axial valley. The lavas drape a 1 km-wide section of the wall, burying several well-defined eastward-facing fault scarps. Immediately north of this spot lies an island of low backscatter that is surrounded by higher backscatter seafloor. This feature is interpreted to be a kipuka, a remnant of older seafloor that has been isolated by plateau lavas that flowed around it to the north and south (see Takahashi and Griggs (1987) for an illustration of a subaerial kipuka). The boundaries of the kipuka are distinct: the east side of the kipuka is defined by the axial valley's western boundary faults, which are not covered by plateau lavas

between 45°32.8'N and 45°33.6'N. The contact between the high-backscatter plateau lavas with the darker surface of the top of the kipuka is clear. The low backscatter evident on the upper surface of the kipuka could be due to either or both of two reasons: the dark areas could be acoustic shadows cast by topographic highs, or they could be the result of low-surface-roughness material there. The kipuka displays slight positive relief (≈ 10 m) in the SeaBeam bathymetry (Figure 20c); however, the topography here does not appear sufficiently rugged to cause large acoustic shadows. Furthermore, digitally enhanced sidescan sonar images of the kipuka show subtle structures within the low backscatter area. The dark area atop the kipuka therefore probably represents low surface roughness rather than acoustic shadow. Similar low-backscatter patterns are evident along the crest of the EMR farther south; all of these surfaces are probably blanketed by sediments, and of a similar age.

The west valley wall between 45°33.6'N and 45°36'N is characterized by 1) the absence of exposed fault scarps, 2) the presence of elongate constructional features oriented transverse to the trend of the wall, and 3) the presence of similar appearing, high-backscatter lavas on either side of the wall. Lavas are inferred to have flowed eastward into the axial valley here, burying preexisting fault scarps. The fault scarps that define the eastern margin of the kipuka disappear below nadir at 45°33.6'N, and are not apparent farther north. A series of small acoustic shadows are arranged *en echelon* along the N20°E trend of the west valley wall between 45°34'N and 45°34.5'N. These features do not display the well-defined linear shape indicative of bare fault scarps, and are not associated with positive-relief structures capable of casting acoustic shadows. Several narrow ribbon-like high-backscatter features extend downslope from between the shadows; these high-backscatter ribbons are interpreted to represent constructional volcanic features associated with lavas that flowed down the west valley wall from the plateau. The acoustic shadows probably indicate either steep areas along the west valley wall where the lavas incompletely buried the underlying fault scarp, or depressions between lava channels over the scarp. The entire length of the west wall between 45°34.5'N and 45°36'N (Figures 18a and b, 19a and b) is blanketed by lavas that display the same general backscatter characteristics as the lavas on the plateau to the west.

North of 45°37'N, the continuity of the west valley wall deteriorates, and between 45°37'N and 45°39.5'N the axial valley is bounded to the west by a series of short (≈ 1 km), discontinuous, fault-bounded ridges (evident in the bathymetry of Figures 21c and 22c). The ridges are defined by east- and west-facing faults that

trend roughly N20°E; individual faults display up to 80 m of vertical relief. The western margin of the axial valley here is defined by a series of east-facing fault segments; a right-stepping offset in the valley wall occurs at 45°37.7'N/130°57.2'W (Figure 21). At 45°39.5'N, the ridges west of the axial valley terminate in a dense field of closely-spaced small-offset faults and fissures, and faulting associated with the west side of the axial valley is not visible north of 45°40'N (Figure 22a).

The morphology of the east valley wall north of 45°32'N differs significantly from that of the west valley wall. Whereas the west wall is composed of a few low-relief fault scarps that have been buried beneath extensive lava flows, the east valley wall displays high vertical relief, and its steep sides are not covered by lavas. Fault segments near the northern terminus of the east valley wall display left-stepping offsets, which result in a progressive decrease in valley width towards the north.

A 1 km-wide band of small-offset fault scarps distribute the vertical relief between the valley floor and the crest of the EMR between 45°32'N and 45°33'N. North of this point, most of the vertical relief along the east wall of the axial valley is concentrated over a steep, narrow scarp (Figure 20). The east valley wall between 45°32'N and 45°37'N is essentially continuous, and displays no major offsets. Total relief over the wall is as great as 210 m at 45°37'N, and the slope of the wall is steep (18° at 45°35'N). The general strike of the valley's east wall gradually bends from N20°E at 45°32'N to nearly N00°E at 45°36.5'N; this curvature is also evident in the orientation of the crest of the EMR (best seen in the regional bathymetry shown in Figure 2). The fault scarps that compose the east wall here bend in a similar manner. North of 45°37'N, the crest of the EMR continues to gradually curve towards the west, and this curvature is reflected in the orientation of fault scarps along the upper part of the western flank of the EMR.

Between 45°37'N and 45°40'N, two tectonic trends are evident along the wall that separates the axial valley from the top of the EMR: a N20°E fabric, and the N00°E-trending faults below the crest of the EMR. The N00°E-trending faults on the upper west flank of the EMR are presumably associated with the tectonic activity that created the vertical relief of the EMR, since they can be traced southwards parallel to the crest of the EMR. The faults near the base of the western flank of the EMR (nearest to the axial valley at 45°38.5'N/129°55.9'W)) are oriented N20°E Figure 22). Several N20°E-trending faults, which are aligned with the faults near the axial valley, crosscut structures atop the EMR. Crosscutting relationships are clearly displayed in the sidescan imagery near the top of the EMR between 45°39'N and

45°40'N, where lobate constructional features are cut by N20°E-trending faults. Along the bottom half of the east valley wall, near 45°38.5'N/129°55.5'W, the intersection of the N00°E and N20°E trends lend a distinctly chaotic appearance to the seafloor. Over this chaotic zone, the sidescan imagery alone is not able to unequivocally resolve whether one trend postdates the other, although the N20°E trend is the most dominant of the two. However, the detailed bathymetry over this area reveals several narrow embayments on the upper part of the west side of the EMR around 45°39'N/129°55.6'W (Figure 22c); these embayments correspond to the location of faults that penetrate into the west flank of the EMR. The presence of N20°E-trending faults cutting into the west flank of the EMR (which is constructed along N00°E faults), in conjunction with the evidence of N20°E-trending faults crosscutting volcanic structures near the crest of the EMR, suggests that the N20E faults postdate the N00°E faulting.

The N20°E faults appear to be associated with the northern tip of the Vance segment's axial valley, and the N00°E-trending faults at this latitude (≈45°30'N) are related to the EMR. Given that the N20°E faults postdate the N00°E faults, the formation of the northern axial valley is inferred to have occurred after the EMR was constructed.

North of 45°37'N, several successive fault scarps along the east margin of the axial valley step towards the left. As a result, the axial valley decreases in width towards the north. Most of the N20°E-trending faults associated with the east valley wall dissipate between 45°39'N and 45°40'N, although N20°E fault scarps may be traced northwards across the EMR to 45°41'N. The axial valley does not persist north of 45°39'N. The EMR and the faults near its crest, however, can be traced as far north as 45°41.5'N. At its northern terminus near 45°41'N/129°55'W, the crest of the EMR trends N05°W (Figure 2).

The morphology of the seafloor within the axial valley changes dramatically north of 45°32'N. The east valley wall, as discussed above, gradually converges towards the west valley wall, resulting in a progressive decrease in valley width and, ultimately, the termination of the axial valley at 45°39'N. Two other significant features within the valley are resolved in the sidescan sonar imagery north of 45°32'N: 1) A major lava unit (or series of lava units) that covers most of the valley floor between 45°33'N and 45°37'N; and 2) a series of small-offset faults, oriented parallel to the trend of the axial valley, that offset the lavas and define a narrow, shallow graben that extends up the center of the valley. The detailed structure of the axial valley north of 45°32'N is discussed below.

The axial valley's central ridge and western graben are evident in the SeaBeam bathymetry between 45°32'N and 45°33'N (Figure 20c). As was the case farther south, the ridge and graben are separated by a series of west-facing, small-offset fault scarps. Individual scarps are not continuous, and the sidescan imagery indicates that the faults are locally overlain by lavas (Figure 20a). Elongate high-backscatter patterns extend downslope from the central ridge and merge with lobate constructional features that bury fault scarps near 45°32.25'N/129°58'W. The lavas that overlie the fault scarp therefore probably erupted along the crest or western flank of the central ridge. The area east of the central ridge displays homogeneous intermediate backscatter, and no fault scarps are evident on the floor of the eastern part of the axial valley.

The west valley graben, the central ridge, and most of the floor of the axial valley are buried beneath a very large body of lavas near 45°33'N. The point where the lavas overlie the central ridge and the graben lies beneath the path of the towfish at 45°33'N/129°58'W and cannot be seen. However, the southern boundary of the major lava unit (or MLU) is evident on either side of nadir (Figure 20b). The boundary of the MLU is defined by a series of low-relief ridges, valleys, and elongate lobes that extend down the face of the constructional scarp. There is little backscatter difference between the MLU and the lavas on the floor of the axial valley -- both display homogeneous intermediate to high backscatter. The southern boundary of the MLU is also evident in the SeaBeam bathymetry: the top of the MLU is roughly defined by the 2470 m isobath, and vertical relief along the southern flow boundary varies from 70 m over the west valley graben to 10 m over the central ridge. The base of the MLU trends diagonally (≈ N50°E) across the axial valley from a point near the base of the west valley wall at 45°32.5'N/129°58.5'W to 45°33.7'N/129°56.4'W. Lavas are also piled up along the base of the axial valley's west wall, and cover the west side of the west valley graben, near 45°32'N/129°59'W.

The eastern boundary of the MLU can be traced northward up the axial valley from 45°34'N/129°56.5'W. The eastern scarp of the MLU displays steep slopes (up to 18°) and great vertical relief (as much as 90 m). In the bathymetry, the outline of the scarp is irregular and displays two large embayments between 45°34.5'N and 45°35.75'N (Figure 20c and 21c). The MLU abuts the east valley wall at 45°46'N; south of this spot the main body of the MLU does not completely fill the axial valley.

The northern limit of the MLU is not well defined. North of 45°36'N the topography within the axial valley is irregular, and a discrete scarp associated with the edge of the MLU, such as the scarp that marks the MLU's southern and eastern boundaries, is not present. The sidescan imagery does not indicate the presence of a flow boundary based on backscatter patterns. Several lobate constructional features, which may be related to the MLU, overlie several small-offset fault scarps near 45°37'N/129°56.0'W (Figure 21). High-backscatter lavas occupy the floor of the axial valley as far north as 45°38.8'N. Given the lack of a well-defined northern flow boundary for the MLU, it is conceivable that lavas from the MLU could extend to the northern tip of the axial valley.

The lavas that compose the MLU appear to be related to the lavas that flowed eastward over the west valley wall from the plateau located west of the axial valley. Lobate constructional features can be traced from the plateau, over the west wall, and onto the MLU at 45°32.6'N (Figure 20). Several flow features that descend across the west wall north of 45°34'N also continue across the top of the MLU.

The surface of the MLU is cut by a series of small-offset faults oriented parallel to the strike of the axial valley. A shallow, 250 m-wide graben extends up the center of the MLU, defined by several linear fault scarps (Figures 20 and 21). The graben is aligned with the faults that separate the central ridge from the western graben in the axial valley south of the MLU. This relationship can be seen by projecting the trend of the graben's axis southward beyond the southern margin of the MLU. Progressing northwards, the axis of the graben curves gradually towards the west: at 45°33.5'N, the graben strikes N10°E (Figure 20); where it disappears beneath nadir at 45°36.5'N, the graben is oriented nearly N00°E (Figure 21).

Another fault scarp is evident along the west side of the MLU, located inboard of the base of the west valley wall between 45°32'N/129°59.2'W (Figure 20) and 45°35.8'N/129°57.75'W (Figure 21). This fault crosscuts lobate volcanic structures that extend into the axial valley below the spot where plateau lavas overlie the west valley wall near 45°32.6'N/129°59'W (Figure 20). The fault can be traced northward as a well-defined, east-facing scarp to 45°34.2'N/129°58.25'W. Between this point and 45°35.2'N/129°57.8'W, the scarp appears indistinct, and is inferred to be overlain by lavas that have entered the valley from the plateau to the west. Beyond 45°35.2'N/129°57.8'W the scarp is not covered by lavas, and it curves westward and merges with the scarp along the west valley wall at 45°35.8'N/129°57.75'W.

The surface of the MLU is relatively flat compared to the interior of the axial valley farther south. However, two slight topographic highs are present on the east side of the MLU, one around 45°33.8'N/129°57.2'W which rises 30 m above the surface of the MLU, and another near 45°35.25'N/129°57'W which is 20 m higher than the MLU's surface (Figure 20). Three different explanations could account for the presence of these topographic highs: 1) the lavas around the topographic highs erupted *in situ* as part of the central volcanic ridge system, prior to the emplacement of the EMU, and are not related to the MLU lavas; 2) the topographic highs were distal, tube-fed eruptive centers for MLU lavas; or 3) the relief between the topographic highs and the surface of the MLU resulted from faulting that occurred after the emplacement of the MLU.

The first scenario implies that the lavas on the topographic highs predate the MLU lavas, and that any lavas entering the axial valley from the west would have been dammed by the western flanks of the central ridge. However, the continuity of the distinctive flow boundary around the south and east sides of the MLU, and around the topographic highs, suggests that the lavas were emplaced concurrently, and in a similar manner. The morphology of the eastern flanks of the topographic highs also differs from that of topographic highs along the central ridge to the south (near 45°28'N/130°59.6'W and 45°30.6'N/129°58.4'W), which display gently dipping sides covered by subtle lobate constructional features.

Either of the second two scenarios is plausible. The shoalest parts of the topographic highs are still deeper than the surface of the plateau west of the axial valley, and therefore a lava tube system originating from the plateau could have fed volcanic vents capable of constructing the topographic highs at the distal edge of the MLU. The presence of the central graben on the MLU indicates that tectonic activity has modified the MLU lavas after they were emplaced. The western flanks of the topographic highs are defined by linear isobaths oriented parallel to the trend of the graben (Figures 20c and 21c), suggesting that the relief between the topographic highs and the rest of MLU could be the result of faulting. Each of these two scenarios implies that the lavas of the topographic highs are associated with the MLU lavas.

The South Rift Zone of Axial Volcano

The south Axial rift zone (SARZ) appears in the regional bathymetry as a topographic high that trends roughly S10°W from the summit plateau of Axial

volcano (Figure 2). The rift zone is composed of three discrete ridges. A west ridge and a middle ridge can each be traced from the summit plateau southwards to 45°34'N, and a more diminutive east ridge extends between 45°43'N and 45°34'N. A field of volcanic cones, which also appears to be related to the SARZ, lies immediately south of the southern termini of the west and middle ridges. The sidescan sonar imagery (plate 1) reveals that the SARZ region displays high backscatter. The western boundary of the SARZ is defined by the backscatter contrast between SARZ lavas and the low-backscatter seafloor to the west (Plate 1); this contact is well defined in the north, but becomes progressively more indistinct towards the south. The southern and eastern margins of the SARZ are defined bathymetrically: the southern boundary is located along the southern edge of the field of volcanic cones, roughly near 45°27'N; and the eastern boundary occurs along the edge of the east SARZ ridge, along 130°01'W. The detailed bathymetric and backscatter characteristics of the SARZ region are shown in Figures 23 through 27, and are further discussed below.

The detailed bathymetry over the SARZ area indicates that neither the west nor the middle ridge is a simple, linear feature. As shown in Figures 23c through 25c, the crests of each ridge are discontinuous, and bifurcate repeatedly down axis. Subsidiary ridges diverge from both of the main ridges, and parallel the general strike of the rift zone. The area between the west and middle ridges is occupied by these minor ridges; for example, a subsidiary ridge can be traced southward from the base of a volcanic cone near 45°45'N/130°03.5'W (Figure 23c) to 45°42.7'N/130°04.1'W (Figure 24c). Subsidiary ridges also cover the flanks of the SARZ area, as shown near 45°46.3'N/130°01.4'W (Figure 23c).

The depth of the west and middle SARZ ridge generally increases towards the south, although numerous topographic highs occur locally along their crests. Most of the topographic highs are elongate parallel to the axis of the rift zone; however, several appear nearly circular in plan view, such as the cone at 45°45.4'N/130°03.4'W (Figure 23c), and minor ridges radiate from the summits of others (e.g., the cones at 45°39.9'N/130°04.5'W and 45°38.8'N/130°06.4'W in Figure 25c).

The crests of the west and middle ridges are not as easily identified in the sidescan sonar imagery (Figures 23a through 25a) as they are in the bathymetry. However, the general S10°W orientation of the ridges, evident in the bathymetry, is mirrored by a pervasive S10°W fabric in the sidescan imagery over the SARZ region. This appearance results from the presence of several volcanic ridges and

Figure 23. Imagery of the south rift zone of Axial volcano, see Figure 17 for location. A) Sidescan mosaic, high backscatter is represented by light shades. B) Geological interpretation. Symbolism is consistent with that in Figure 19. C) SeaBeam bathymetry, 10 m contour interval. The convoluted region near 45°44.5'N/130°03.5'W is an artifact of the contouring program.

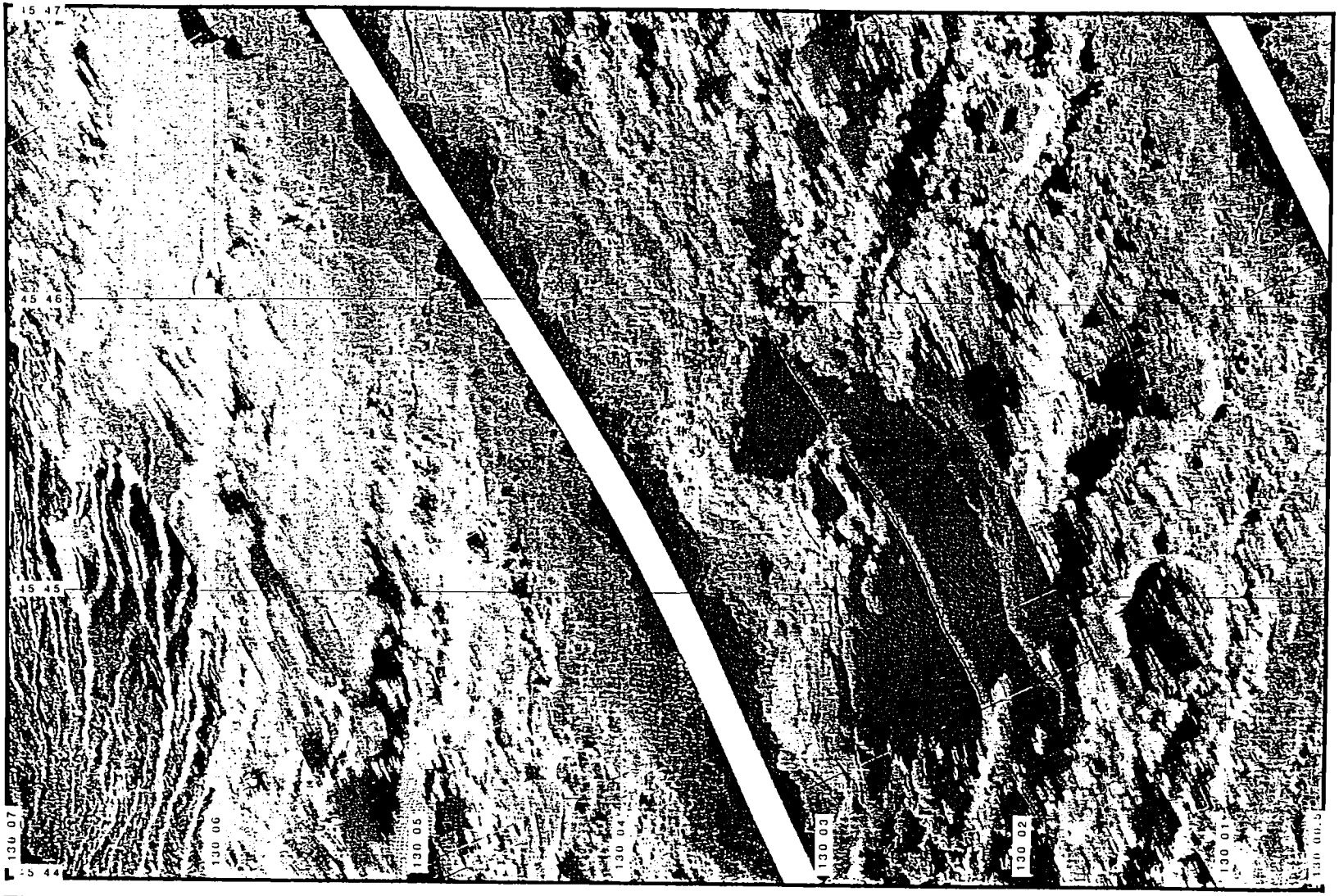
15 47
45 46
15 45
15 44
130 07
130 06
130 05
130 04
130 03
130 02
130 01
130 00

Figure 23 a.

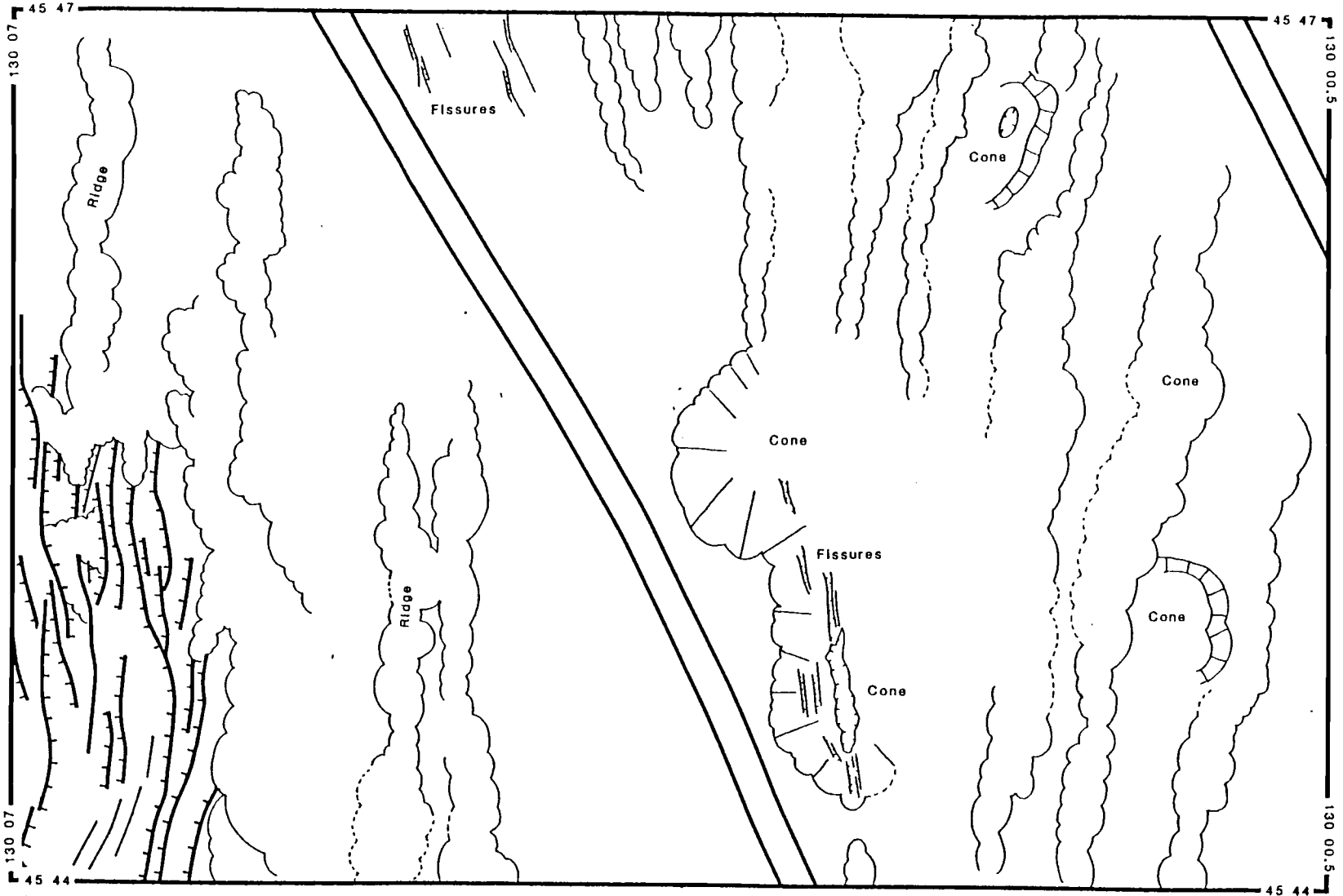
45 47
130 07
130 00.5
Fissures
Ridge
Cone
Cone
Cone
Fissures
Ridge
Cone
Cone
45 44

Figure 23 b.

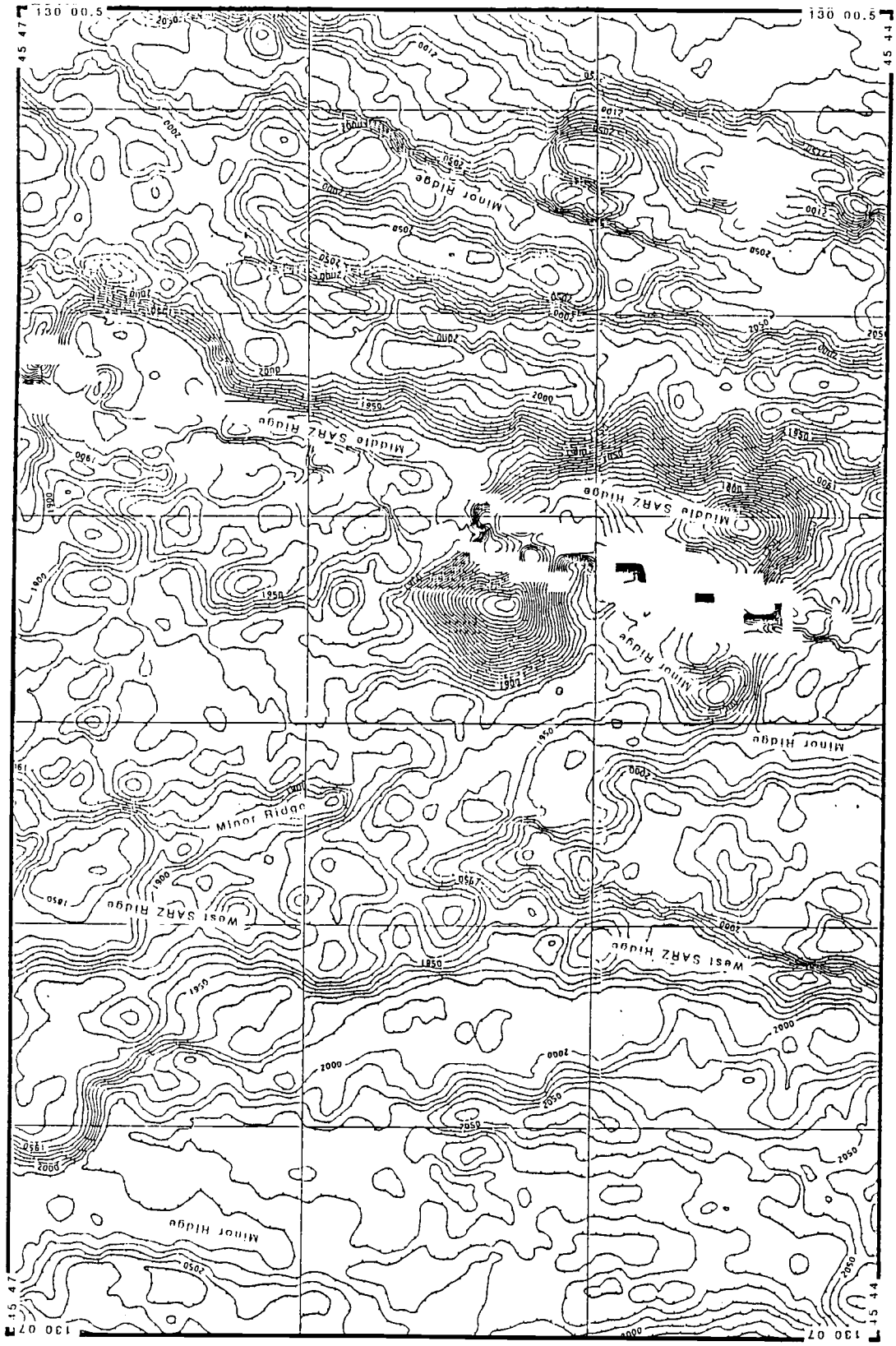
130 00.5
45 47
45 44
130 07
Minor Ridge
Middle SARZ Ridge
West SARZ Ridge

Figure 23 c.

Figure 24. Imagery of the south rift zone of Axial volcano, see Figure 17 for location. A) Sidescan mosaic, high backscatter is represented by light shades. B) Geological interpretation. Symbolism is consistent with that in Figure 19. C) SeaBeam bathymetry, 10 m contour interval.

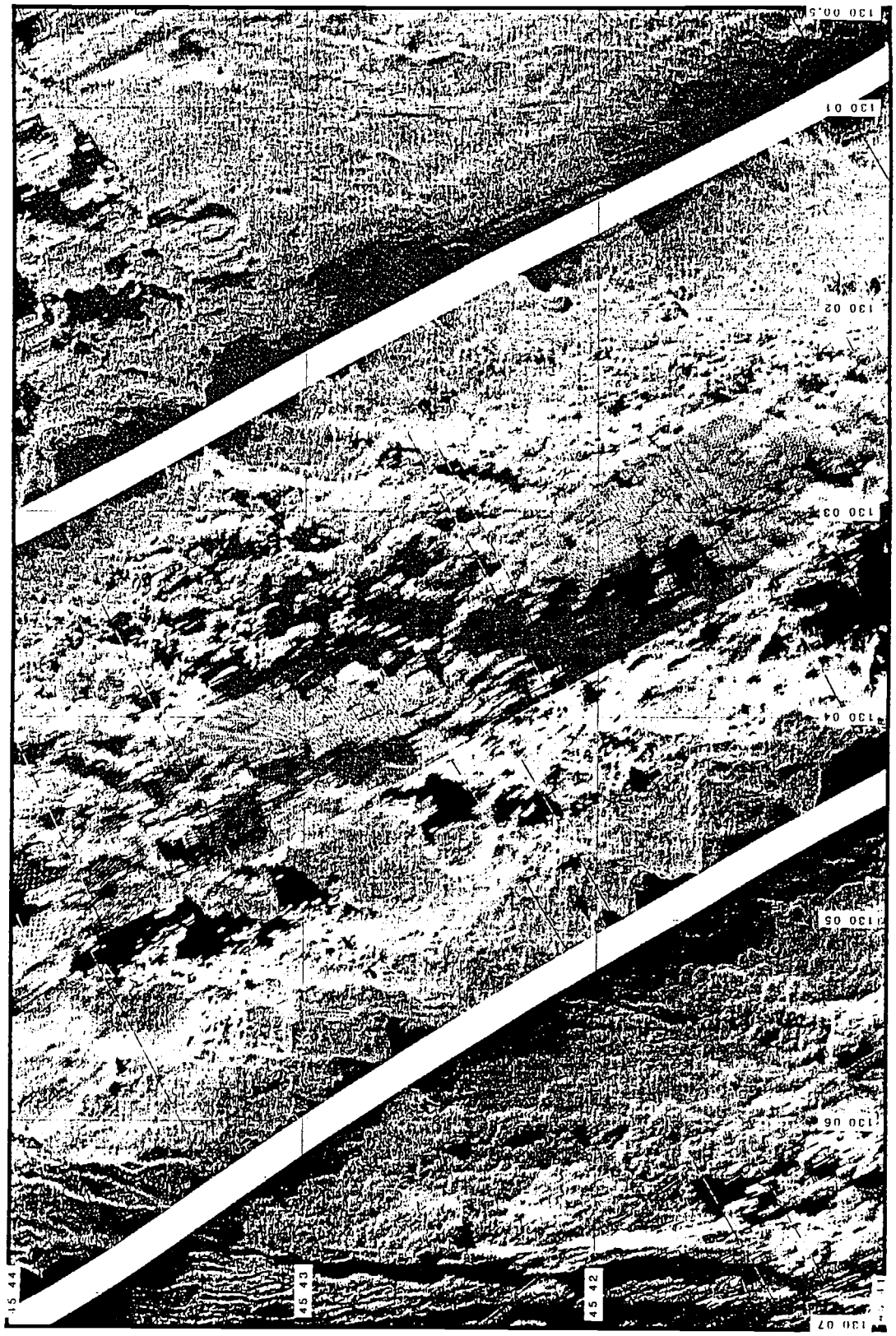
130 00.5
130 01
130 02
130 03
130 04
130 05
130 06
130 07
45 44
45 43
45 42

Figure 24 a.

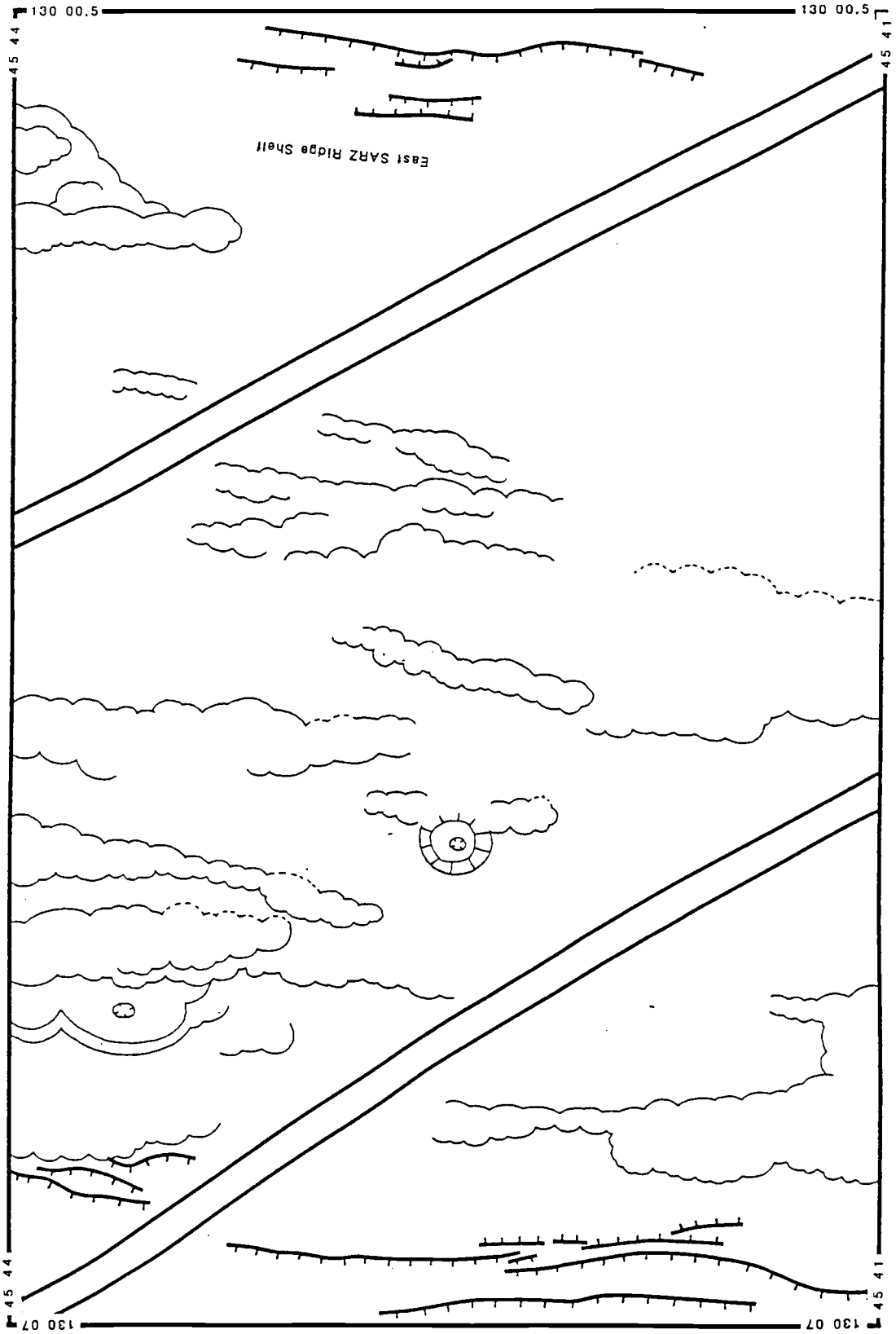
130 00.5
130 00.5
45 44
45 41
East SARZ Ridge Shelf
45 44
45 41
130 07
130 07

Figure 24 b.

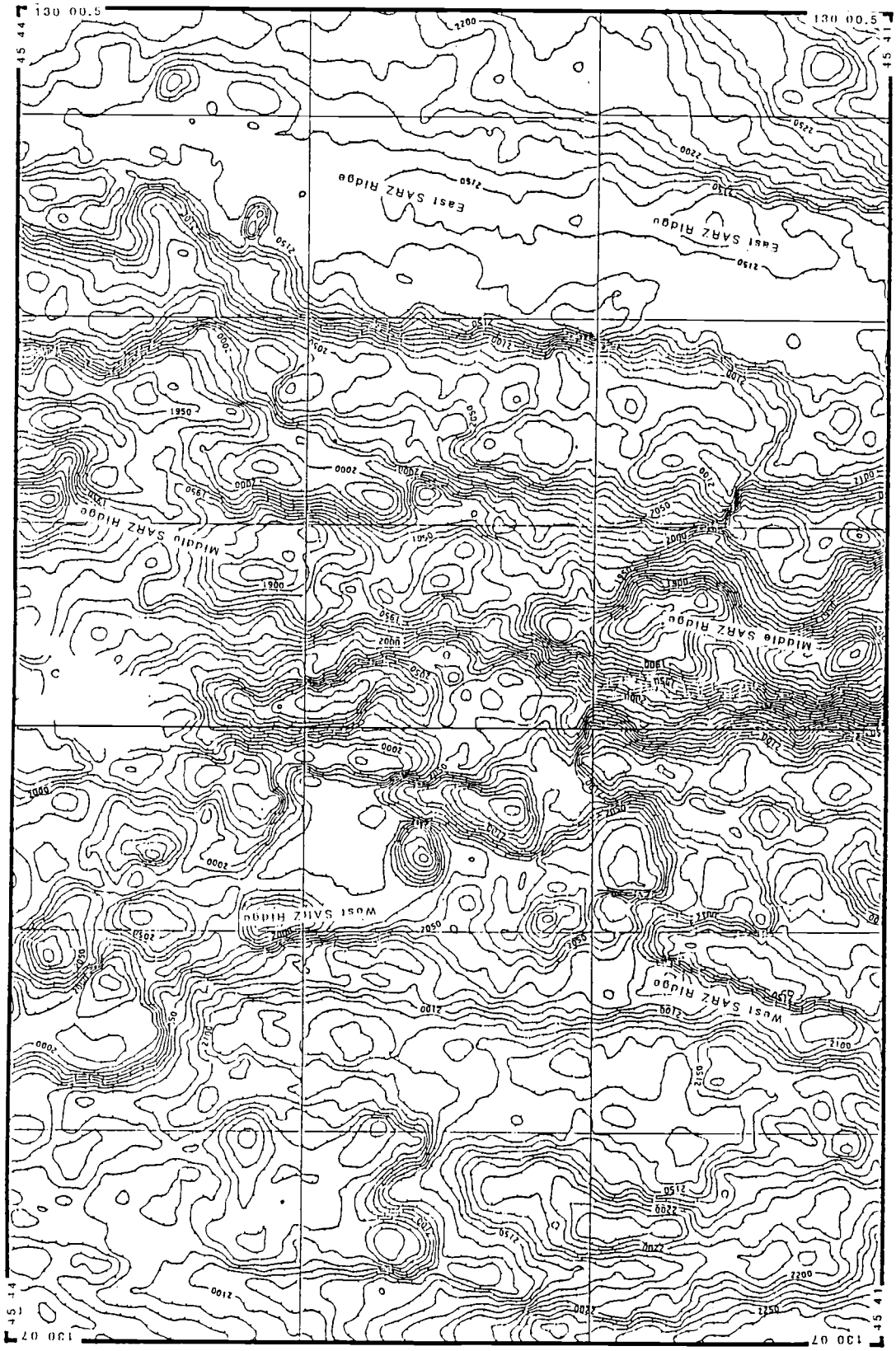
130 00.5
45 44
East SARZ Ridge
Middle SARZ Ridge
West SARZ Ridge
130 07
45 41

Figure 24 c.

Figure 25. Imagery of the south rift zone of Axial volcano, see Figure 17 for location. A) Sidescan mosaic, high backscatter is represented by light shades. B) Geological interpretation. Symbolism is consistent with that in Figure 19. C) SeaBeam bathymetry, 10 m contour interval.

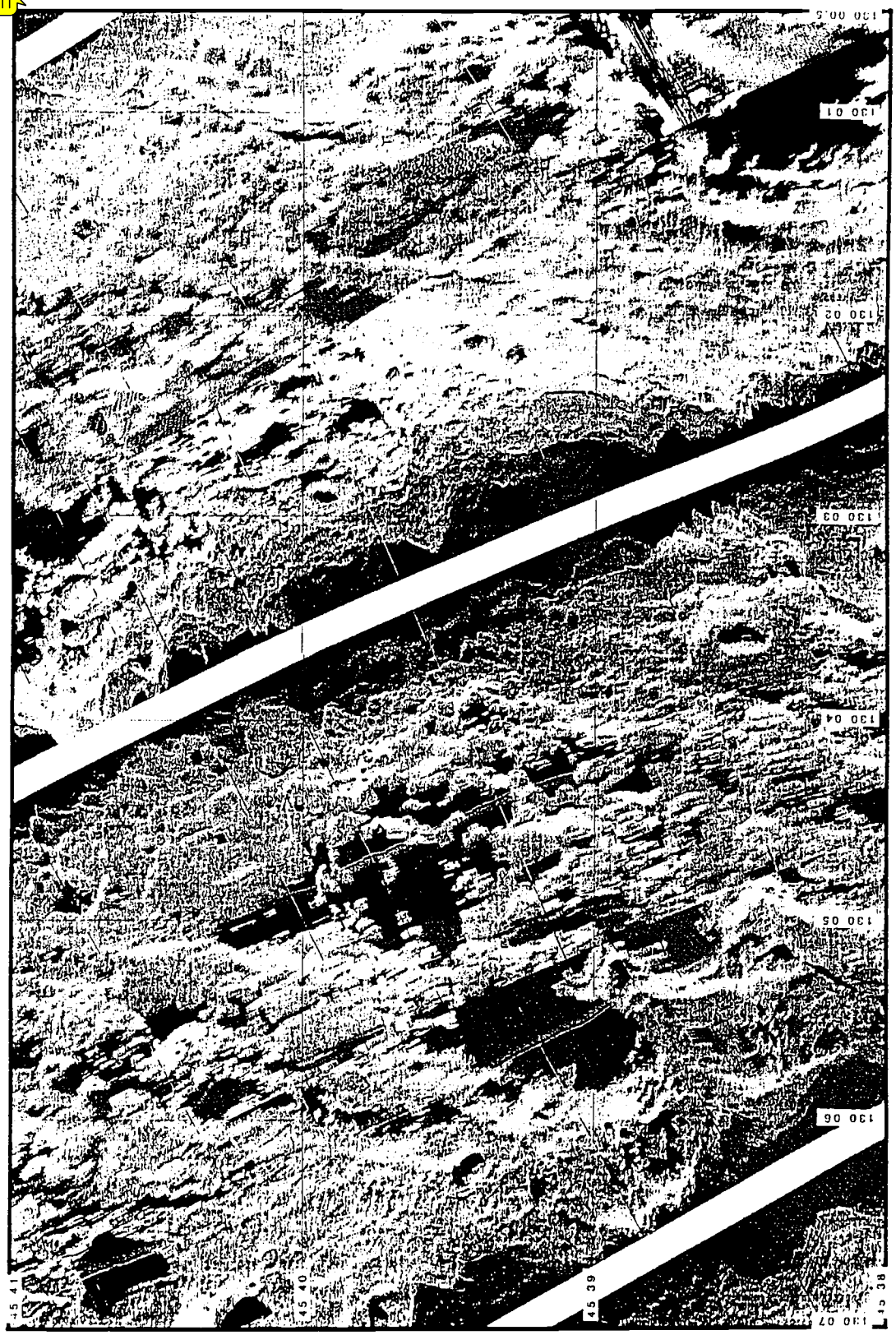
130 00.5
130 01
130 02
130 03
130 04
130 05
130 06
130 07
45 41
45 40
45 39
45 38

Figure 25 a.

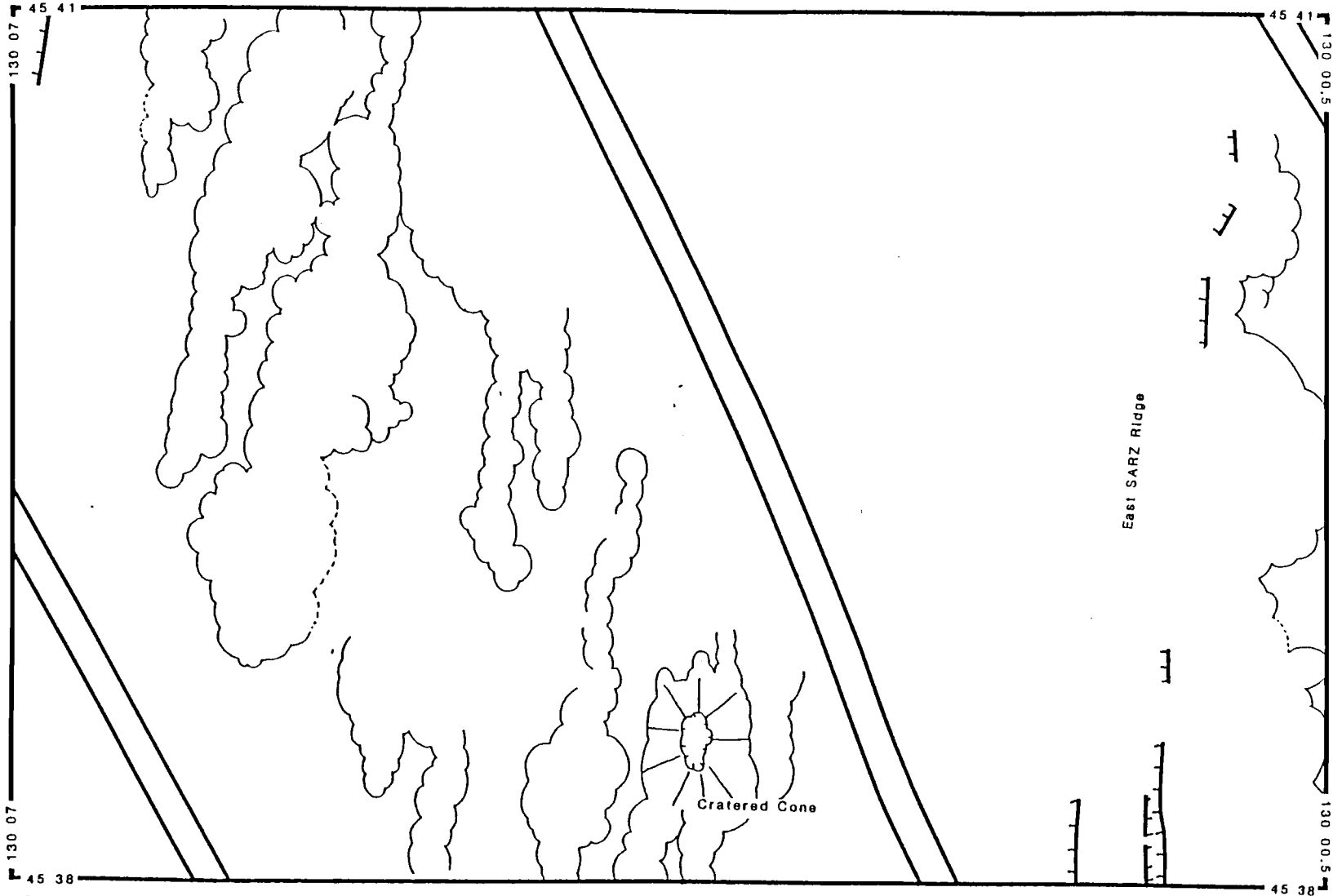
45 41
130 07
130 00.5
East SARZ Ridge
Cratered Cone
130 07
45 38
130 00.5
45 38

Figure 25 b.

45 41
130 07
West SARZ Ridge
Middle SARZ Ridge
East SARZ Ridge
130 00.5
45 38

Figure 25 c.

Figure 26. Imagery of the south rift zone of Axial volcano, see Figure 17 for location. A) Sidescan mosaic, high backscatter is represented by light shades. B) Geological interpretation. Symbolism is consistent with that in Figure 19. C) SeaBeam bathymetry, 10 m contour interval. The convoluted area near 45°36.25'N/130°05.75'W is an artifact of the contouring program.

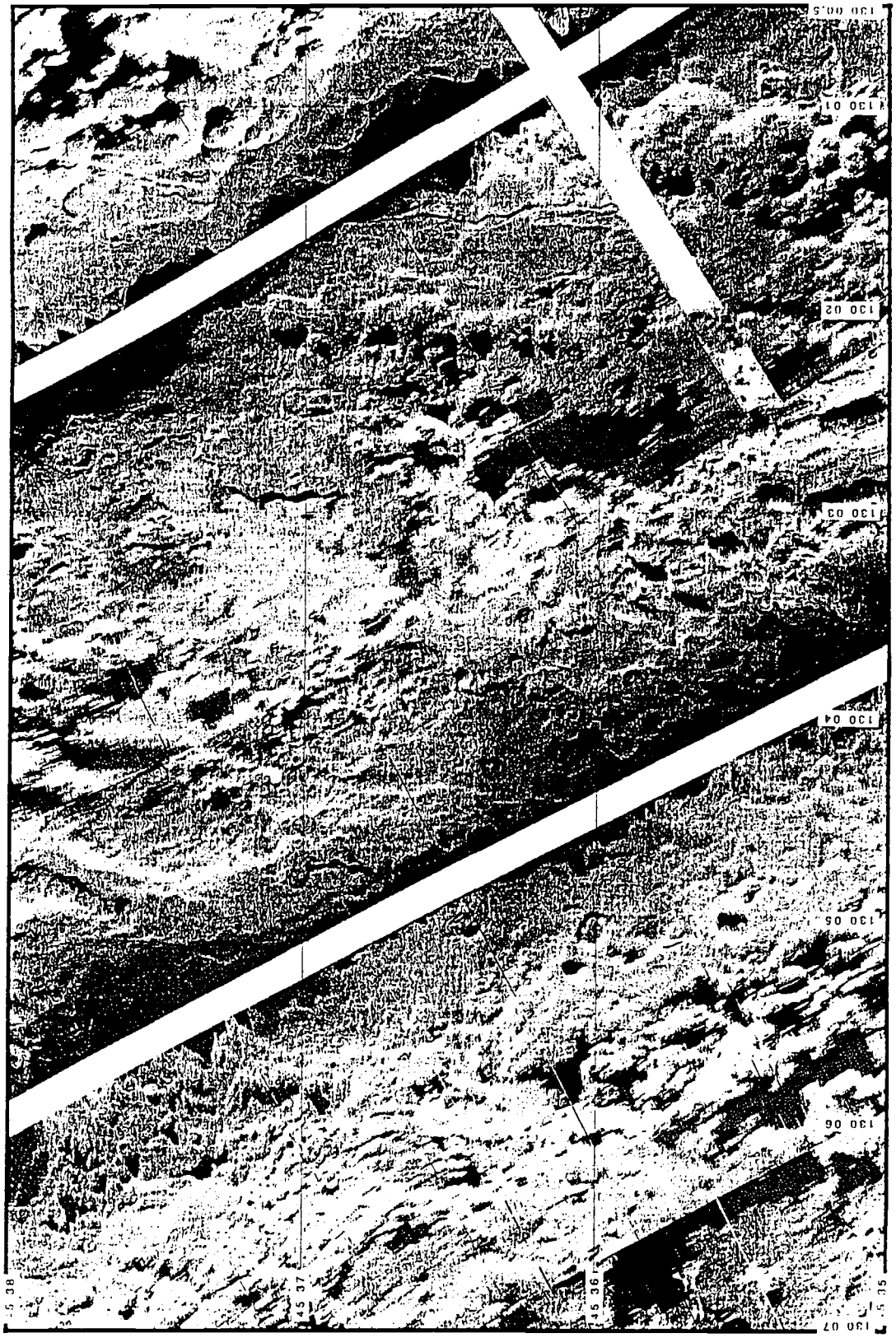
130 00.5
130 01
130 02
130 03
130 04
130 05
130 06
130 07
45 38
45 37
45 36
45 35

Figure 26 a.

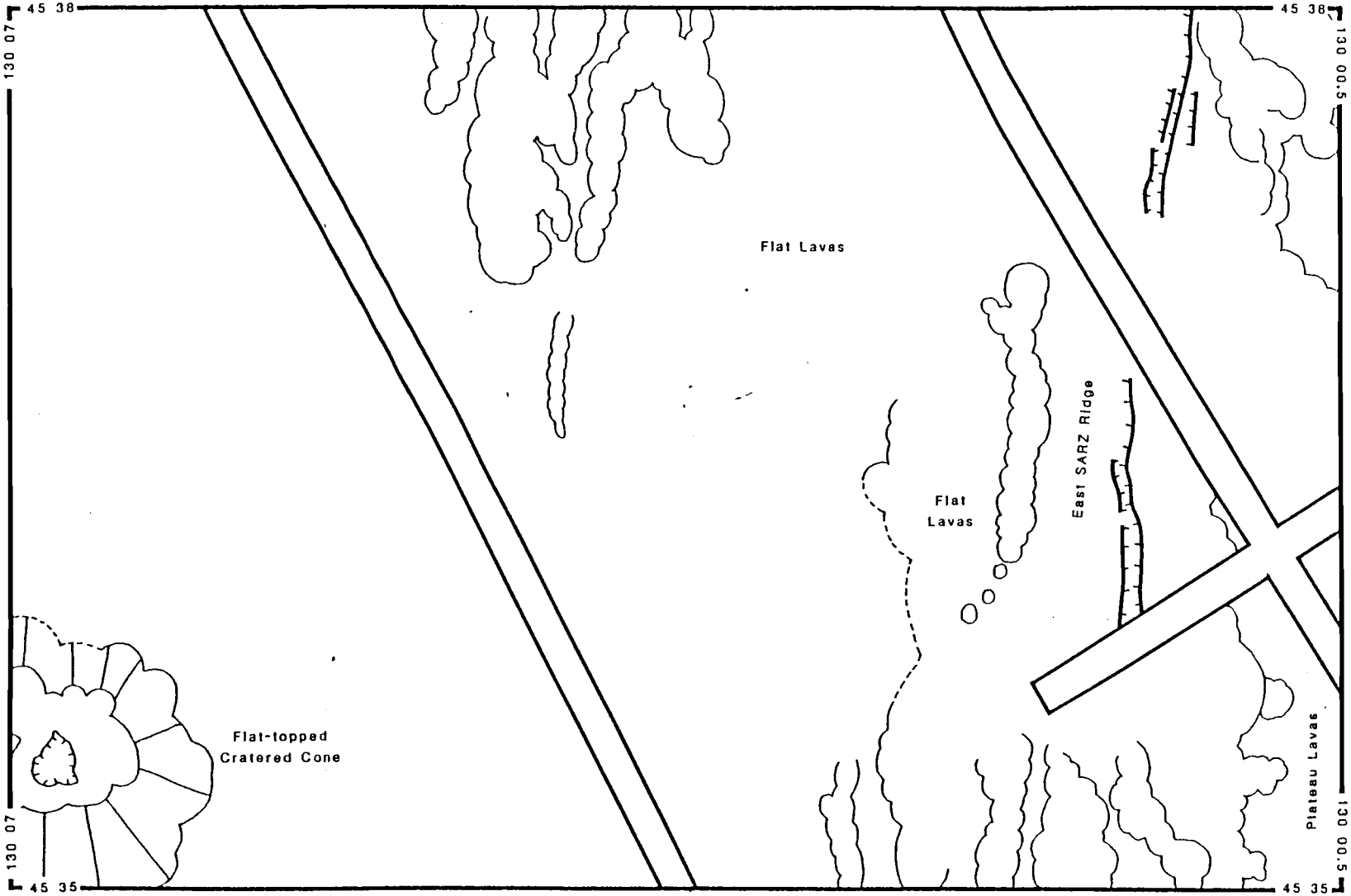
45 38
130 07
Flat Lavas
Flat
Lavas
East SARZ Ridge
Flat-topped
Cratered Cone
Plateau Lavas
130 00.5
45 35

Figure 26 b.

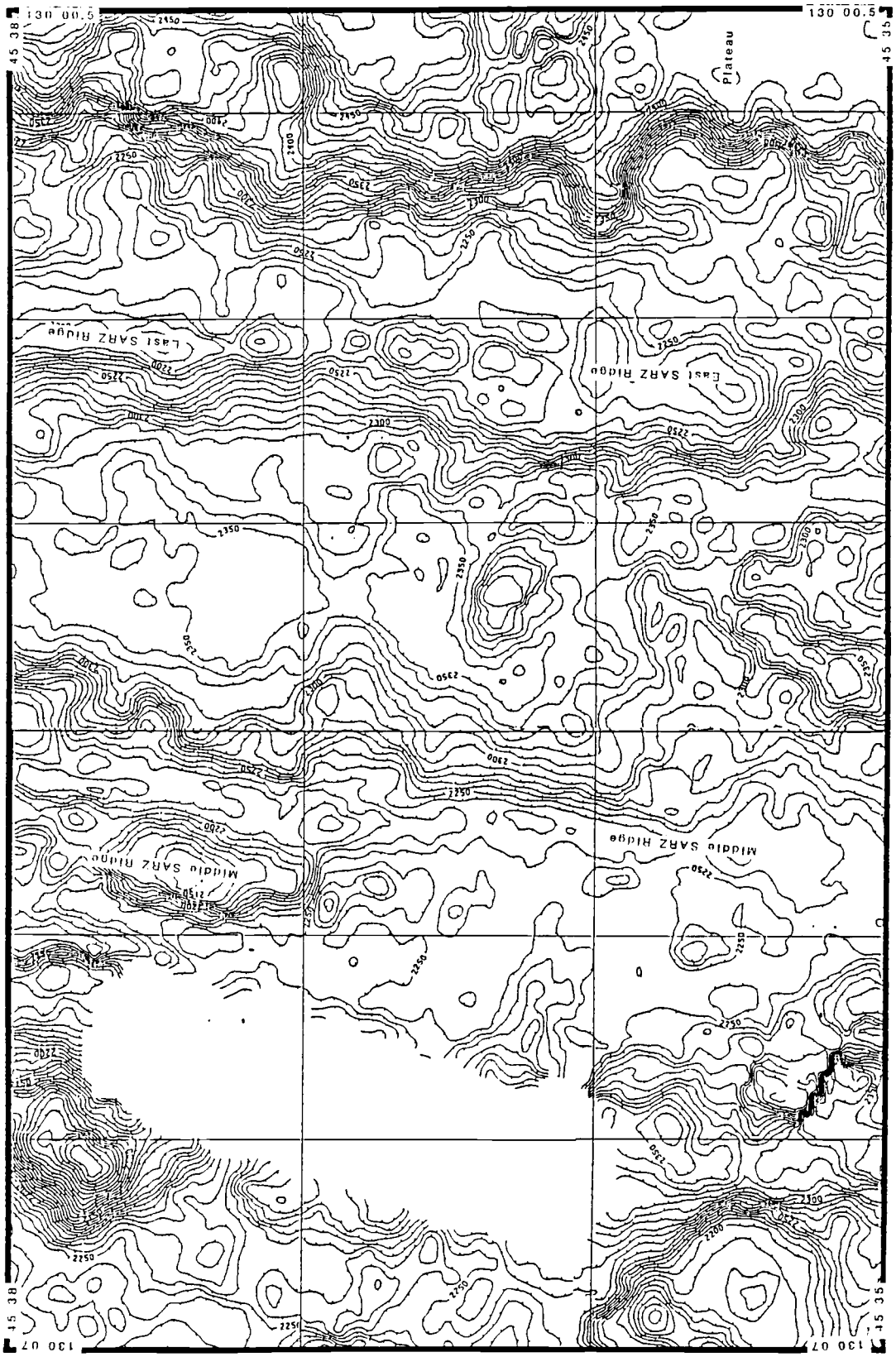
130 00.5
45 38
45 35
130 07
Plateau
East SARZ Ridge
Middle SARZ Ridge
Last SARZ Ridge

Figure 26 c.

Figure 27. Imagery of the south rift zone of Axial volcano, see Figure 17 for location. A) Sidescan mosaic, high backscatter is represented by light shades. B) Geological interpretation. Symbolism is consistent with that in Figure 19. C) SeaBeam bathymetry, 10 m contour interval.

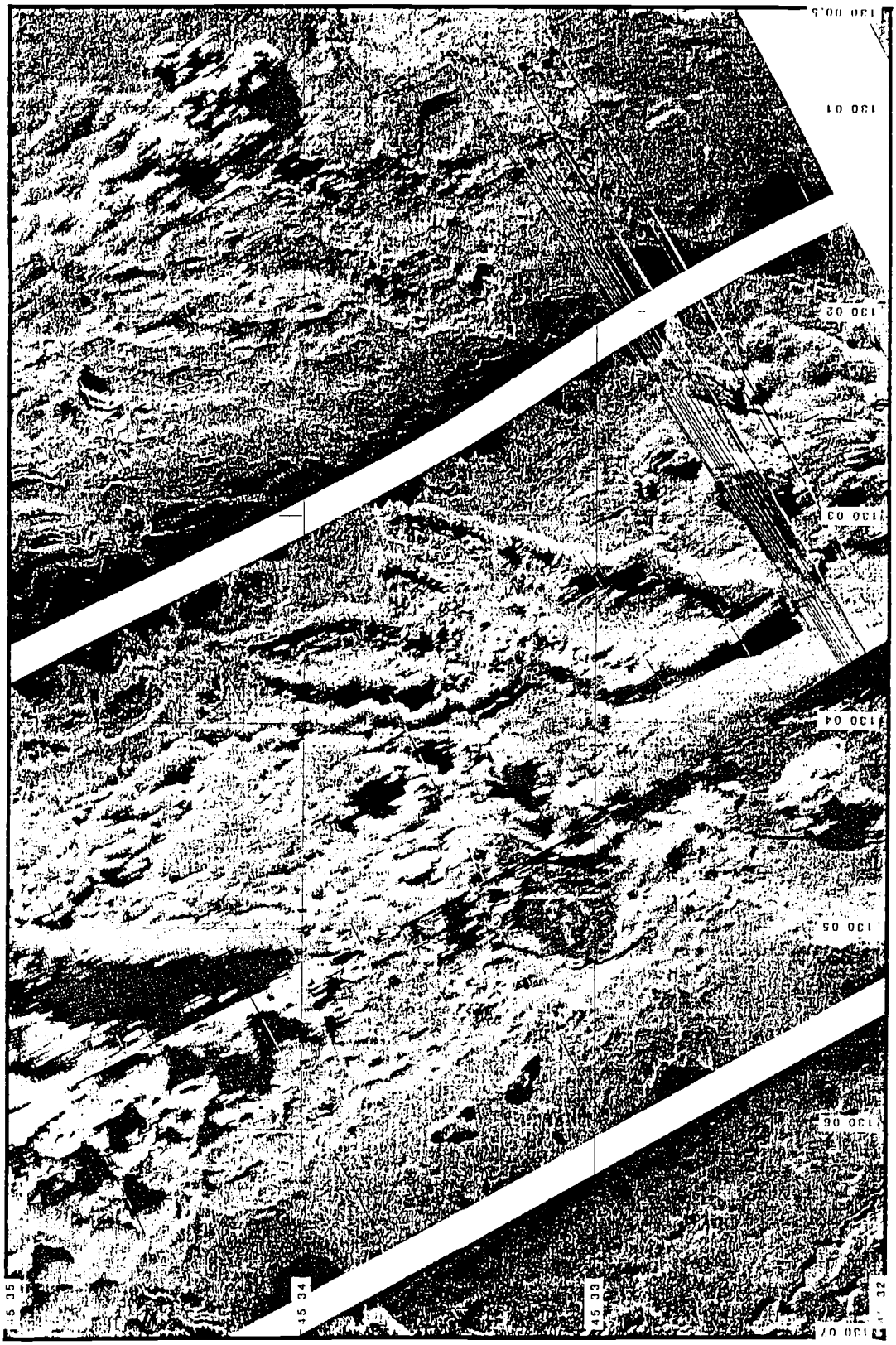

Figure 27 a.

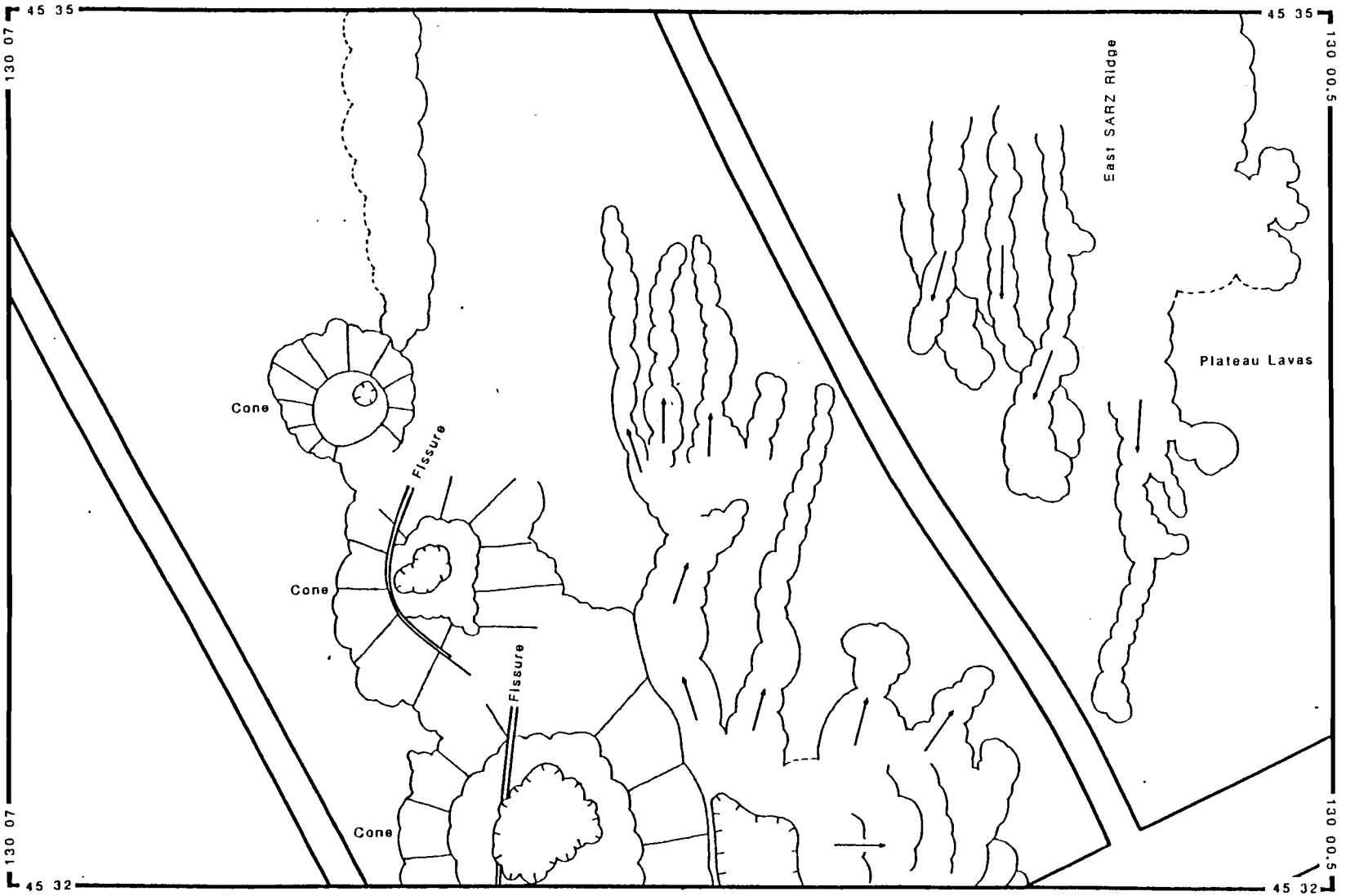
45 35
130 07
45 35
130 00.5
East SARZ Ridge
Plateau Lavas
Cone
Fissure
Cone
Fissure
Cone
130 07
45 32
130 00.5
45 32

Figure 27 b.


45 35
130 00.5
Miguia SAHZ Ridge
Enel SAñZ Ridge
Plateau
Plateau
Plateau
Cone
Cone
Cone
Crater
45 32
130 07

Figure 27 c.

rows of aligned, coalesced cones which can be traced discontinuously from 45°47'N at the top of Figure 23a to 45°36'N on Figure 26a. The rows of aligned cones are not evident in areas near large volcanic cones, either because they lie within the acoustic shadow of the larger structures (as appears to be the case near 45°45'N/130°02'W in Figure 23), or because the ridges are buried beneath lavas associated with the cones (as at 45°41.4'N/130°03'W in Figure 24). In contrast to the sinuous trend of the ridge crests defined in the bathymetry, the structural fabric resolved in the sidescan imagery is remarkably linear.

The surface of the SARZ region near the west and middle ridges displays a variety of morphologies characteristic of volcanic terrain. In addition to the rows of coalesced cones, several circular constructional features are present along the crests and flanks of the ridges. Two such structures appear on Figure 23a, one near 45°45'N/130°01.3'W and one at 45°45.8'N/130°01.2'W, and another appears on Figure 24a at 45°42.4'N/130°04.7'W. The flanks of the major and subsidiary ridges within the SARZ region appear scalloped, and lobate structures extend away from the bases of many of the volcanic ridges and cones. Some of the topographic highs display summit craters, for example the cratered cone centered around 45°38.5'N/130°03.5'W. Near 45°42.7'N/130°04.7'W, flat-lying lavas have filled a valley, and are surrounded by two linear ridges and a small volcanic cone. All of these features are indicative of volcanic terrain.

The distal southern ends of the west and middle ridges are populated by numerous volcanic cones, and south of 45°34'N volcanic cones dominate the topography within the SARZ (Figure 17). In general, the smaller cones in this region retain an elongate shape (in plan view) oriented parallel to the rift axis, and appear roughly conical in profile across their long axes. Volcanic ridges and rows of small cones are aligned along the trend of the rift axis also, suggesting that volcanism here is related to SARZ volcanism. Larger cones become more abundant towards the south, display circular morphologies in plan view, and often have flat tops and summit craters. One such flat-topped, cratered cone is visible near 45°35.5'N/130°06.8'W (Figure 26c). This cone is steep-sided, and contains a crater on the flat southeastern half of its summit. The flat summit area displays high backscatter, and the crater is evident in the sidescan imagery as a small negative-relief structure (Figure 26a).

A row of three large round flat-topped cones is visible farther south, between 45°'34'N/130°05.5'W and 45°32'N/130°04'W (Figure 27c). Of these three structures, the southernmost cone displays the most vertical relief and contains the

largest summit crater; the northernmost cone displays the least relief and the smallest crater. On the sidescan imagery (Figure 27a), the craters on each of the cones appear as negative-relief structures within the planar summit regions. The crater on the southern cone appears to be a composite of several small craters, as indicated by the scalloped crater rim. A series of sinuous ridges radiate away from a point below the eastern flank of the southern cone; these structures may represent lava tubes or channels that formed as the result of flank eruptions near the base of the cone. Flank eruptions have been inferred to occur on other small seafloor volcanoes, and have been proposed as a mechanism for summit collapse leading to crater formation (Fornari et al., 1984; Fornari et al., 1985); this process may account for the summit craters evident on the cones in this region as well.

Fault scarps are conspicuously absent within the high-backscatter SARZ region, both in the north where volcanic ridges dominate the topography, and in the south where volcanic cones are more prevalent. Although a few fissures are evident (for instance, near 45°46.8'N/130°04.75'W and 45°44.75'N/130°03'W on Figure 23, and near 45°32.3'N/130°04.5'W on Figure 27), they occur along the summits of major constructional features, and are probably related to eruptive rather than tectonic processes.

The contact between the high-backscatter lavas of the SARZ and the low-backscatter seafloor to the west is apparent near 45°44.5'N/130°06'W (Figure 23a). The low backscatter intensities observed over the seafloor to the west are attributed to the presence of sediment, which implies that the low-backscatter areas are older than the high-backscatter SARZ lavas. West of the contact, a series of west-facing, small-offset fault scarps etch the surface of the low-backscatter seafloor. The strikes of the faults vary somewhat, but are essentially oriented N00°E. The easternmost faults, which parallel the 130°06'W line of longitude, are locally overlain by the high-backscatter lavas of the west ridge of the SARZ. Lobate, constructional volcanic features in the field of high-backscatter lavas north of the older seafloor are aligned parallel to the trend of the faults. A 20 m ridge, expressed in the bathymetry between 45°47'N/130°06.4'W and 45°46'N/130°06.6'W (Figure 23c), coincides with the position of a row of high-backscatter, lobate, positive-relief structures evident in the sidescan imagery (Figure 23a). A N00°E-trending fault extends southwards from the southern tip of these aligned volcanic structures. Farther south along this fault, near 45°45.2'N/130°06.7'W, the fault is overlain by lavas that display backscatter intensities similar to the lavas farther north. These lavas are completely isolated within the low-backscatter area, and cannot be traced to the

SARZ lavas to the north or east. These lavas evidently erupted along the fault, and, given their similarity and alignment with the lavas that compose the volcanic ridge to the north, are probably associated with SARZ volcanism.

Several lines of evidence suggest that the high-backscatter SARZ lavas in this region (Figure 23) may have erupted along preexisting faults that have not accommodated displacement after the eruption of the lavas. None of the high-backscatter lavas in the northern part of Figure 23 are cut by faults, indicating that tectonic activity has not disrupted the volcanic surface here since the lavas erupted. The correlation between the strike of the volcanic ridge located between 45°47'N/130°06.4'W and 45°46'N/130°06.6'W with the strike of the fault that extends from the southern tip of the ridge suggests that the lavas that compose the ridge erupted from the northern continuation of the fault, and buried it. This interpretation is also supported by the presence of high-backscatter lavas, which appear similar to the SARZ lavas, that erupted along this fault within the low-backscatter region. Several other volcanic ridges are evident within the SARZ area east of the contact between the low- and high-backscatter regions. These ridges are also oriented parallel to the strike of the faults within the older, low-backscatter seafloor. One such ridge, evident in the bathymetry between 45°45.8'N/130°04.8'W and 44°44'N/130°05.2'W (Figure 23c), appears in the sidescan imagery as a series of coalesced cones and bulbous positive-relief features (Figure 23a). By analogy with the ridge located between 45°47'N/130°06.4'W and 45°46'N/130°06.6'W, the lavas that compose this ridge are inferred to have erupted along a preexisting fault, and the original orientation of the fault influenced the orientation of the volcanic ridge. Extrapolated across the entire SARZ edifice, the orientations of linear volcanic features, such as the numerous rows of coalesced cones, may reflect the orientation of preexisting faults that acted as conduits for SARZ magmas and controlled the emplacement of the lavas that constructed the rift zone.

The east ridge of the SARZ is similar to the west and middle ridges in the respect that it displays a volcanic surface morphology, and appears to be related to volcanism associated with Axial volcano's south rift zone. The crest of the east ridge diverges from the middle ridge near 45°43'N/130°01'W, and trends S00°W to about 45°34'N (Figure 2). In general, the crest of the ridge increases in depth towards the south. Crestal volcanic structures, such as the row of small cones between 45°37'N/130°02'W and 45°36'N/130°02'W, are aligned parallel to the axis of the ridge (Figure 26). The distal end of the ridge is marked by several low-relief, sinuous constructional features near 45°34'N/130°02'W that meander towards the

south (Figure 27a). The ridge's east flank displays several large lobate structures near 45°34.3'N/130°01'W (Figure 27) and 45°35.8'N/130°01'W (Figure 26) that protrude onto the planar surface of the plateau to the east. Flat-lying, intermediate-backscatter lavas occur along the base of the western flank of the east ridge around 45°37'N/130°02.5'W, and planar lavas occupy the interstices between rows of aligned cones along the crest of the ridge between 45°37'N/130°02.5'W and 45°36'N/130°02.5'W (Figure 26).

North of 45°41'N, the crest of the east ridge is not as distinctly expressed in the bathymetry as it is farther south, due to its superposition upon the shoaling southern flank of the Axial volcanic edifice. The crest of the ridge is located on a flat shelf (roughly defined by the 2200 m isobath) that juts outward from the east side of the middle SARZ ridge between 45°41'N/130°03'W to 45°45'N/130°02'W, and is flanked to the east by South Helium Basin (Figure 24c). The seafloor over the shelf displays homogeneous high backscatter, and, except where lobate structures protrude from the middle ridge at 45°43.4'N/130°01.6'W, lacks major positive-relief constructional features.

In contrast to the west and middle ridges, the east ridge displays a series of small-offset faults that extend along its summit. Scarps can be traced northwards on the sidescan imagery from 45°36'N/130°01.75'W (Figure 26a) to 45°46.75'N/129°59.4'W (Figure 29a). These scarps are not apparent in the bathymetry, although the local contours run roughly parallel to the trend of the faults. Most of the faults face towards the west, although in some areas eastward-facing faults are also evident, forming narrow, shallow grabens (e.g., near 45°36'N/130°01.5 on Figure 26 and 45°42.6'N/130°01'W on Figure 24). The faults crosscut positive-relief volcanic structures on the eastern flank of the east ridge near 45°37.5'N/130°01.5'W (Figure 26) and 45°38.25'N/130°01.3'W (Figure 25), and displace featureless, homogeneous-backscatter lavas north of 45°41'N (for example near 45°43'N/130°00.75'W on Figure 24).

The general appearance of the east SARZ ridge, as expressed in the regional bathymetry (Figure 2), differs from the west and middle SARZ ridges. The east ridge is oriented roughly N00°E, which is oblique to the N10°E trend of the west and middle SARZ ridges. The crest of the east ridge is flat, and is not marked by massive constructional volcanic features. The southern tip of the east ridge does not terminate in a field of volcanic cones, as the west and middle ridges do; instead, the east ridge is bounded to the south by flat-lying, intermediate-backscatter lavas.

The east SARZ ridge is separated from the axial valley of the northern Vance segment by a wedge-shaped parcel of seafloor that is widest at 45°40'N and tapers to a point near 45°31'N/130°01'W (Figure 2). The northern part of the wedge-shaped area contains a depression (centered around 45°37.5'N/130°00'W), and the southern area is composed of a triangular-shaped plateau; a 100 m constructional scarp separates these two regions (Figure 21c). Faulting is not evident within the depression or on the plateau. High-backscatter lavas cover the floor of the depression, and lobate volcanic structures can be traced downhill into the depression from the plateau to the south (near 45°37.5'N/129°59'W in Figure 21), and from the east SARZ ridge to the west (around 45°38'N/130°00'W in Figures 21 and 22). The plateau is blanketed by flat-lying, intermediate-backscatter lavas that are pockmarked by numerous negative-relief structures (Figures 20 and 21). The interiors of the negative-relief structures display higher backscatter than the surrounding flat-lying lavas. The contact between the flat-lying lavas with the bulbous volcanic structures that protrude from the east SARZ ridge is distinct, although it is not evident whether the SARZ lavas overlie the flat-lying lavas, or whether the plateau lavas onlap the bulbous structures. The plateau lavas are considered to be related to the MLU lavas within the axial valley due to 1) their similar backscatter characteristics, 2) the continuity of the backscatter pattern of the plateau lavas over the axial valley's west wall, and 3) the presence of plateau lavas overlying fault scarps along the west valley wall. Although an unequivocal source for these lavas cannot be resolved from the sidescan imagery, they must have erupted west of the Vance segment's axial valley. It is conceivable, however, that these lavas could have erupted from the east SARZ ridge, since the ridge is a major constructional volcanic feature associated with Axial volcano's south rift zone.

South Helium Basin

South Helium Basin is a semi-rectangular embayment in the southeast flank of Axial volcano, situated east of the SARZ and north of the northern terminus of the Vance spreading segment (Figure 2). The long axis of the basin strikes roughly N25°E. In general, the backscatter intensity within the basin decreases towards the south and east, away from the shoalest part of Axial volcano (plate 1). The basin is pervasively faulted, and displays two outstanding structures: a 200 m, N25°E-

trending ridge that defines the basin's eastern side, and a 100 m ridge that extends up the middle of the basin.

The eastern ridge of South Helium Basin is located between 45°45'N/129°55'W and 45°40'N/129°58'W (Figure 17). The east and west flanks of the ridge are bounded by faults that are oriented parallel to the strike of the ridge (Figure 28). At its crest, the ridge displays low backscatter, considered to represent sediment cover and hence a relatively old age for the seafloor there. The lack of volcanic structures along the flanks of the ridge indicate that the vertical relief of this ridge is due to tectonic processes, rather than constructional volcanism.

The middle ridge within South Helium Basin, evident in the detailed bathymetry of Figure 28c, extends from 45°41'N/129°59.5'W to 45°44'N/129°57.5'W (Figure 28). The summit of the middle ridge displays intermediate backscatter, and lobate positive-relief structures are evident along the crest and eastern flank of the ridge, near 45°42.75'N/129°58.5'W and 45°41.5'N/129°58.5'W. The area between the two ridges displays intermediate backscatter, and is dissected by numerous faults, which, on average, strike N25°E. Near 45°41.5'N/129°58.5'W, several of the faults near the base of the middle ridge's east flank are overlain by intermediate-backscatter, lobate volcanic features. The local topography slopes towards the east here, which suggests that the lavas that buried the faults originated near the crest of the middle ridge. The west side of the ridge is bounded by a curvilinear westward-facing fault scarp that accommodates up to 70 m of relief. This scarp can be traced from 45°40.9'N/129°59.9'W (Figure 22a) to 45°44.5'N/129°58'W (Figure 29a); the fault displays maximum vertical relief near its midpoint, and progressively less relief to the north and south.

A graben and horst lie to the west of the middle ridge, between 45°42'N/129°59.75'W and 45°43'N/129°59'W (Figure 28). The top of the horst is flat, and exhibits low backscatter. Much of the graben between the horst and the middle ridge is cast in acoustic shadow; however, the illuminated area reveals that the interior of the graben exhibits low to intermediate backscatter, and is cut by several small-offset faults. West of these structures, the seafloor slopes upward towards the east SARZ ridge. High-backscatter lavas blanket this slope, and abut the base of the fault scarp on the west side of the middle ridge near 45°41.75'N/129°59.75'W.

The surface of the northern part of South Helium Basin (shown in Figure 29) exhibits a predominantly volcanic morphology, although the faults of the basin's east ridge, and the faults associated with the east SARZ ridge, are evident in this

Figure 28. Imagery of South Helium Basin, see Figure 17 for location. A) Sidescan mosaic, high backscatter is represented by light shades. B) Geological interpretation. Symbolism is consistent with that in Figure 19. C) SeaBeam bathymetry, 10 m contour interval.

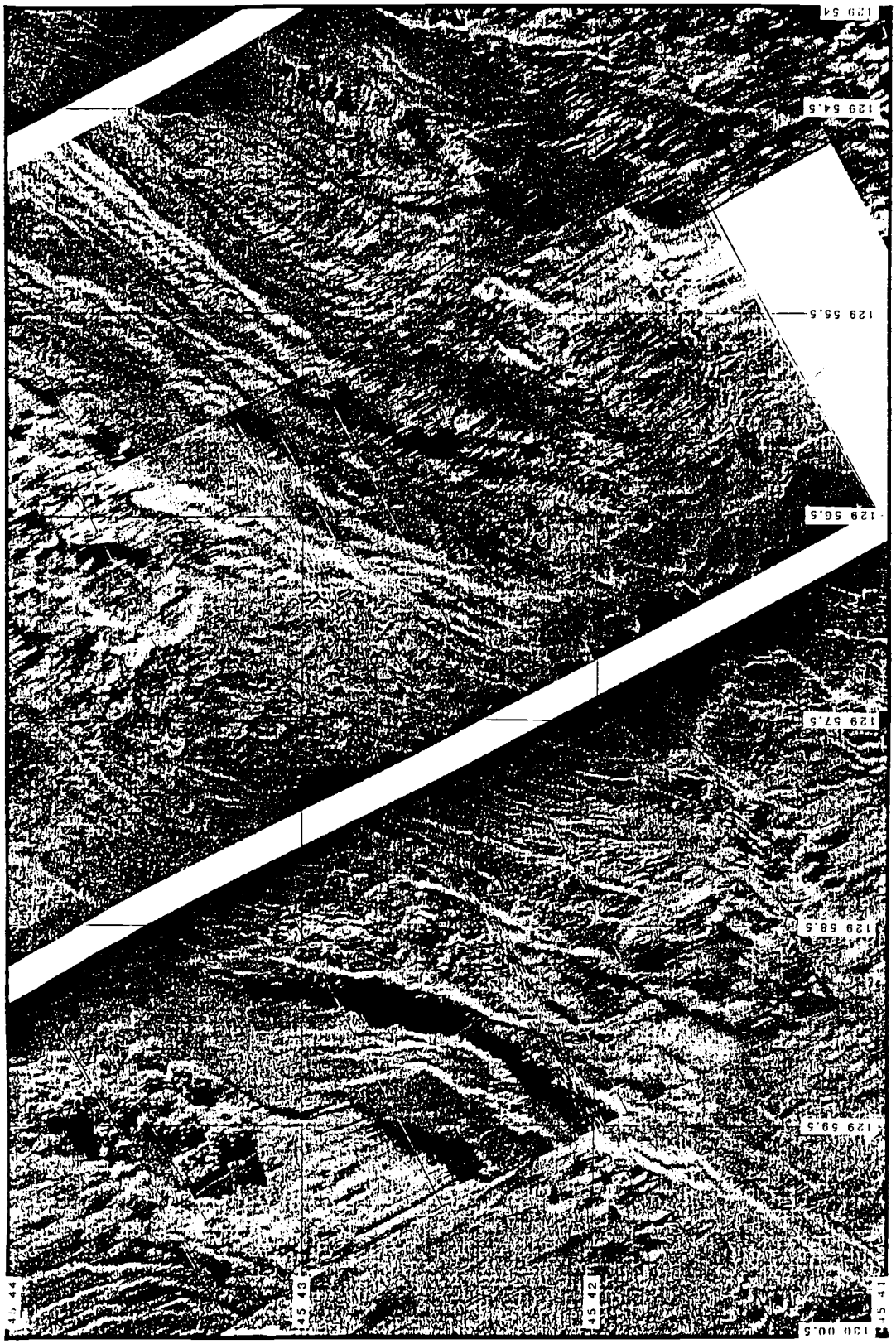
129 54
129 54.5
129 55.5
129 56.5
129 57.5
129 58.5
129 59.5
130 00.5
45 44
45 43
45 42
45 41

Figure 28 a.

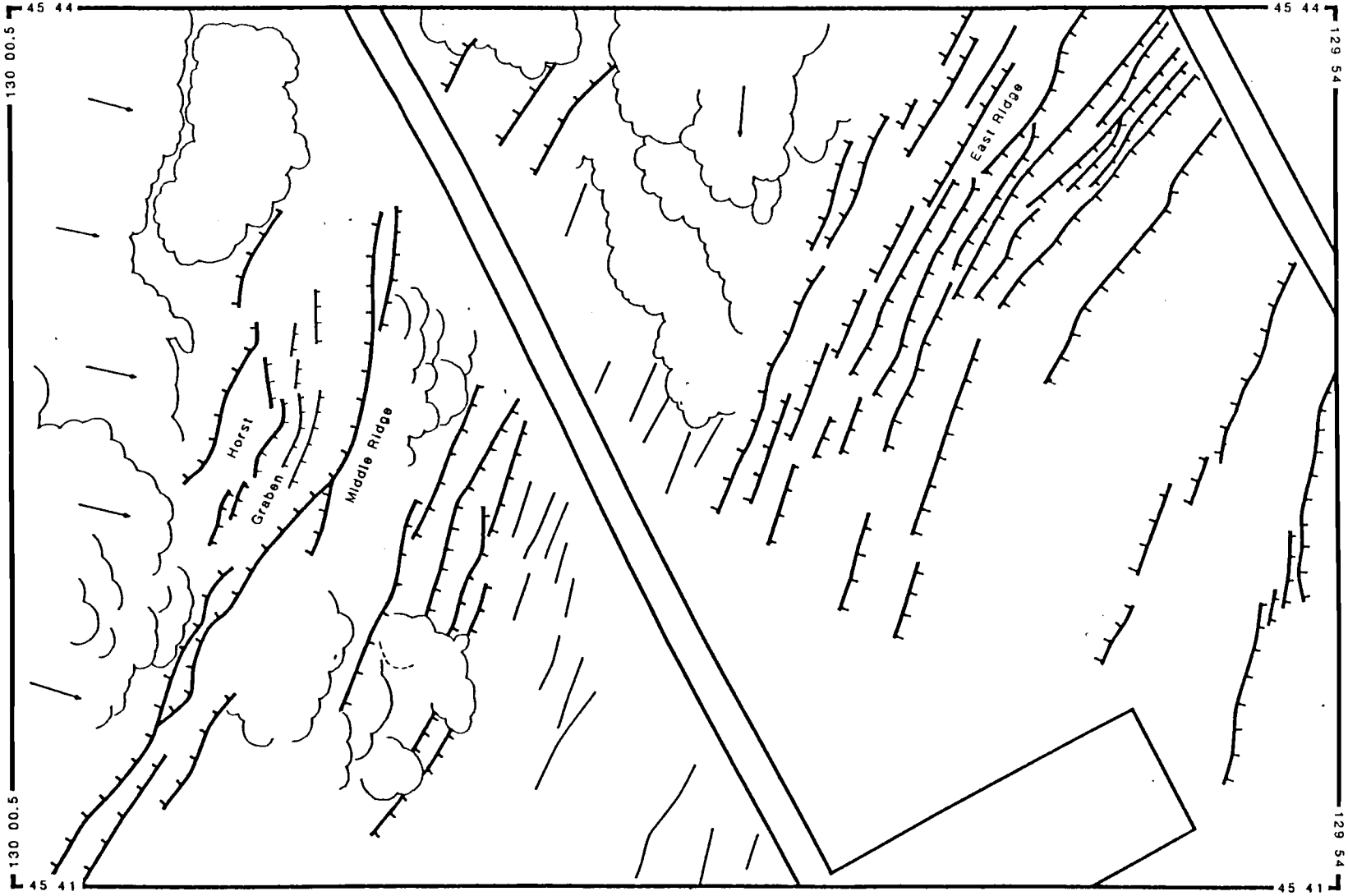
45 44
130 00.5
129 54
Horst
Graben
Middle Ridge
East Ridge
45 41

Figure 28 b.

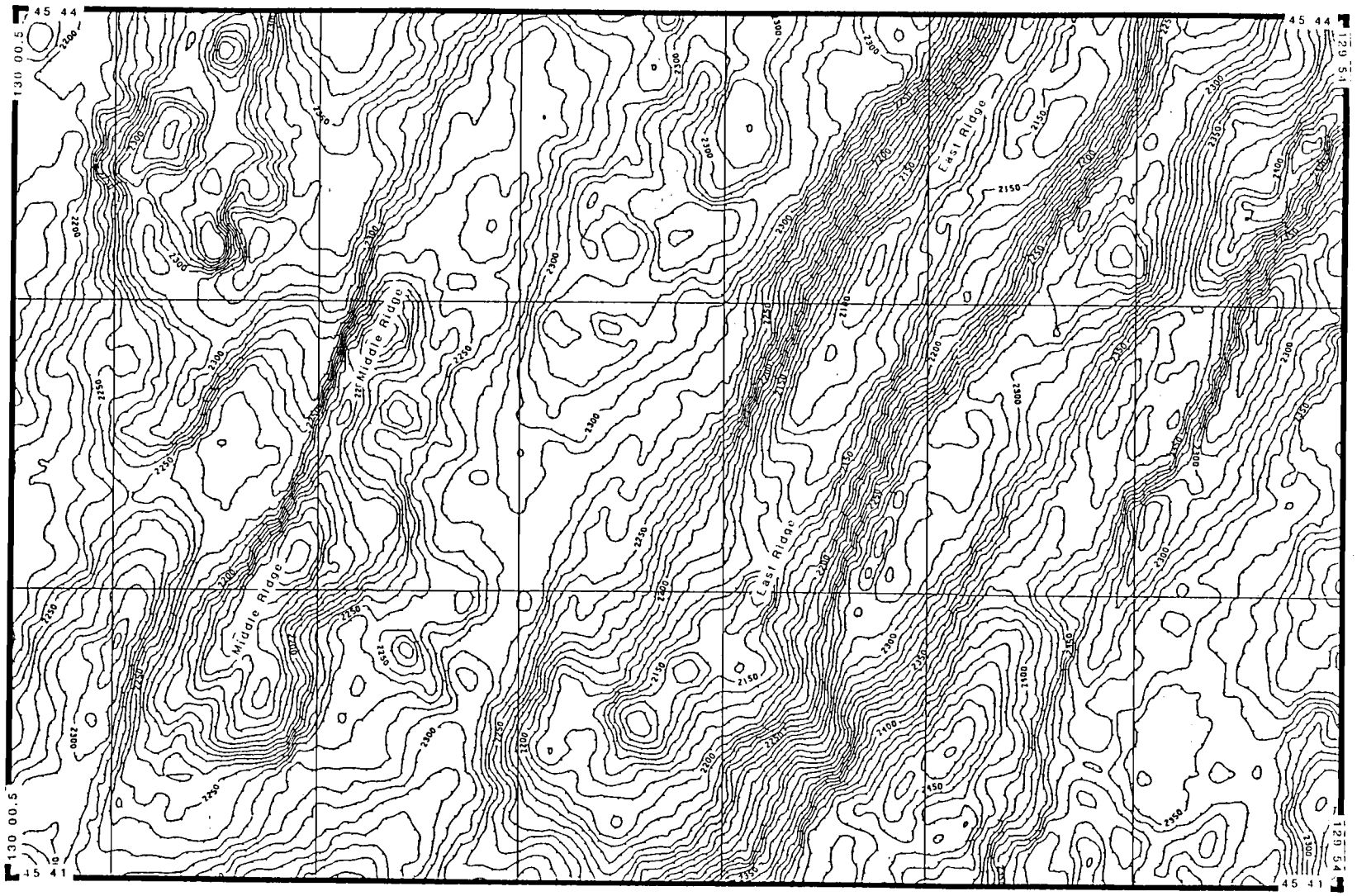

Figure 28 c.

Figure 29. Imagery of South Helium Basin, see Figure 17 for location. A) Sidescan mosaic, high backscatter is represented by light shades. B) Geological interpretation. Symbolism is consistent with that in Figure 19. C) SeaBeam bathymetry, 10 m contour interval.

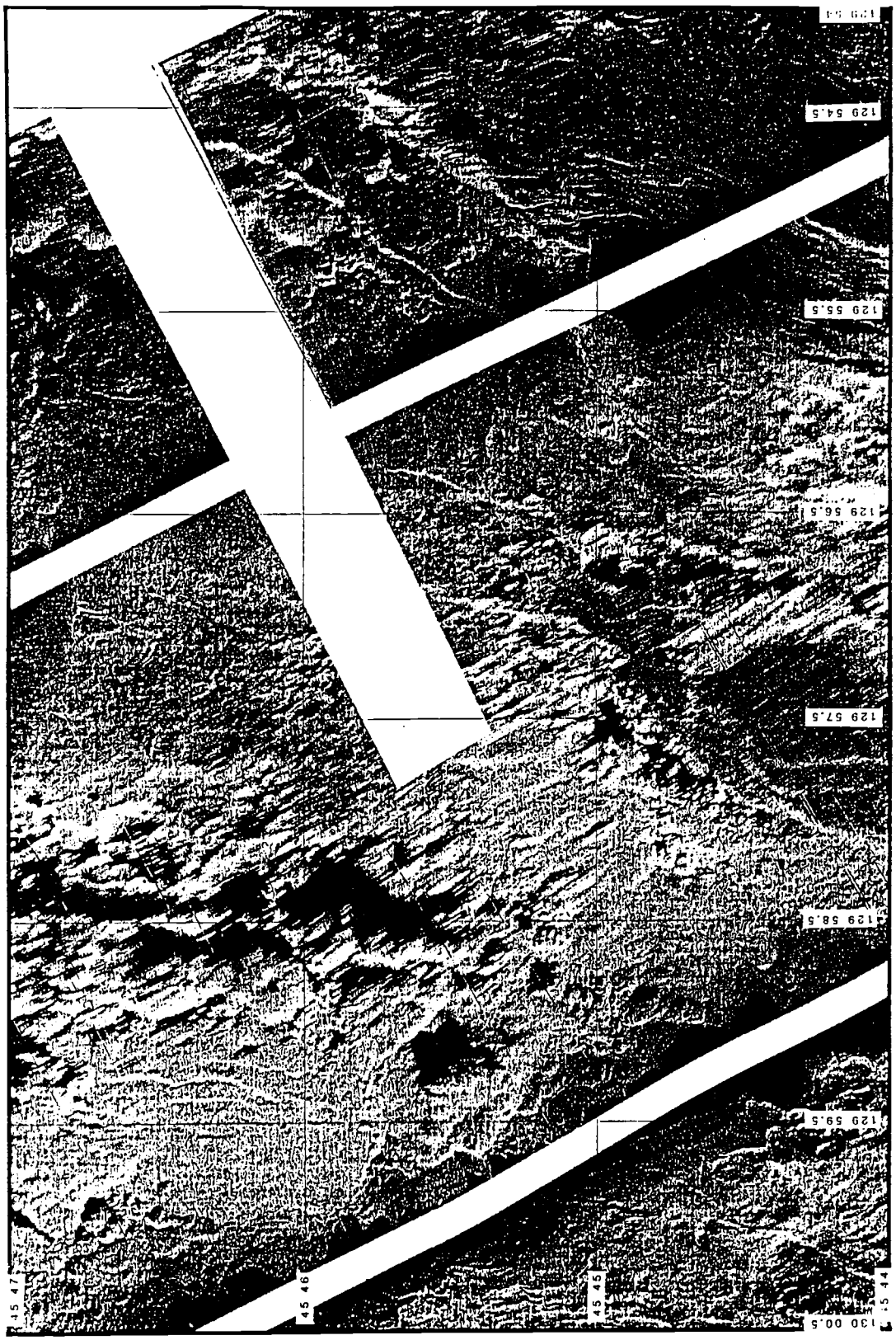
129 54.5
129 55.5
129 56.5
129 57.5
129 58.5
129 59.5
130 00.5
45 47
45 46
45 45
45 44

Figure 29 a.

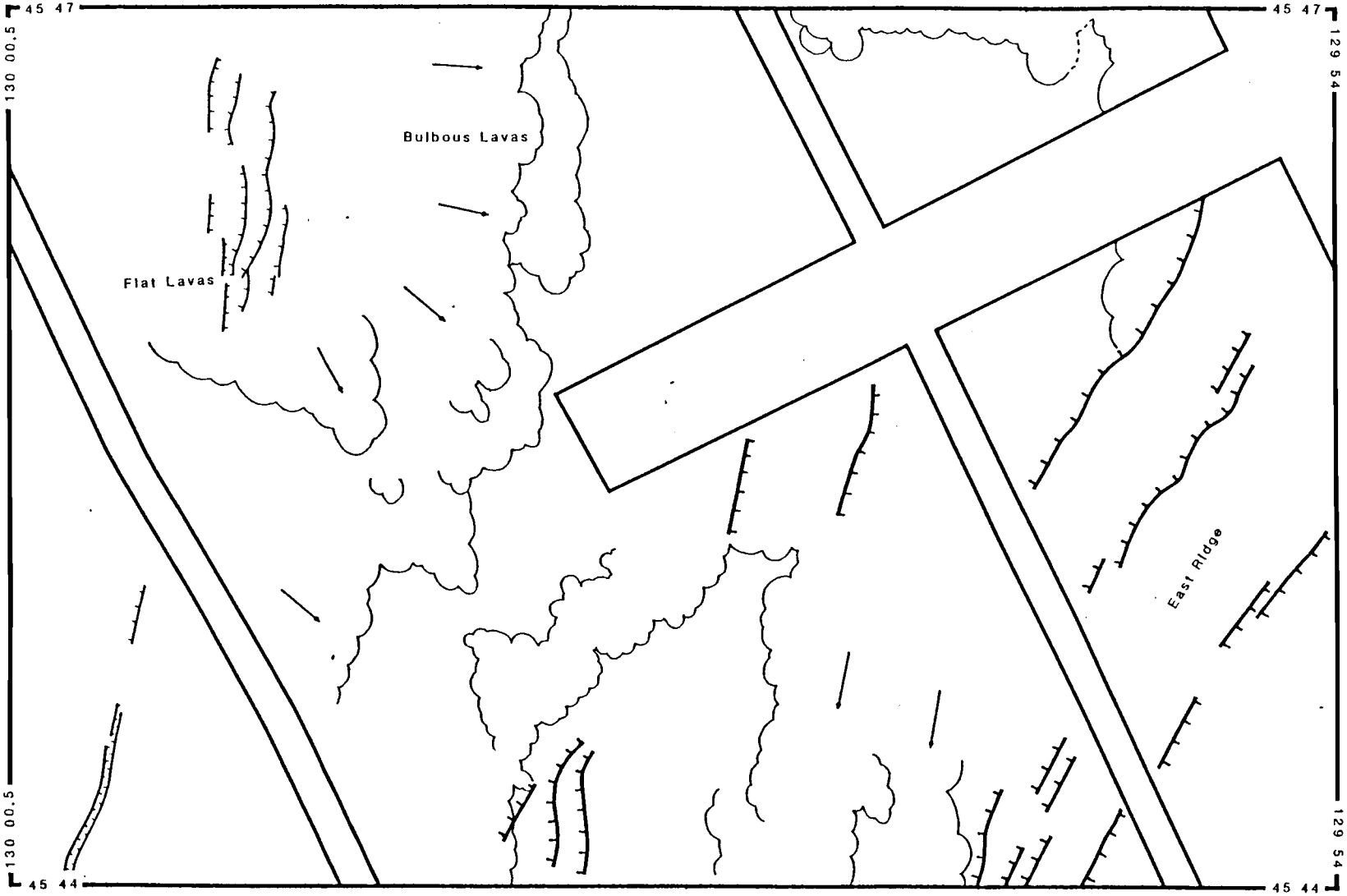

Figure 29 b.

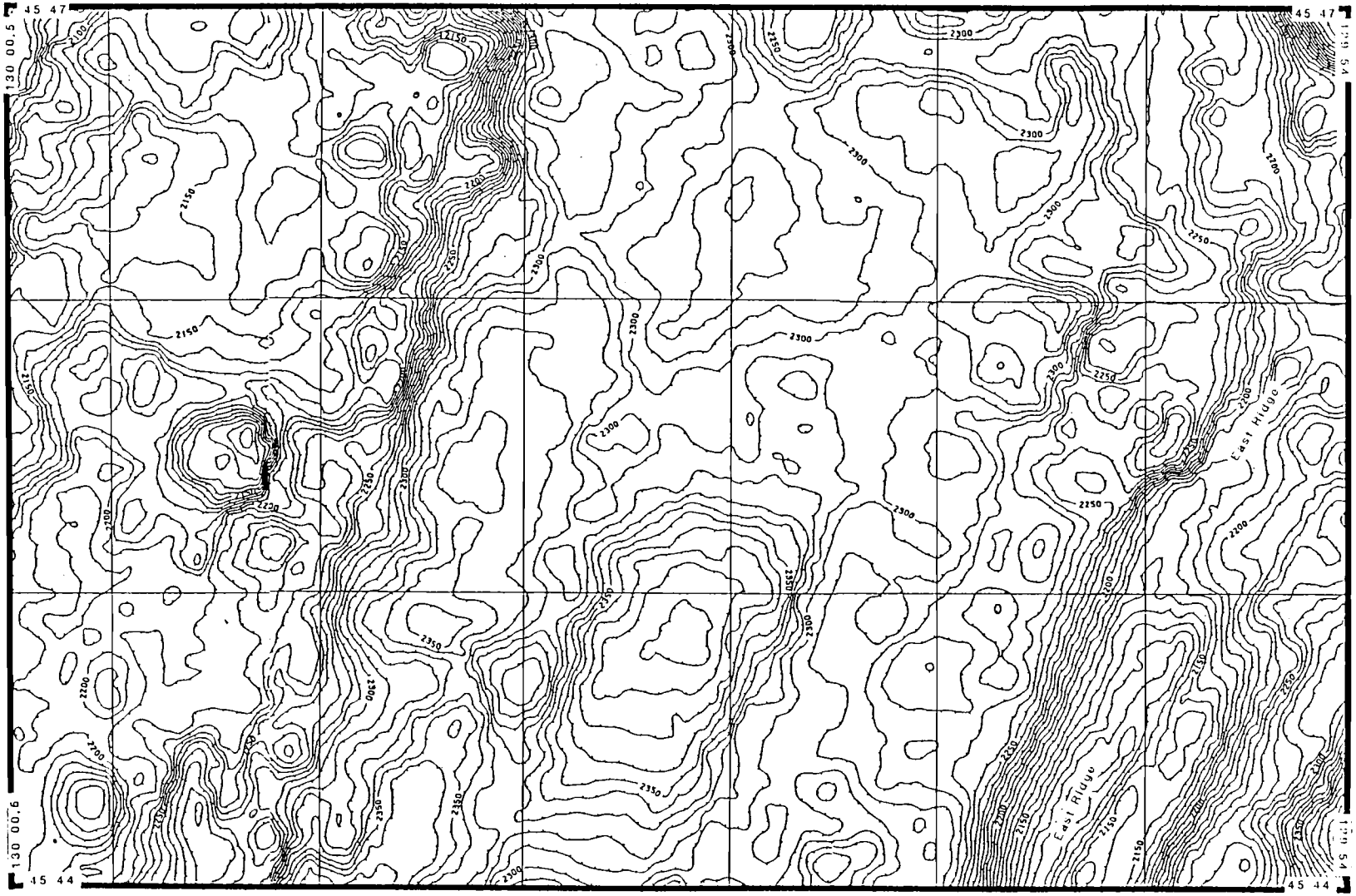

Figure 29 c.

region. High-backscatter, flat-lying lavas occupy the area around 45°46.5'N/129°59.5'W; these lavas are crosscut by the faults along the crest of the east SARZ ridge. The northern ends of the faults are buried beneath bulbous lavas at 45°46.75'N/129°58.4'W. The seafloor slopes down towards the south and east from these lavas, and a 150 m scarp, constructed from bulbous and lobate volcanic features, extends between 45°47'N/129°58'W and 45°45'N/129°58.5'W (Figure 29c). The surface of the basin east of this scarp is flat, and displays low backscatter (Figure 29a). The backscatter contrast between the upper and lower lavas is interpreted to represent a greater degree of sediment cover east of the volcanic scarp, indicating that the lavas near 45°46.5'N/129°59.5'W are younger than those to the east.

A low backscatter region occupies a topographic low centered around 45°44.5'N/129°57.5'W. The depression is bounded by a pair of volcanic ridges that extend southwards from the flat-lying, low-backscatter lavas to the north. The scarps that separate the floor of the depression from the crests of the ridges are composed of bulbous volcanic features. The low-backscatter area is inferred to be a sedimented region that is flanked by younger volcanics to the east, west, and north.

DISCUSSION

Based on the foregoing observations made from the sidescan imagery, several inferences may be made regarding the structures, timing of events, and geological processes that have shaped the southern flank of Axial volcano and the northern portion of the Vance segment. In the following section, the relative ages of various structures within the northern part of the Vance segment and within South Helium Basin are used to infer sequences of tectonic and volcanic events that have contributed to shape these two regions. Bathymetric data provide constraints for the absolute time frame of the relative ages of events. This section also discusses the location of the axis of Juan de Fuca spreading in the vicinity of Axial volcano.

Timing of Events and Implications for the Tectonic Evolution of the Northern Vance Spreading Segment

The structural relationships between the faults and lavas in and around the Vance segment's axial valley permit relative ages to be assigned to the various features there, from which a scenario for the tectonic and volcanic evolution of the area may be surmised. The oldest features evident in this area are the low-backscatter parcels of seafloor on top of the eastern and western marginal ridges, beyond the axial valley walls. The faults of the valley walls separate the high-backscatter surface of the axial valley from the low-backscatter surfaces of the crests of the EMR and WMR. Assuming that the high backscatter surface of the axial valley represents relatively barren (unsedimented) lavas, then the faulting along the valley walls must predate the formation of the surface of the valley floor, and the crestal regions of the WMR and EMR must be older than the fault.

Based on structural evidence, two different episodes of faulting can be resolved along the east valley wall. The two fault systems evident along the east valley wall between 45°27.5'N and 45°31'N (Figures 18 and 19) bound a fault block that is covered by lobate, constructional volcanic features. These lobate structures overlie older faults on the eastern side of the fault block near 45°29.2'N/129°57'2'W and 45°30.2'N/129°57'W (Figure 19), and are themselves faulted by a continuous fault that separates the west side of the block from the floor of the axial valley (Figures 18 and 19). The surface of the fault block displays backscatter that is intermediate in intensity relative to the high-backscatter axial valley floor and low-backscatter crest of the EMR.

From these observations, sequential volcanic and tectonic events in this area may be inferred. Displacement along the outermost fault is inferred to predate movement along the inner fault. The outer fault initially displaced the EMR above the valley floor, which isolated the EMR from rift valley volcanism and allowed pelagic sediments to accumulate atop the EMR without being covered by new volcanic material. Lavas subsequently erupted within the axial valley, which at that time included the seafloor that now occupies the fault block, and these lobate lavas buried much of the fault block and covered some of the older fault scarps to the east. After the emplacement of the lavas on the fault block, faulting occurred along the west side of the block, displacing the surface of the fault block above the floor of the axial valley. Finally, volcanism within the axial valley emplaced the high-backscatter lavas below the inner fault. This scenario suggests that the youngest lavas in the valley may overlie lavas associated with those that are now perched on the fault block.

An inherent assumption within this model is that lavas erupt within the axial valley, and not beyond the valley wall. Previous studies of the JDF spreading segments have shown that volcanism is generally confined to the axial valley (e.g., Kappel and Ryan, 1986; Barone and Ryan, 1988). Primary eruptive centers are typically located along medial structures within the axial valley, such as the cleft in the Cleft segment (USGS Juan de Fuca Study Group, 1986; Kappel and Normark, 1987) and the central ridge in the Vance segment (Embley et al., 1983; Kappel and Ryan, 1986). Sidescan sonar studies and seafloor photography surveys have consistently documented low backscatter, sedimented surfaces outboard of the axial valleys of the JDF ridge segments (Crane et al., 1985; Kappel and Ryan, 1986; USGS Juan de Fuca Study Group, 1986; Kappel and Normark, 1987; Barone and Ryan, 1988). The sidescan imagery over the northern part of the Vance segment in this study indicates that the central ridge is the most probable major source of lavas within the eastern half of the axial valley, given its topographic relief, constructional morphology, and the presence of lobate constructional forms which radiate eastwards from discrete topographic highs on the ridge. There is no evidence to suggest that recent volcanic activity has occurred beyond the east wall of the axial valley.

The fault that defines the west side of the fault block can be traced as a discrete scarp northwards to 45°31'N. North of this point the fault splays into several closely-spaced faults that define the western boundary of the EMR between 45°31' and 45°42'N. The along-strike continuity of the faults north and south of

45°31'N suggests that they are related. North of 45°31'N, the lower part of the tectonic scarp is abutted by lavas of the MLU. The MLU lavas are not crosscut by faults associated with the faults on the east wall of the axial valley. This fault system is considered to be associated with the tectonic activity that created the vertical relief between the western side of the EMR and the east side of the axial valley, and predates the emplacement of the MLU lavas.

The most recent volcanism within the axial valley postdates the faulting along the east valley wall. High-backscatter lavas within the axial valley abut the east valley wall at 45°30'N, 45°27.75'N, and 45°26.25'N. At least two episodes of volcanism are resolvable on the eastern valley floor: faulted, intermediate-backscatter lavas are overlain by undisturbed high-backscatter lavas near 45°26.1'N/129°59.6'W, indicating that the older lavas were deposited and faulted prior to the emplacement of the high-backscatter lavas which overlie the intermediate-backscatter lavas. The older lavas within this part of the valley may be related to the lavas on the fault block located near 45°27.5'N/129°58.5'W, as indicated by the proximity of these lavas to the fault block farther north, and the similarity between the backscatter intensities over each area. Lobate, constructional forms can be traced on the high backscatter lavas from the point where they dam against the east valley wall at 45°27.5'N/129°58.75'W uphill to the central ridge, suggesting that the central ridge acted as a source for these volcanics.

Faulting along the western side of the central ridge created the relief between the central ridge and the graben immediately to the west. The movement along these faults postdates the initial volcanism along the central ridge. This is indicated by the linear fault scarps that displace the volcanics on the central ridge near the topographic high at 45°28'N/130°00'W. The topographic high is constructed from voluminous lavas that probably would have completely buried the fault scarps had the bulk of the volcanism occurred after the faulting. Some of the fault scarps on the western flank of the central ridge are locally overlain by lavas, as seen near 45°27.5'N and 45°32.5'N, indicating that volcanic activity along the ridge continued to occur after the faults were formed. The faulting along the western side of the central ridge may have occurred over a short period of time, bracketed between episodes of volcanism along the crest of the central ridge, or alternatively, intermittent faulting and volcanism could have occurred throughout the later stages of the formation of the central ridge.

The faults on the western side of the graben crosscut volcanic features associated with central ridge lavas, but are also overlain by lavas that appear to have

originated on the central ridge. Therefore the most recent activity along this fault system occurred sometime during the constructional phase of the central ridge. Tectonic activity along the faults on the east and west sides of the graben is considered to have occurred during the same general time period, given the lack of evidence to further constrain the timing of the movement along one fault system relative to the other. The western side of the graben is overlain by lavas near 45°26'N. These lavas must postdate activity along the fault, although a minimum age for these lavas cannot be determined due to their lack of correlation with younger structures.

The plateau lavas, the MLU lavas, and the lavas that overlie the axial valley's west wall are considered to be related, and to have erupted during the same general period. All of these lavas display similar backscatter characteristics, and there is no evidence to suggest that significant hiatuses separate their emplacement. The lavas that overlie the west valley wall at 45°31'N, 45°32.6'N, and 45°34.5'N can all be traced uphill to the plateau, and these lavas appear to be contiguous with the MLU lavas. Each of these lavas overlies the low-backscatter seafloor on the WMR, the faults along the west valley wall, the faults along the east side of the graben, and the volcanics of the central ridge. MLU lavas abut the east valley wall, conform to the faulted terrain within the northern end of the axial valley, and overlie faults associated with the west valley wall near the terminus of the axial valley. The MLU lavas are not cut by faults associated with the east valley wall. All of the lavas that can be traced from the plateau into the axial valley are therefore inferred to be younger than the structures that predate the MLU lavas, as well as structures which they overlie themselves.

The N20°E-trending faults at the northern tip of the Vance segment appear to postdate the faults that constructed the west side of the EMR, as suggested by the crosscutting relationships evident near 45°39'N/129°55.5'W. Lavas of the MLU abut the bases of the N20°E-trending faults along the east margin of the axial valley near 45°38'N/129°56'N, and the MLU lavas are not faulted, suggesting that the N20°E-trending faults are older than the MLU lavas.

The youngest resolvable tectonic structures within the Vance segment are the faults which crosscut the MLU lavas. The alignment of the graben atop the MLU with the faults along the east side of the graben south of the MLU suggests that these fault systems may be related. If the tectonic activity that disrupted the surface of the MLU also caused displacement along the faults in the axial valley south of the MLU, then it is conceivable that the most recent volcanism along the central ridge postdates

the faults on the MLU, since the fault scarps that separate the graben from the central ridge are buried beneath lavas that can be traced to the central ridge near 45°32.25'N.

The youngest resolvable volcanic structures within the Vance segment's axial valley are the lavas that overlie the fault scarp along the western side of the MLU, located below the base of the west valley wall. These lavas are inferred to have erupted on the plateau to the west, based on the local topographic slope and the presence of subtle backscatter lineations that trend transverse to the trend of the west valley wall.

These relative age relationships suggest the following sequence of events (depicted in Figure 30), listed sequentially according to the maximum possible age of each event:

1) volcanic construction of the eastern and western marginal ridges;
2) faulting along the east and west valley walls (elevating the crests of the EMR and WMR above the axial valley);
3) volcanism within the axial valley (covering the area now elevated on the fault block between the inner and outer faults on the EMR);
4) resumed faulting along the eastern valley wall (elevating the fault block above the axial valley);
5) faulting near the terminus of the axial valley (N20°E-trending faults)
6) eruption of lavas from the central ridge;
7) faulting along the east and west sides of the west valley graben (disrupting lavas associated with the central ridge);
8) continued volcanism along the central ridge;
9) eruption of lavas on the plateau west of the axial valley, flooding the northern part of the valley with the MLU lavas;
10) faulting along the top of the MLU; and
11) eruption of minor plateau lavas that overlie the fault along the west side of the MLU, and possibly minor eruption of lavas along the central ridge.

Timing of Events on the Southern Flank of Axial Volcano

Similar crosscutting relationships between faults and lavas, as well as the superposition of high-backscatter lavas upon low-backscatter lavas, allows the

Figure 30. Composite line drawing showing the relative ages of major structures in and around the Vance segment's axial valley, interpreted from the sidescan imagery in Figures 18 through 22. Numbers indicate the sequence of formation of various structures within the Vance segment, as inferred from crosscutting and superposition relationships:

1. Volcanic construction of the eastern and western marginal ridges.
2. Faulting along the east and west valley walls.
3. Volcanism within the axial valley.
4. Renewed faulting along the eastern valley wall.
5. Faulting near the terminus of the axial valley (N20°E faults).
6. Eruption of lavas from the central ridge.
7. Faulting within the axial valley to form the west valley graben.
8. Continued volcanism along the central ridge.
9. Eruption of lavas on the plateau to the west of the axial valley, and flooding of the northern part of the axial valley by these lavas to form the MLU.
10. Faulting along the top of the MLU.
11. Eruption of lavas on the plateau that locally bury faults along the west side of the MLU.

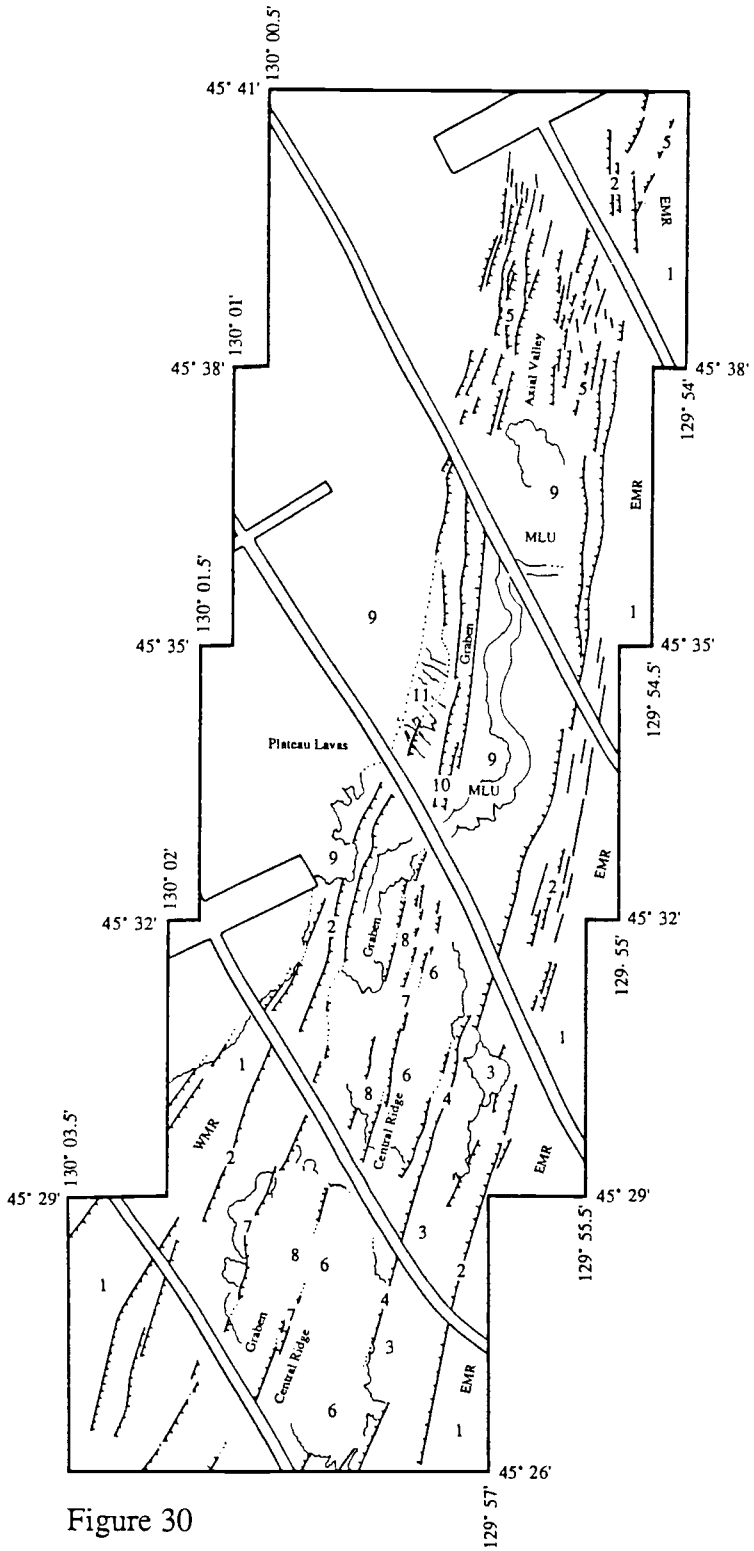
45° 41'
130° 00.5'
45° 38'
130° 01'
45° 35'
130° 01.5'
45° 32'
130° 02'
45° 29'
130° 03.5'
45° 26'
129° 57'
129° 54'
129° 54.5'
129° 55'
129° 55.5'
Axial Valley
MLU
EMR
WMR
Graben
Central Ridge
Plateau Lavas

Figure 30

relative ages of some of the structures within South Helium Basin to be estimated. The oldest surface associated with the basin is probably the seafloor atop the crest of the ridge on the basin's east side. The summit of the ridge displays low backscatter, and can be traced northwards to the eastern flank of Axial volcano. This ridge formed tectonically -- both its east and west sides are cut by major faults that must postdate the formation of the surface of the ridge crest. The lack of constructional volcanic features along the flanks of the ridge suggests that the vertical relief between the crest of the ridge and the floor of the basin resulted from displacement along the faults that separate them; the ridge did not grow upward due to constructional volcanism. The continuity of the ridge crest with the surface of the east flank of Axial volcano may indicate that activity along the fault primarily caused subsidence within the basin, with little uplift of the ridge itself. The ridge may have once been part of a broader structure that was faulted into its present shape. Unfortunately, the intersection of the ridge with the Axial volcano edifice is outside of the survey area, and the relationship between the ridge and the volcano cannot be unequivocally determined.

The faulted, low-backscatter region west of the east ridge in the southern part of the basin is intermediate in age between the ridge's west fault and the intermediate-backscatter lavas in the northern part of the basin. The intermediate-backscatter lavas abut the base of the west flank of the ridge near 45°44.25'N/129°55.7'W (Figure 29a) and extend southwards, covering the faulted low-backscatter area. Although a few faults mark the surface of the intermediate-backscatter lavas, fault density is much higher on the low-backscatter surface in the southern part of the basin, indicating that most of the faulting occurred prior to the emplacement of the intermediate-backscatter lavas.

The youngest lavas within the basin are the high-backscatter lavas near the basin's west side. In the northern part of the basin, these lavas are perched on a plateau 150 m above the intermediate-backscatter lavas, and bulbous lobes protrude from the constructional scarp between the two terrains, overlying the intermediate-backscatter surface. In the southern part of the basin, the high-backscatter lavas dam against the west-facing fault on the west side of the middle ridge, indicating that the fault is older than the lavas. The lavas here appear to have flowed downslope from the east SARZ ridge. The high-backscatter lavas on the plateau along the west side of the basin are crosscut by faults that can be traced southwards down the crest of the east SARZ ridge; these faults are the youngest discernable features within South Helium Basin.

The sequence of events within South Helium Basin constrained by these relative age estimates is depicted in Figure 31, and involves: 1) faulting along the west side of the basin's east ridge, dropping the floor of the basin down relative to the ridge's crest; 2) faulting and small-scale volcanism within the floor of the basin, creating the faulted topography now evident in the southern part of the basin: 3) invasion of lavas from the north, which flowed along the base of the west side of the east ridge and onlapped the older, faulted surface to the south; 4) emplacement of lavas along the western side of the basin that may be related to volcanism along the east SARZ ridge; and 5) displacement of the young lavas by the faults that extend south along the east SARZ ridge.

Unfortunately, the relative age dating technique does not constrain the maximum age for the faulting within the basin (with the exception of the faults atop the east ridge of the SARZ, which must be the youngest structures in the vicinity of the basin). Faulting within the basin must predate the emplacement of the lavas that overlie the faulted terrain, but whether the faulting occurred within the recent history of the volcano, or whether the faulted terrain is a relict fabric from a much earlier period, may not be determined.

Few constraints may be imposed on the timing of events within the south Axial rift zone. This is due in part to the absence of faulting within the SARZ, and also due to the lack of areally extensive, flat-lying lava flows that may be used to correlate widely-spaced, disparate structures. The rugged topography of the SARZ is composed of constructional volcanic structures that display similar backscatter characteristics, which prohibits even gross age estimates from being assigned to different surfaces based on differences in backscatter intensity. Conversely, the constant backscatter intensity over the rift zone suggests that the lavas on the surface of the SARZ were emplaced within the same general time period.

Constraints on the Timing of Events Based on Bathymetric Data

An age envelope for the sequence of events within the Vance segment can be constructed by determining the maximum age of formation of the EMR. The approximate ages of the ridges that flank the northern end of the Vance segment may be estimated using simple spreading rate calculations. Similar calculations were performed by Lichtman and Eissen (1983) to determine the age of the crust within the Cleft segment of the Juan de Fuca ridge, and by Hammond and Delaney (1985) to estimate the timing of the dislocation of the central Juan de Fuca spreading center

Figure 31. Composite line drawing showing the relative ages of major structures in South Helium Basin, interpreted from the sidescan images presented in Figures 28 and 29. Numbers indicate the sequence of formation of various structures as inferred from crosscutting and superposition relationships:

1. Faulting along the west side of the basin, downdropping the floor of the basin relative to the crest of the ridge on the east side of the basin.
2. Faulting and volcanism on the basin's floor.
3. Emplacement of lavas in the northern part of the basin that overlie the faulted, intermediate-backscatter terrain in the southern part of the basin.
4. Eruption of the lavas on the west side of South Helium Basin.
5. Faulting of the lavas on the west side of the basin.

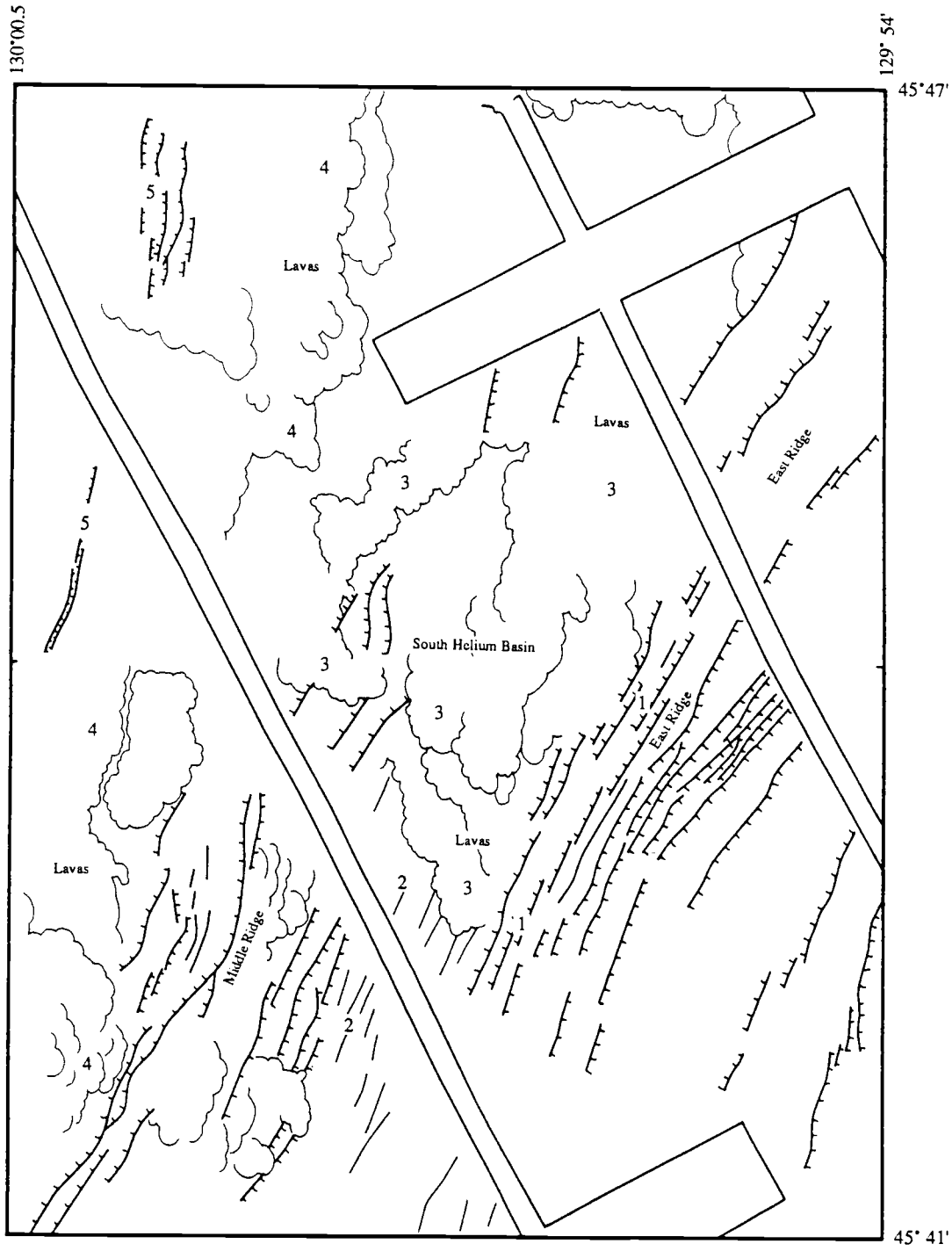
130°00.5
129° 54'
45°47'
45° 41'
Lavas
Lavas
Lavas
Lavas
South Helium Basin
East Ridge
East Ridge
Middle Ridge
1
2
3
4
5

Figure 31

near Axial volcano. These calculations are based on two assumptions, 1) that the ridges about the axial valley constitute half-ridges that were formed coevally as a single volcanic ridge over the spreading axis, and were subsequently rifted apart and rafted away from each other due to seafloor spreading concentrated in the ever-widening valley between them (essentially the non-steady state model for rift valley and marginal ridge construction of Kappel and Ryan, 1986); and 2) that the seafloor spreading half-rate of 29mm/yr (Karsten et al., 1986) has remained constant since the formation of the outermost ridges. The topographic symmetry across the spreading axis is consistent with the first premise. Near 45°25'N, the inward-facing flanks of the EMR and WMR are each 2.7 km from the geometric center of the axial valley, and the inner scarps of the west outer ridge (WOR) and east outer ridge (EOR) are each about 7.1 km from the center of the valley (Figure 2). The EMR and WMR are thus considered to be correlative, as are the WOR and EOR. Assuming the validity of the foregoing assumptions, the EMR and WMR rifted apart at 94 ka, and the WOR and EOR separated at about 245 ka. These ages are maximum values for the faulting episodes which split the ridges, since the summits of the ridges may have collapsed broadly rather than simply split apart. Therefore the N20°E-trending faults that crosscut the EMR near the northern tip of the Vance segment are younger than 94 ka, as are the rest of the volcanic and tectonic structures which are inferred to postdate the faulting along the eastern side of the axial valley within the Vance segment.

The morphology of the ridges that flank the Vance segment to the east may also provide insight into the tectonic evolution of the northern part of the Vance segment. The curvature observed along the northern tips of the EMR and EOR implies the presence of an overlapping spreading center configuration at the time each of the ridges formed. Bent ridge tips are a common characteristic of offset spreading centers (OSC's), and have been documented near OSC's on the East Pacific Rise (e.g., Macdonald and Fox, 1983; Lonsdale, 1983; Sempere and Macdonald, 1986; Antrim et al., 1988), and around propagating rifts on the Galapagos ridge (Hey et al., 1986) and East Pacific Rise (Naar and Hey, 1986; Macdonald et al., 1988). On the Juan de Fuca ridge, bent rift tips occur on the ridges surrounding the Cobb Offset (Hammond et al., 1981; Johnson et al., 1983) and the Endeavour Offset (Karsten et al., 1986). The presence of bent ridge tips about the Cobb Offset over a long period of time is reflected in the magnetic anomaly patterns along the the wake of the Cobb propagator (Johnson et al., 1983).

The bent tips of offset spreading centers are considered to form in response to the stress field generated by the offset geometry. Mid-ocean ridge spreading center systems have been studied using mathematical models (Pollard and Aydin, 1983), wax models, and photoelastic materials (Macdonald et al., 1984) in order to map the stress field surrounding the spreading axis. Most approaches model the spreading center as a simple crack under tensile stress within an elastic medium. For a single, isolated crack subjected to simple tension, tensile stress trajectories are oriented perpendicular to the long axis of the crack, and intermediate stress trajectories are parallel to the crack (Macdonald et al., 1984). These results predict that the strikes of normal faults generated near a spreading axis under such a stress regime will be oriented parallel to the intermediate stress trajectory, and hence parallel to the strike of the spreading ridge. For offset cracks, however, the stress trajectories near the area of offset rotate such that the intermediate stress trajectories around each ridge tip curve inward towards the opposing ridge tip (Pollard and Aydin, 1984; Macdonald et al., 1984). Therefore, faults generated near the tips of offset spreading centers are predicted to be oriented parallel to the intermediate stress trajectories and curve towards the interior of the offset. The westward-curving tips of the EMR and EOR indicate that the spreading axis north of the Vance segment was offset to the west of the Vance spreading axis during the formation of these ridges.

There is no evidence of a transform fault at the north end of the Vance segment, which suggests that the area of offset between the Vance segment and the spreading center to the north has not been stable through time. The geometry of the two ridges east of the Vance segment implies that the northern tip of the Vance segment retreated southwards between 245 ka and 94 ka. The northern tip of the EOR abuts the east flank of the Axial volcano near 45°46'N, and the EMR terminates near 45°42'N. Assuming that the tips of the ridges correspond to the northern terminus of the Vance spreading segment at the time each of the ridges formed, then the northern tip of the Vance segment retreated southwards by 7.4 km during the period between the formation of the ridges, which corresponds to an average rate of retreat of about 4.9 cm/year.

Discrimination of the Locus of Spreading Between 45°24'N and 45°47'N

The Juan de Fuca spreading axis is located within the axial valley of the Vance segment between 45°24'N and 45°39'N. The postulated sequence of tectonic

and volcanic events within the axial valley indicates that the most recent extension has been concentrated in the western half of the valley. South of 45°32'N, recent extensional faulting has constructed the west valley graben. North of 45°32'N, the fault scarps that define the graben atop the MLU are aligned with the trend of the west valley graben to the south, indicating that the recent locus of extension is continuous within the west side of the axial valley as far north as 45°37.5'N. The northern tip of the axial valley is offset 500 m to the east of the graben at 45°37.5'N. Faults associated with the east and west valley walls cannot be traced farther north than 45°40'N; this is the northern terminus of the Vance spreading segment.

Beyond 45°39'N, an unequivocal, discrete spreading locus is not visible. However, some limits on the location of the plate boundary zone may be imposed, based on the sidescan data, between the latitudes of 45°39'N and 45°48'N. The seafloor near the lower southeast flank of Axial volcano, east of South Helium Basin and northeast of the terminus of the Vance segment (around 45°42'N/129°54'W), displays low backscatter, and is interpreted to be sedimented and relatively old. Recent lavas, defined by high backscatter intensities, are not visible here. Although a few N20°E-trending faults occur in this area, fault density is low; therefore this region is probably not the site of significant active seafloor spreading.

Similarly, the region west of the south Axial rift zone may be ruled out as a location for the spreading axis. The low-backscatter seafloor west of the SARZ is judged to be old relative to the high-backscatter lavas of the rift zone, and is dissected by faults that are overlain by SARZ lavas. None of the faults, however, crosscut younger lavas, and no throughgoing structural trends are present that would suggest active extension is occurring there.

These two boundaries constrain an area roughly between 130°06'W and 129°54'W in which most of the divergence between the Pacific and Juan de Fuca plates is occurring. Two major structural features are located within this region: the SARZ, which is dominated by constructional volcanism and displays no evidence of recent faulting; and South Helium Basin, which is crosscut by several N25°E-trending faults and contains minor volcanic structures.

The SARZ has been interpreted as the site of the Juan de Fuca spreading axis based on the bilateral symmetry expressed in the rift's topographic profile between the west and middle ridges (Hammond and Delaney, 1985). This interpretation implies that the spreading axis is located within the valley that separates the two ridges. According to the non-steady state model for the construction of rift valleys on the Juan de Fuca ridge proposed by Kappel and Ryan (1986), the

formation of marginal ridges about the spreading axis is cyclic, and involves first the construction of a single ridge over the spreading locus during a period of high volcanic output (one example of such a ridge is the central ridge bisecting the Vance spreading axis), followed by a period of volcanic quiescence during which the summit of the volcanic ridge collapses. The remnants of the original ridge, which are essentially half-ridges at this point, are thus left standing on opposite sides of the rift valley, and are subsequently rafted apart by plate divergence along the spreading axis. This model predicts that the inward-facing sides of the half-ridges will display fault scarps, and the outer sides will retain the original constructional volcanic morphology of the ridge. The resulting half-ridges display a characteristic asymmetric cross-sectional profile in which the inner side is steep, the summit is relatively flat, and the outer side gradually slopes away from the ridge in a convex-up manner (the "baroque scroll" morphology described in Kappel and Ryan, 1986). The interior of the rift axis should display swarms of small-offset faults and fissures that result from extension within the rift valley. This model further implies that the opposing, rifted half-ridges formed coevally and constitute isochrons.

The middle and west ridges of the SARZ do not meet these criteria for rifted half-ridges about a spreading axis. The east and west flanks of both ridges display constructional volcanic features along their entire lengths, and there are no fault scarps cutting the high-backscatter lavas on the flanks that slope into the medial valley between the two ridges. The floor of the medial valley is not flat in cross-section as would be expected for the floor of a rift valley, and is covered by intact constructional volcanics that are not faulted. The flanks of each ridge are symmetric in cross-sectional profile, and the crests of the ridges rise to a sharp peak. The ridges therefore display neither the asymmetric, scroll-shaped profile nor the flat summit of a rifted half-ridge.

The SARZ is obviously the site of voluminous volcanic activity, and the possibility remains that the characteristic structures indicative of a rifted spreading center may simply be masked beneath a veneer of volcanic products. However, the pattern of volcanism over the SARZ suggests that the valley between the west and middle ridges is not the discrete axis of spreading. If the west and middle ridges constitute half-ridges bisected by the spreading axis, then subsequent volcanism would be expected to be concentrated within the rift valley between them, and not along their summits. Volcanic activity along ridge segments elsewhere on the Juan de Fuca ridge has consistently been documented within the rift valleys, with little or no recent activity occurring along the crests or flanks of the marginal ridges. The

axial valley floor of the Cleft segment is covered by voluminous flows that erupted from a medial fissure which bisects the marginal ridges, located on or near the geometrical spreading axis (Kappel et al., 1983; Lichtman and Eissen, 1983; USGS Juan de Fuca Study Group, 1986). Volcanic activity along the Vance segment has constructed a topographic ridge that extends up the center of the axial valley (Embley et al., 1983; Kappel and Ryan, 1986). The sidescan imagery in this survey indicates that most of the recent volcanism within the axial valley of the northern Vance segment has been concentrated along the central ridge, and no recent flows associated with normal seafloor spreading are evident outside of the axial valley. Lobate flow structures observed on the outer flanks of the marginal ridges on the Cleft, Vance, and Endeavour segments have been interpreted to have formed from lavas that flowed from vents along the spreading axis during the initial constructional phase that built the ridges; the lobate structures did not erupt along the crests or flanks of the marginal ridges after they were rifted apart (Kappel and Ryan, 1986). As pointed out by Kappel and Ryan (1986), rift valley volcanism would tend to fill the valley from the bottom up. Therefore, during a constructional phase along the ridge segment, volcanic products would be expected to floor the axial valley, leaving the steep upper parts of the boundary faults on the valley walls exposed. The sidescan sonar imagery presented here shows that the crests of the west and middle ridges on the SARZ have been volcanically active, and that fault scarps are not present along the flanks of the ridges. The west and middle ridges do not appear to be rifted half-ridges that have been modified by high degrees of late-stage volcanism.

Furthermore, if the valley between the east and middle ridges was the axis of spreading, faulting should be evident near their distal end of the SARZ. The area over which faulting occurs within the axial valley has been shown to widen towards the distal ends of the Endeavour segment (Barone and Ryan, 1988), and fault density has been observed to increase near the tips of overlapping spreading centers on the East Pacific Rise (Antrim et al., 1988). As shown by the sidescan imagery in this survey (Plate 1 and Figure 22a), the number of fault scarps increases dramatically at the northern tip of the Vance segment. Furthermore, the decrease in total relief and size of the SARZ ridges towards the south indicates that the amount of volcanic material that has erupted along the rift zone decreases as the tip of the SARZ is approached. With decreasing volcanism, existing fault scarps would have a greater probability of remaining exposed. Due to the combined anticipated effects of waning volcanism, increasing fault density, and a widening zone over which faulting occurs, fault scarps would be expected to be observed near the southern tip

of the SARZ if it were a discrete spreading segment. With only one minor exception (a small N15°E-trending fault scarp near 45°33'N/130°07'W), no evidence of faulting was found along the entire lengths of the west and middle SARZ ridges.

The presence of widespread faulting within South Helium Basin indicates that extension has occurred in this region, east of the south Axial rift zone. The basin is a tectonic structure, as indicated by the 200 m fault scarp that bounds the basin's east side. The ridge on the east side of the basin is not simply an elongate constructional volcanic feature protruding southwards from the main edifice of Axial volcano, as indicated by the fault-bounded nature of the ridge and the lack of volcanic structures over its flanks. The crest of the ridge can be traced continuously along the 2200 m isobath to the eastern flank of Axial volcano (Figure 17), suggesting that the ridge and the volcano may be continuous, related structures. The floor of the basin, where not buried beneath younger lavas, is cut by numerous N25°E-trending faults. Based on these interpretations, South Helium Basin may represent an area of collapse within the southeast flank of Axial volcano, possibly related to extension over the plate boundary zone. However, the maximum age of the faulting that constructed the basin cannot be constrained by the relative age dating technique, and the basin may be an old, relict structure that is not related to recent extension.

A well-defined, unequivocal axis of spreading over the south flank of axial volcano (north of 45°39'N) is not resolvable in the sidescan imagery. By process of elimination, the plate boundary zone can be confined to a region between 130°06'W and 129°54'W. The west and middle SARZ ridges do not exhibit structural characteristics indicative of rifted half-ridges, and therefore the valley separating them cannot be constrained by these data as the spreading locus. The complicated morphology of the southern flank of Axial volcano suggests that volcanic processes associated with the volcano have complexly interacted with the volcanic and tectonic processes of the Juan de Fuca ridge to construct this region. Although divergence between the Pacific and Juan de Fuca plates must be occurring over these latitudes, the physical manifestation of the plate boundary has been sufficiently modified or masked by the hotspot volcanic processes related to Axial volcano such that a definitive locus of spreading is not expressed in the surface morphology.

AREAS OF FUTURE STUDY

In order to more completely understand the nature of the divergent plate boundary near Axial volcano, several avenues of future study should be pursued. Numerical and physical modelling of the stress regime that is generated by a radial stress field (the Axial hotspot) to a uniaxial stress field (the Juan de Fuca spreading axis) could address many relevant questions regarding the interpretation of the morphology of the southern flank of Axial volcano and the northern part of the Vance segment:

1) What are the principal stress trajectories predicted for the region where the two stress fields interfere, and what patterns of tectonic activity would be expected?
2) Would the trajectories be expected to vary as the two stress fields approach one another, as is occurring between the Juan de Fuca ridge and the hotspot?
3) How does the mass of the volcanic edifice affect the stress regime?
4) Would the plate boundary zone beneath the volcano be expected to be broad, with extension accommodated diffusely within the crust, or would the plate boundary be narrow? In either case, how would the faults be be predicted to propagate up through the volcanic massif, and what patterns of faulting would result?

Numerical models (e.g., Pollard and Aydin, 1983) and physical models (such as the wax and photoelastic material modelling discussed in Macdonald et al., 1984) of the stress fields generated near offset, propagating cracks have provided valuable insight into the processes involved near propagating rifts and offset spreading centers (e.g. Macdonald et al., 1983; Macdonald et al., 1987: Macdonald et al., 1988). Similar studies of the stress regime around Axial volcano could reveal important information to facilitate the interpretation of the geophysical processes that are responsible for shaping the seafloor in this region.

Additional constraints could be imposed on the evolution of Axial volcano's south rift zone by determining the ages of the lavas that construct each of the SARZ ridges. A west-to-east age progression (with the east ridge being youngest) would imply that either 1) the plate boundary is east of the ridge, and the

SARZ ridges were constructed sequentially as the crust beneath the south Axial rift zone was rafted westward past the hotspot, or 2) the decreasing distance between the Cobb-Eickelberg hotspot and the Juan de Fuca spreading axis is controlling the position of the ridges. In both cases, episodic phases of constructional rift zone volcanism are implied. The absence of a definitive age progression from ridge to ridge would suggest that the ridges were not constructed in succession, and perhaps volcanism has occurred concomitantly along the entire breadth of the rift zone. Age dating could be accomplished using magnetic secular variation measurements similar to those conducted on Kilauea (e.g., Holcomb, 1980; Holcomb et al., 1986), which have been proposed as a means of dating rift zone basalts elsewhere (Holcomb and Clague, 1986). Alternatively, relative ages of lavas from each of the ridges could be estimated based on palagonite thicknesses in a manner similar to that employed by Lichtman and Eissen (1983) for basalts from the Cleft segment of the Juan de Fuca ridge.

Further studies should also be performed to establish the validity of the interpretations drawn from the sidescan sonar imagery. Relative ages assigned to the various structures and processes within the study area are contingent upon crosscutting relationships between volcanic structures and faults; corroboration of these crosscutting relationships by independent data sets would lend credence to the inferred ages, or alternatively, if a more detailed data set proved some of the relationships to be unsupportable, then the relative age scheme could be further refined. The relationship between low backscatter intensities and sediment thickness should be investigated to determine whether the assumptions made in this study are accurate; a consistent correlation between backscatter intensity and sediment thickness would enable rough absolute age estimates to be inferred using sedimentation rates. Seafloor photography is an efficient means of groundtruthing large sidescan sonar survey areas (Holcomb, 1985) which would enable the structural and morphological interpretations of this study to be checked.

SUMMARY

The algorithm developed in this study for estimating the path of the sidescan vehicle provides an effective means for navigating sidescan images, and enables sidescan data from adjacent and overlapping sonar swaths to be combined in order to construct computer-generated mosaics of the backscatter characteristics of the seafloor. Since the navigation process determines the position of the sidescan vehicle at the time of each outgoing acoustic pulse, variations in the vehicle's speed over ground are automatically accounted for, resulting in orthorectified sidescan images. Computer-generated mosaics constructed from navigated sidescan data afford many advantages over manually constructed mosaics. Once developed, the computer process for generating sidescan mosaics enables high-quality, final sidescan images to be produced from raw data with a minimum turnaround time. Sidescan mosaics may be generated at any scale, using any projection, allowing close-ups of areas of interest to be produced just as easily as large-scale, regional images. The navigated sidescan mosaics can be plotted directly onto a lat/long grid, facilitating the comparison of the sidescan imagery with ancillary data sets.

The utility of sidescan mosaics as tools for interpreting the regional geology has also been demonstrated. The continuity of large features, such as the ridges of the south Axial rift zone and the faults that define the axial valley of the Vance segment, are maintained from swath to swath, facilitating the identification and correlation of major throughgoing structures. Large-scale plots of sidescan mosaics are valuable for their ability to show regional relationships that are not as evident in individual swaths, for example the westward-curving tip of the Vance segment, and the continuity between the SARZ ridges and the hilly terrain at the distal southern end of the SARZ. On a finer scale, the sidescan mosaics enable discrete structures and backscatter patterns to be traced from swath to swath, facilitating correlations that are critical in order to assign relative ages to disparate structures.

The backscatter characteristics revealed in the sidescan imagery provide a means for estimating first-order age relationships between faults and lava flows. Basic crosscutting and superposition principles were applied to assign relative ages to the volcanic and tectonic structures within South Helium Basin and the Vance segment's axial valley, and the relative age relationships were used to formulate scenarios for the evolution of each region. Based on the sidescan imagery, several

conclusions may be drawn regarding the several recognizable provinces within the survey area:

1) The Vance Segment. The axis of spreading between the Pacific and Juan de Fuca plates is located within the axial valley of the Vance segment. The most recent resolvable extension within the axial valley has been concentrated between the valley's west wall and central ridge; the central ridge has been the site of the most recent resolvable rift-valley volcanism. The Vance segment terminates at 45°39'N, and a discrete spreading locus is not resolvable north of this point. The westward curvature of the tectonic fabric along the northern part of the axial valley implies that, north of 45°39'N, the seafloor spreading axis is offset from the Vance segment in a left-stepping fashion. The northern tip of the Vance segment is not linked with a transform fault, and is inferred to have retreated southwards at an average rate of 4.9 cm/yr between 245 ka and 94 ka. Within the past 94 ka, faults associated with the axial valley walls have propagated northwards through preexisting tectonic fabric associated with the EMR.
2) The South Rift Zone of Axial Volcano. The SARZ is a constructional volcanic feature composed of three primary volcanic ridges. Volcanic cones along the crests of the two western ridges increase in abundance towards the south, and dominate the topography near the distal southern end of the rift zone. Lavas on the west side of the SARZ have erupted along older, preexisting faults to construct linear ridges; the volcanic ridges and coalesced cones that comprise the surface of the SARZ may have also erupted from preexisting planes of weakness in the underlying crust. Tectonic activity has not disrupted the volcanic carapace of the rift zone and a discrete location for the Juan de Fuca spreading axis is not evident over the SARZ.
3) South Helium Basin. Volcanic and tectonic processes have combined to construct South Helium Basin. Young lavas have invaded the basin from the west and north, and overlie the older, faulted floor of the basin. The negative relief of the basin (relative to the Axial volcanic edifice) may have resulted from a

collapse of the southeast flank of Axial volcano, possibly related to recent extension associated with the Juan de Fuca spreading center; however, the maximum age of the faults within the basin cannot be constrained based on the relative age dating technique, and the basin may be an old, relict feature.

BIBLIOGRAPHY

Antrim, L., J.-C. Sempere, K. C. Macdonald, and F. N. Spiess, Fine-scale study of a small overlapping spreading center system on the East Pacific Rise, *Marine Geophysical Researches, 9*, 115-130,1988.

Atwater, T., Implications of plate tectonics for the Cenozoic tectonic evolution of western North America, *Geological Society of America Bulletin, 81*, 3513-3536, 1970.

Barone, A. M., and W. B. F. Ryan, Along-axis variations within the plate boundary zone of the southern segment of the Endeavour Ridge, *Journal of Geophysical Research, 93*,7856-7868, 1988.

Blackington, J. G., D. M. Hussong, and J. G. Kosalos, First results from a combination side-scan and seafloor mapping system (SeaMARC II), in *Proceedings of the Fifteenth Offshore Technology Conference*, pp. 276-292, Houston, 1983.

Boegeman, D. E., G. J. Miller, and W. R. Normark, Precise positioning for near-bottom equipment using a relay transponder, *Marine Geophysical Researches, 1*, 381-396, 1972.

Carlson, R. L., Late Cenozoic rotations of the Juan de Fuca Ridge and the Gorda Rise: A case study, *Tectonophysics, 77*, 171-188, 1981.

Cassarella, M. J., and M. Parsons, A survey of investigations on the configuration and motion of cable systems under hydrodynamic loading, *Marine Technology Society Journal, 4*, 27-44, 1970.

Chayes, D., Evolution of SeaMARC I, in *IEEE Proceedings of the Third Working Symposium on Oceanographic Data Systems*, pp. 103-108, New York, IEEE Computer Society Press, 1983.

Chitwood, L. A., Origin and morphology of inflated lava, *EOS Trans. AGU, 68*, 1545, 1987.

Choo, Y.-I. and M. J. Cassarella, Hydrodynamic resistance of towed cables, *Journal of Hydronautics, 5*, 126-131, 1971.

Crane, K., F. Aikman, R. W. Embley, S. R. Hammond, A. Malahoff, and J. Lupton, The distribution of geothermal fields on the Juan de Fuca ridge, *Journal of Geophysical Research, 90*, 727-744, 1985.

Davis, E. E., and J. L. Karsten, On the cause of the asymmetric distribution of seamounts about the Juan de Fuca ridge: Ridge-crest migration over a

heterogeneous asthenosphere, *Earth and Planetary Science Letters, 79*, 385-396, 1986.

Delaney, J. R., H. P. Johnson, and J. L. Karsten, The Juan de Fuca ridge -- hot spot -- propagating rift system: New tectonic, geochemical, and magnetic data, *Journal of Geophysical Research, 86*, 11747-11750, 1981.

Desonie, D. L., and R. A. Duncan, Spreading ridge and hotspot contributions to seamounts near the Juan de Fuca ridge, *EOS Trans, AGU*, 67, 1231, 1986.

Dobrin, M. B., *Introduction to Geophysical Prospecting*, 630 pp., McGraw-Hill, New York, 1976.

Elvers. D., S. P. Srvivastava, K. Potter, J. Morley, and D. Sdidel, Asymmetric spreading across the Juan de Fuca and Gorda Rises as obtained from a detailed magnetic survey, *Earth and Planetary Science Letters, 20*, 211-219, 1973.

Embley, R. W., S. R. Hammond, A. Malahoff, W. F. B. Ryan, K. Crane, and E. Kappel, Rifts of the southern Juan de Fuca, *EOS Trans. AGU*, 64, 853, 1983.

Engebretson, D. C., A. Cox, and R. G. Gordon, Relative motions between oceanic and continental plates in the Pacific Basin, *Geological Society of America Special Paper 206*, 1-59, 1985.

Farre, J., The importance of mass wasting processes on the continental slope, pp. 225, Palisades, New York, Ph.D dissertation, Columbia University, 1985.

Flemming, B. W., Side-scan sonar: A practical guide, *International Hydrographic Review, 53*, 56-92, 1976.

Fornari, D. J., W. B. F. Ryan, and P. J. Fox, The evolution of craters and calderas on young seamounts: Insights from SeaMARC I and SeaBeam sonar surveys of a small seamount group near the axis of the Eastn Pacific Rise at ≈ 10°N, *Journal of Geophysical Research, 89*, 11069-11083, 1984.

Fornari, D. J., W. B. F. Ryan, and P. J. Fox, Sea-floor lava fields on the East Pacific rise, *Geology, 13*, 413-416, 1985.

Fox, C. G., and D. E. Hayes, Quantitative methods for analyzing the roughness of the seafloor, *Reviews of Geophysics and Space Physics, 23*, 1-48, 1985.

Guest, J. E., C. R. J. Kilburn, H. Pinkerton, and A. M. Duncan, The evolution of lava flow-fields: observations of the 1981 and 1983 eruptions of Mount Etna, Sicily, *Bulletin of Volcanology, 49*, 527-540, 1987.

Hammond, S. R., A. Malahoff, and R. N. Hey, Detailed bathymetric evidence for recent rifting at the Cobb Propagator, Juan de Fuca Ridge, *EOS Trans. AGU, 62*, 1028, 1981.

Hammond, S. R., and J. R. Delaney, Evolution of Axial Volcano, Juan de Fuca ridge, *EOS Trans. AGU, 66*, 925, 1985.

Hammond, S. R., R. W. Embley, C. G. Fox, J. R. Delaney, and T. B. Appelgate, Tectonic relationships between Axial volcano and the central segment of the Juan de Fuca ridge, in *Hawaii Symposium on How Volcanoes Work*, Hawaiian Volcano Observatory, pp. 99, 1987.

Heirtzler, J. R., G. O. Dickson, E. M. Heron, W. C. Pitman III, and X. Le Pichon, Marine magnetic anomalies, geomagnetic field reversals, and motions of the ocean floor and continents, *Journal of Geophysical Research, 73*, 2119-2136, 1968.

Hey, R. N., A new class of "pseudofaults" and their bearing on plate tectonics: A propagating rift model, *Earth and Planetary Science Letters, 37*, 321-325, 1977.

Hey, R. N., Duennebier, F. K., and W. J. Morgan, Propagating rifts on midocean ridges, *Journal of Geophysical Research, 85*, 3647-3658, 1980.

Hey, R. N., and D. S. Wilson, Propagating rift explanation for the tectonic evolution of the northeast Pacific -- the pseudomovie, *Earth and Planetary Science Letters, 58*, 167-188, 1982.

Hey, R. N., M. C. Kleinrock, S. P. Miller, T. M. Atwater, and R. C. Searle, Deep-Tow investigation of an active oceanic propagating rift system, Galapagos 95.5°W, *Journal of Geophysical Research, 91*,3369-3393, 1986.

Holcomb, R. T., Kilauea Volcano, Hawaii: Chronology and morphology of the surficial lava flows, *USGS Open File Report, 81-354*, 1980.

Holcomb, R. T., and D. A. Clague, Volcanic eruption patterns along submarine rifts, in *Oceans '86*, IEEE/MTS, 787-790, 1986

Holcomb, R. T., D. Champion, and M. McWilliams, Dating recent Hawaiian lava flows using paleomagnetic secular variation, *Geological Society of America Bulletin, 97*, 829-839, 1986.

Ivers, W. D., and J. D. Mudie, Towing a long cable at slow speeds: A three-dimensional dynamic model, *Marine Technology Society Journal, 7*, 23-31, 1973.

Johnson, H. P., J. L. Karsten, J. R. Delaney, E. E. Davis, R. G. Currie, and R. L. Chase, A detailed study of the Cobb Offset of the Juan de Fuca Ridge: Evolution of a propagating rift, *Journal of Geophysical Research, 88*, 2297-2315, 1983.

Kappel, E. S., R. W. Embley, W. B. F. Ryan, R. Perry, and A. Malahoff, The great cover-up on the southern Juan de Fuca ridge, *EOS Trans. AGU*, 64, 853, 1983.

Kappel, E. S., and W. B. F. Ryan, volcanic episodicity and a non-steady state rift valley along the northeast Pacific spreading centers: Evidence from SeaMARC I, *Journal of Geophysical Research, 91*, 13925-13940, 1986.

Kappel, E. S., and W. R. Normark, Morphometric variability within the axial zone of the southern Juan de Fuca ridge: Interpretation from SeaMARC II, SeaMARC I, and deep-sea photography, *Journal of Geophysical Research, 92*, 11291-11302, 1987.

Karsten, J. L., S. R. Hammond, E. E. Davis, and R. G. Currie, Detailed geomorphology and neotectonics of the Endeavour Segment, Juan de Fuca Ridge: New results from Seabeam swath mapping, *Geological Society of America Bulletin, 97*, 213-221, 1986.

Karsten, J. L., and J. R. Delaney, Hot spot/migrating ridge crest interaction -- Juan de Fuca style, *EOS Trans. AGU, 67*,1254, 1986.

Kosalos, J., and D. Chayes, A portable system for ocean bottom imaging and charting, in *IEEE Proceedings of the Third Working Symposium on Oceanographic Data Systems*, pp. 649-656, New York, IEEE Computer Society Press, 1983.

Leenhardt, O., Side-scanning sonar - a theoretical study, *International Hydrographic Review, 51*, 61-80, 1974.

Le Guerch, E., The deep towing of underwater fish behaviour patterns during half-turn manoeuvres, *Ocean Engineering, 14*, 145-162, 1987.

Lichtman, G. S., and J-P Eissen, Time and space constraints on the evolution of medium-rate spreading centers, *Geology, 11*, 592-595, 1983.

Lonsdale, P., Overlapping rift zones at the 5.5°S offset of the East Pacific Rise, *Journal of Geophysical Research, 88*, 9393-9406, 1983.

Macdonald, K. C., and P. J. Fox, Overlapping spreading centers: New accretion geometry on the East Pacific Rise, *Nature, 302*, 55-58, 1983.

Macdonald, K. C, J.-C. Sempere, and P. J. Fox, East Pacific Rise from Siqueiros to Orozco Fracture Zones: Along-stride continuity of axial neovolcanic zone and structure and evolution of overlapping spreading centers, *Journal of Geophysical Research, 89*, 6049-6069, 1984.

Macdonald, K. C., J.-C. Sempere, P. J. Fox, and R. Tyce, Tectonic evolution of ridge-axis discontinuities by the meeting, linking, or self-decapitation of neighboring ridge segments, *Geology, 15*, 993-997, 1987.

Macdonald, K. C., R. M. Haymon, S. P. Miller, J-C Sempere, and P. J. Fox, Deep-Tow and SeaBeam studies of dueling propagating ridges on the East Pacific Rise Near 20°40'S, *Journal of Geophysical Research, 93*, 2875-2898, 1988.

McKinney, C., and C. D. Anderson, Measurement of backscattering of sound from the ocean bottom, *Journal of the Acoustical Society of America, 36*, 158-163, 1964.

Menard, H. W., Fragmentation of the Farallon plate by pivoting subduction, *Journal of Geology, 86*, 99-110, 1978.

Morton, J. L., N. H. Sleep, W. R. Normark, and D. H. Tompkins, Structure of the southern Juan de Fuca ridge from seismic reflection records, *Journal of Geophysical Research, 92*, 11315-11326, 1987.

Mudie, J. D., W. R. Normark, and E. J. Cray, Jr., Direct mapping of the sea floor using side-scanning sonar and transponder navigation, *Geological Society of America Bulletin, 81*, 1547-1554, 1970.

Naar, D. F., and R. N. Hey, Fast rift propagation along the East Pacific Rise near Easter Island, *Journal of Geophysical Research, 91*, 3425-3438, 1986.

Nishimura, C., D. S. Wilson, and R. N. Hey, Pole of rotation analysis of present-day Juan de Fuca plate motion, *Journal of Geophysical Research, 89*, 10283-10290, 1984.

Paluzzi, P. R., R. D. Toaz, D. G. Roberts, R. C. Searle, and M. L. Somers, Computer rectification and mosaicking of side-looking sonar image, in *Proceedings of the Thirteenth Offshore Technology Conference*, pp. 103-115, Houston, 1981.

Pollard, D. D., and A. Aydin, Propagation and linkage of oceanic ridge segments, *Journal of Geophysical Research, 89*, 10017-10028, 1984.

Prior, D. B., J. M. Coleman, and L. E. Garrison, Digitally acquired undistorted side-scan sonar images of submarine landslides, Mississippi River delta, *Geology, 7*,423-425, 1979.

Raff, A. D., and R. G. Mason, Magnetic survey off the west coast of North America, 40°N to 52°N latitude, *Geological Society of America Bulletin, 82*, 1267-1270,1961.

Ransford, G. A., and J. W. Ioup, Locating and determining the orientation of underwater research equipment: Acoustic range and range rate data, *IEEE Journal of Oceanic Engineering, OE-12*, 524-533, 1987.

Riddihough, R. P., Recent movements of the Juan de Fuca plate system, *Journal of Geophysical Research, 89*, 6980-6994, 1984.

Riddihough, R. P., M. E. Beck, R. L. Chase, E. E. Davis, R. D. Hyndman, S. H. Johnson, and G. C. Rogers, Geodynamics of the Juan de Fuca plate, in *Geodynamics of the Eastern Pacific and Scotia Ridges*, ed. R. Cabre, American Geophysical Union, 5-21, 1983.

Schram, J. W., and S. P. Reyle, A three-dimensional analysis of a towed system, *Journal of Hydronautics, 2*, 213-220, 1968.

Sempere, J-C, and K. Macdonald, Deep-Tow studies of the overlapping spreading centers at 9°03'N on the East Pacific Rise, *Tectonics, 5*, 881-900, 1986.

Silver, E. A., Small plate tectonics in the northeastern Pacific, *Geological Society of America Bulletin, 82*, 3491-3496, 1971.

Somers, M. L., and A. R. Stubbs, Sidescan Sonar, *IEEE Proceedings, 131*, 243-256, 1984.

Takahashi, T. J., and J. D. Griggs, Hawaiian volcanic features: A photoglossary, in *Volcanism in Hawaii*, edited by R.W. Decker, T. L. Wright, and P. H. Stauffer, USGS Professional Paper 1350, 845-902, 1987.

Teleki, P. G., D. G. Roberts, P. S. Chavez, M. L. Somers, and D. C. Twichell, Sonar survey of the U.S. Atlantic continental slope: Acoustic characteristics and image processing techniques, in *Proceedings of the Thirteenth Offshore Technology Conference*, pp. 91-102, Houston, 1981.

Theilig, E., and R. Greeley, Lava flows on Mars: Analysis of small surface features and comparisons with terrestrial analogs, in *Proceedings of the Seventeenth Lunar and Planetary Science Conference, Part 1, Journal of Geophysical Research, 91*, E193-E206, 1986.

USGS Juan de Fuca Study Group, Submarine fissure eruptions and hydrothermal vents on the southern Juan de Fuca Ridge: Preliminary observations from the submersible *Alvin*, *Geology, 14*, 823-827, 1986.

Vine, F. J., Spreading of the ocean floor: New evidence, *Science, 154,* 1405-1415, 1966.

Vine, F. J., and D. H. Mathews, Magnetic anomalies over ocean ridges, *Nature, 199*, 947-949, 1963.

Vine, F. J., and J. T. Wilson, Magnetic anomalies over a young oceanic ridge off Vancouver Island, *Science, 150*, 485- 489, 1965.

Vogt, P. R. and B. E. Tucholke, Imaging the ocean floor History and state of the art, in *The Geology of North America, Volume M, The Western North Atlantic Region*, edited by P. R. Vogt and B. E. Tucholke, pp. 19-44, New York, Geological Society of America, 1986.

Wilson, D. S., A kinematic model for the Gorda Deformation Zone as a diffuse southern boundary of the Juan de Fuca Plate, *Journal of Geophysical Research, 91*, 10259-10269, 1986.

Wilson, D. S., R. N. Hey, and C. Nishimura, Propagation as a mechanism of reorientation of the Juan de Fuca Ridge, *Journal of Geophysical Research, 89*, 9215-9225, 1984.